

Spring 2012

# Synergistic Effect of Subnanosecond Pulsed Electric Fields and Temperature on the Viability of Biological Cells

James Thomas Camp  
*Old Dominion University*

Follow this and additional works at: [https://digitalcommons.odu.edu/ece\\_etds](https://digitalcommons.odu.edu/ece_etds)



Part of the [Biomedical Engineering and Bioengineering Commons](#), [Electrical and Computer Engineering Commons](#), and the [Oncology Commons](#)

---

## Recommended Citation

Camp, James T.. "Synergistic Effect of Subnanosecond Pulsed Electric Fields and Temperature on the Viability of Biological Cells" (2012). Doctor of Philosophy (PhD), dissertation, Electrical/Computer Engineering, Old Dominion University, DOI: 10.25777/qfcp-0n91  
[https://digitalcommons.odu.edu/ece\\_etds/57](https://digitalcommons.odu.edu/ece_etds/57)

This Dissertation is brought to you for free and open access by the Electrical & Computer Engineering at ODU Digital Commons. It has been accepted for inclusion in Electrical & Computer Engineering Theses & Dissertations by an authorized administrator of ODU Digital Commons. For more information, please contact [digitalcommons@odu.edu](mailto:digitalcommons@odu.edu).

**SYNERGISTIC EFFECT OF SUBNANOSECOND PULSED ELECTRIC FIELDS  
AND TEMPERATURE ON THE VIABILITY OF BIOLOGICAL CELLS**

by

James Thomas Camp  
B.S. December 2005, Christopher Newport University

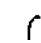
A Dissertation Submitted to the Faculty of  
Old Dominion University in Partial Fulfillment of the  
Requirements for the Degree of

DOCTOR OF PHILOSOPHY


ELECTRICAL ENGINEERING

OLD DOMINION UNIVERSITY

May 2012

Approved by: 

\_\_\_\_\_  
Karl H. Schoenbach (Director)

\_\_\_\_\_  
 Juergen Kolb (Member) /

\_\_\_\_\_  
Richard Heller (Member)

\_\_\_\_\_  
Shirshak Dhali (Member)

## ABSTRACT

### SYNERGISTIC EFFECT OF SUBNANOSECOND PULSED ELECTRIC FIELDS AND TEMPERATURE ON THE VIABILITY OF BIOLOGICAL CELLS

James Thomas Camp  
Old Dominion University, 2012  
Director: Dr. Karl H. Schoenbach

Pulsed electric fields have been used to induce a biological response in cells, and at sufficient energy, can cause cell death. By reducing the pulse duration from presently used nanosecond to subnanosecond ranges, the electric field can be delivered to biological tissue non-invasively by the use of an antenna instead of electrodes, such as needles. Studies have previously been completed in which the aim was to determine the energy density (electric field strength, number of pulses) required to induce cell death with 800 ps pulses. Based on this data, it was concluded that for pulse durations of 200 ps, with electric field strengths below 100 kV/cm, pulse numbers on the order of  $10^6$  would be needed to achieve similar effects. In this dissertation, it was shown that the energy density required for cell death can be reduced considerably if the temperature of the sample is increased to values above physiological temperature (37°C).

In order to perform the experiments, a solution of biological sample (growth medium and Hepa 1-6 cells) was exposed to 200 ps pulses in which the electric field strength ranged from 60 kV/cm to 100 kV/cm and the pulse number ranged between 100 and 3,300 pulses. The temperature of the sample was controlled externally by placing the exposure chamber in a controlled temperature environment, and was varied between room temperature and 47°C. In order to reduce the thermal effects due to ohmic heating from the pulses, the repetition rate of the pulses was kept below 10 Hz. The effect, cell death, was determined by trypan blue uptake of the cells 4 hours after experimental exposure.

The pulse generator used was an 8 stage Marx bank in which the output pulse was formed with a peaking and tailcut switch. The peaking switch was used to decrease the risetime of the output pulse to less than 200 ps, and the tailcut switch was used to cut off the decaying portion of the pulse. The eight spark gap switches of the Marx bank were pressurized with Nitrogen, while both the peaking and tailcut switch operated in air at atmospheric pressure. The output voltage of the pulse generator ranged from 10 kV to 20 kV and the pulse width could be varied between 140 ps and 230 ps. A conical exposure chamber was designed to expose the biological sample to the pulsed voltages, such that the electric field across the gap was homogeneous. The voltage was measured with a capacitive voltage divider, which was incorporated into the cable leading to the load.

The results indicate that an increase in temperature above 37°C caused the cells to be more susceptible to the pulsed electric fields. The lethality increased to over 25% (trypan blue uptake) when the cells were exposed to 2,000 pulses with an electric field strength of 78 kV/cm at 47°C. For temperatures at and below 37°C, there was no indication of cell death, when compared to the controls, for the same pulsing conditions.

In order to determine the reason for this increase in cell lethality due to the pulsed electric fields with an increase in temperature, the electrical properties of HELA 1-6 cells were measured by means of time domain reflective spectroscopy. The conductivity of the growth medium, plasma membrane, and cytoplasm increased with temperature. The permittivity of the medium and membrane increased, while the permittivity of the cytoplasm decreased with temperature. Using this data and comparing the results of the trypan blue studies, it seems to be likely that the subnanosecond pulse induced cell death can be considered a dose effect with respect to the energy deposited in the cell membrane. Assuming that subcellular membranes show a similar temperature dependence in their electrical properties, the possibility that the cell lethality is triggered through permeabilization of inner membranes (in addition to that of the plasma membrane) cannot be excluded.

The threshold voltage across the membrane required for electroporation was shown to decrease with an increase in temperature, which is likely due to the increase in the membrane fluidity with temperature. This argument is supported by molecular dynamics simulations which show an increased probability for pore formation with temperature. Based on a three layer (medium, membrane, cytoplasm) cell model and using the dielectric spectroscopy results it was concluded that the induced membrane voltage also decreases with an increase in temperature. Consequently, the threshold voltage needed to induce electroporation must decrease at a faster rate than the induced membrane voltage from the electric field.

## ACKNOWLEDGEMENTS

I would like to express my gratitude to my advisor, Dr. Karl H. Schoenbach, for his unlimited patience and support for me throughout my graduate studies. I would also like to thank him for his time, even through retirement. I would also like to thank the following for their support and time serving on my dissertation committee: Dr. Jurgen Kolb, Dr. Richard Heller, Dr. Dharamsi, and Dr. Shirshak Dhali.

I would also like to thank Dr. Beebe and Dr. Joshi for their support and talks in regards to my research. Thank you to Robert Minahan for guiding me in my early years at the Center for Bioelectrics. I would also like to thank my fellow students, Chandra Bajracharya, Mark Migliaccio, Jie Zhuang, Salleh Sheikh and Subhash Kalluri for their help in the classroom and in the lab.

In regards to the biological studies, I would like to share my sincere appreciation to Ellen Yang for all of her help and support. I would also like to mention Angela Bowman, Betsy Gregory and Barbara Carroll for their help as well.

Most importantly, I would like to thank my parents; Jane and James Camp, for their unlimited support my entire life. I would like to thank them for molding me into the man I am today, and providing me with highest achievable education. All of my success today is owed to them, and I will be forever grateful.

## TABLE OF CONTENTS

	Page
LIST OF TABLES .....	x
LIST OF FIGURES .....	xi
Chapter	
I. INTRODUCTION .....	1
I.I. INTRODUCTION TO SUBNANOSECOND PULSES .....	1
I.II. MOTIVATION .....	2
I.III. PREVIOUS SUBNANOSECOND RESEARCH .....	7
I.IV. TOPIC OF THE DISSERTATION .....	8
II. BACKGROUND .....	10
II.I. 800 PICOSECOND, > 100 kV/cm CONDITIONS .....	10
II.II. 200 PICOSECOND, < 100 kV/cm CONDITIONS .....	14
II.III. EFFECT OF PULSED ELECTRIC FIELDS (PEF) AND TEMPERATURE ON BACTERIA .....	16
II.IV. CONCLUSION FROM PREVIOUS RESEARCH RESULTS .....	17
III. TEMPERATURE DEPENDENCE ON THE ELECTRICAL PROPERTIES OF THE CELL .....	20
III.I. TDR ANALYSIS OF THE CELLS AND GROWTH MEDIUM .....	20
III.II. IMPEDANCE AND RELAXATION TIME RELATIONSHIP .....	22
III.III. VOLTAGE INDUCED ACROSS THE MEMBRANE .....	24
III.IV. TEMPERATURE EFFECT ON RESTING POTENTIAL .....	27
IV. TEMPERATURE EFFECTS ON PLASMA MEMBRANE .....	29
IV.I. STRUCTURE OF THE PLASMA MEMBRANE .....	29
IV.II. HEAT SHOCK VERSUS HOMEOVISCIOUS ADAPTATION .....	31
IV.III. TEMPERATURE EFFECTS ON ELECTROPORATION .....	33
V. SUBNANOSECOND PULSE GENERATORS .....	35
V.I. SUB NS PULSE GENERATORS WITH AVALANCHE TRANSISTORS AS SWITCHES .....	35
V.II. SUB NS PULSE GENERATORS WITH SOS SWITCHES .....	37
V.III. SUB NS PULSE GENERATORS WITH PHOTOCONDUCTIVE SWITCHES .....	41
V.IV. SUB NS PULSE GENERATORS WITH SPARK GAP SWITCHES .....	45
VI. DESIGN AND SETUP OF PULSE GENERATOR .....	51
VI.I. DESIGN OF SUB NS PULSE GENERATOR .....	51
VI.II. MARX BANK .....	53

VI.III.	PEAKING SWITCH.....	58
VI.III.I.	Peaking Switch Geometry.....	58
VI.III.II.	Peaking Circuit.....	59
VI.III.III.	The Effect of the Number of Stages on the Peaking Pulse.....	61
VI.III.IV.	Varying the Gap Distance.....	63
VI.IV.	TAILCUT SWITCH.....	65
VII.	DESIGN AND SETUP OF EXPOSURE CHAMBER.....	68
VIII.	VOLTAGE MEASUREMENTS.....	73
VIII.I.	VOLTAGE DIAGNOSTICS.....	73
VIII.II.	REFLECTION CONCEPT OF CAPACITIVE AND RESISTIVE LOAD.....	77
VIII.III.	DETERMINING THE VOLTAGE ACROSS THE LOAD.....	80
VIII.III.I.	Measurements.....	80
VIII.III.II.	Voltage Simulations Using PSpice.....	85
IX.	TEMPERATURE MEASUREMENTS.....	88
IX.I.	TEMPERATURE INCREASE DUE TO PULSING.....	88
IX.II.	THERMAL DECAY MEASUREMENT.....	91
IX.III.	TEMPERATURE CONTROL.....	94
X.	BIOLOGICAL PROTOCOLS AND PROCEDURES.....	96
X.I.	CELL CULTURE AND TRYPAN BLUE EXCLUSION ASSAY.....	96
X.II.	EXPERIMENTAL PROTOCOL.....	97
X.III.	MEASUREMENT OF TEMPERATURE DEPENDENCE ON TRYPAN BLUE UPTAKE.....	97
XI.	EXPERIMENTAL RESULTS.....	99
XI.I.	EFFECT OF TEMPERATURE WITHOUT PULSE APPLICATION.....	99
XI.II.	TRYPAN BLUE EXCLUSION FOUR HOURS AFTER EXPOSURE TO PEF.....	100
XI.III.	TRYPAN BLUE EXCLUSION IN TERMS OF ENERGY DENSITY.....	102
XI.IV.	ELECTRIC FIELD THRESHOLD.....	104
XI.V.	CELL DEATH: IMMEDIATE MEMBRANE PERMEABILIZATION OR APOPTOSIS.....	105
XII.	DISCUSSION OF RESULTS.....	107
XII.I.	MEMBRANE VOLTAGE.....	107
XII.II.	MEMBRANE CHARGES VERSUS MEMBRANE DOSE EFFECT.....	110
XII.II.I.	Membrane Charges in Relationship to the Temperature.....	110
XII.II.II.	Membrane Dose Effect in Relationship to the Temperature.....	112
XII.III.	MEMBRANE VISCOSITY.....	115
XIII.	SUMMARY.....	118
	REFERENCES.....	121
	APPENDIX A: NANO AND SUBNANOSECOND SPARK GAP SWITCHES.....	137



A.1.	INITIATION OF SUBNANOSECOND BREAKDOWN.....	137
A.2.	BREAKDOWN .....	141
A.3.	CIRCUIT PARAMETERS.....	144
A.4.	ELECTRODE SHAPE AND MATERIAL .....	146
A.5.	OPTIMIZATION OF SPARK GAP FOR SUB-NS BREAKDOWN .....	148
A.6.	COMPARISON TO OTHER SUBNANOSECOND SWITCHES .....	149
APPENDIX B: MEASUREMENTS OF THE ELECTRICAL PROPERTIES OF CELLS BY MEANS OF DIELECTRIC SPECTROSCOPY .....		151
APPENDIX C: MOLECULAR DYNAMICS SIMULATION APPROACH .....		155
VITA.....		156

## LIST OF TABLES

Table	Page
3.1. Permittivity (a) and conductivity (b) of cytoplasm, plasma membranes of Hepa 1-6 cells, and the growth medium at 25°C, 37°C, 42°C and 47°C [48]. .....	20
6.1. The breakdown voltage and E/n ratio of the peaking switch, along with the pulse width of the peaking pulse for an 8 kV and 12 kV input voltage to an 8 stage Marx Bank. ....	64
7.1. Permittivity and conductivity of the medium used for the cell suspension depending on temperature. Also listed is the resulting capacitance and resistance of the sample. ....	69
8.1. The amplitude of the voltage across the load will be determined by decreasing the amplitude of the voltage measured with the voltage probe in front of the load by the percentage given at its respected temperature. ....	84
11.1. Trypan blue uptake of cells immediately after pulsing and four hours later (Avg.; average value, Std: standard deviation) . There was no difference between the sham at 47°C and results of measurements at 25°C (not shown). The measurements at 61 kV/cm and at 84 kV/cm were conducted at the same electrical energy density. ....	106
12.1. Relationship between the voltage across the membrane and temperature of the medium. The applied electric field is 90 kV/cm. The electric field across the sample, $E_{med}$ , is reduced as a result of impedance of the sample, which is temperature dependent.....	108
12.2. Membrane voltage for threshold electric field experiments (Fig. 11.4). ....	109

## LIST OF FIGURES

Figure	Page
1.1. (a) Basic structure of a mammalian cell. A cell membrane (aka plasma membrane) surrounds the cell and the intracellular components (nucleus shown here). A separate membrane surrounds the nucleoplasm which makes up the nucleus. (b) The double cell model with the circuit components [1] .....	3
1.2. Different types of electrodes for exposing cancerous tissue (dark gray) with electric fields.....	4
1.3. A prolate spheroidal reflector, or irradiating antenna, can be used to focus electromagnetic energy at the second focal point within the tissue. The input magnetic wave is launched from the first focal point .....	5
1.4. A step function with a risetime of 200 ps is fed into the first focal point leads to an inverted pulse with a pulse width equal to 200 ps at the second focal point. The functions were determined by using MAGIC software [37] .....	6
2.1. Trypan blue exclusion of B16 cells exposed to 800 ps pulses of varying electric field strength and pulse number. The results were plotted in terms of energy density in which the conductivity was chosen to be that of the medium (100 $\Omega$ -cm). The threshold of trypan blue uptake is approximately 0.8 kJ/cm <sup>3</sup> .....	11
2.2. Data from the 800 ps experiments are compared with B16 cells exposed to 10 ns pulses with less energy density. The data does not align in terms of energy density, but does when plotted verses the empirical scaling parameter. The scaling parameter was derived from two separate experiments in which data was plotted in terms of electrical impact ( $E \cdot \tau$ ) and a dose effect ( $E^2 \cdot N$ ) [4].....	12
2.3: The experimental results from [2] (200 ps, 25 kV/cm) compared with the 800 ps experiments [1] in terms of energy density .....	15
2.4. The data from reference [2] plotted in terms of the empirical scaling parameter does not show the same effect due to cell death being attributed to heating rather than the pulse electric fields.....	18
3.1. Single shell cell model with the circuit diagram .....	22
3.2. Cell exposed to pulse durations greater than the relaxation time of the cytoplasm, and less than the relaxation time of the membrane can be expressed by the membrane charging model. Cells exposed to pulses less than the relaxation time of the cytoplasm can be expressed by the dielectric model in which the permittivity plays a higher role than the conductivity [47].....	24
3.3. The external electric field will be superimposed on the electric field across the membrane due to the resting potential. As a result, the field across the membrane facing the anode will be higher than the side facing the cathode. Therefore, electroporation begins on the anode side of the cell for cells exposed to pulsed electric fields with rise times less than the charging time of the membrane. For slow rise times, the cell membrane will be charged such that the resting potential can be neglected.....	28

- 5.1. Schematic of an avalanche transistor subnanosecond pulse generator. Each transistor has an inductance associated with it, which gives the circuit a transmission line type of setup. By decreasing the capacitance of each stage ( $C_1 < C_2 < C_3 < C_4 < C_5$ ), the impedance of each stage is increased, which sharpens the risetime of the pulse. The fall time of the pulse depends on the RC time constant of the load and  $C_{out}$  ..... 36
- 5.2. Simple schematic layout of a pulse generator incorporating a single SOS switch, represented by the SOS diode. Typically,  $C_1$  will equal  $C_2$  and  $L_1$  will equal  $L_2$  ..... 38
- 5.3. The current through a shorted diode, when S1 closes, shows the oscillation of the circuit. In order for the SOS switch to open, the time between the negative and positive peak of the current across the diode needs to be twice that of the reverse recovery time of the diode. The voltage across the load is equal to the current across the load (solid black) multiplied by the resistance ..... 39
- 5.4. Concept of a pulse generator incorporating a photoconductive switch. A pulsed power source is used to charge the electrodes. The mode depends on the magnitude of the electric field across the switch prior to triggering. In the linear mode, a high energy laser source is needed (mJ) to close the switch whereas the nonlinear mode requires less energy from the laser ( $\mu$ J) ..... 41
- 5.5. Quantitative description of the development of a high voltage, subnanosecond pulse from a pulse generator layout incorporating a peaking and tailcut switch. The pulse generator (second stage) in this dissertation is an 8 stage (N) Marx Bank. A peaking switch decreases the risetime of the pulse by effectively reducing the inductance of the pulse generator [40]. A tailcut switch is used to ground the decaying portion of the pulse ..... 46
- 5.6. Concept of the peaking circuit incorporating both the peaking switch ( $S_p$ ) and peaking capacitor ( $C_p$ ). The first graph is the voltage across  $R_{k\Omega}$  with (dotted black) and without (dashed gray) the peaking capacitor while the peaking switch remains open. The second graph compares the voltage across the load with the closing of the peaking switch ..... 47
- 5.7. Concept of a differential subnanosecond pulse. Two pulses of equal magnitude but opposite polarity (gray traces) are superimposed with one another with a time difference, which will define the pulse width of the resulting pulse (black trace) ..... 49
- 6.1. (a) Conceptual layout of the subnanosecond pulse generator. An 8 stage Marx Bank feeds into a  $50 \Omega$  cable through a peaking switch. A tailcut switch is placed within the cable. The load is a conical exposure chamber. The voltage is measured with a capacitive voltage divider placed in front of the exposure chamber. (b) Photograph of the Marx Bank and peaking switch. (c) Photograph of the peaking switch and tailcut switch. The electrodes of the peaking switch are labeled "A" and "B" for discussion purposes ..... 52
- 6.2. Equivalent circuit of erected Marx Bank. The individual stage capacitance and inductance is represented by  $C_{MB}$  and  $L_w$ , respectively. The charging resistor of each stage is denoted  $R_{MB}$  and N is the number of stages ..... 54
- 6.3. The comparison of the measured voltage (solid) to the simulated voltage (dashed) for an 8 stage Marx Bank with a  $50 \Omega$  load. The black traces represent the voltage measured and simulated with a resistive voltage divider, and the gray traces are those measured and simulated with a capacitive voltage divider whose time constant is 8.3 ns (Chapter VIII) ..... 55

6.4. Voltage measured with a capacitive voltage divider across a 50 $\Omega$ load for a 1, 2, and 8 stage Marx Bank without a peaking switch. The 1 stage Marx Bank does not have oscillations in the pulse whereas the 2 and 8 stage do .....	57
6.5. The circuit diagram of the peaking circuit connected to the output of a 1 stage Marx Bank. Both the peaking switch and Marx Bank switch are represented by their respected capacitance and inductance. The capacitance of the Marx Bank switch makes up the peaking capacitor. The arrow points to the equivalent circuit, which is similar to Fig. 4.5 .....	59
6.6. (a) Voltage measured across a 50 ohm resistor with a capacitive voltage divider for a 1 stage Marx Bank whose input voltage is 13 kV. The gray trace is with a closed peaking switch, and the black trace represents an open peaking switch with a gap distance of 2 mm. (b) Same conditions as in (a) except with an 8 stage Marx Bank .....	62
6.7. Voltage measured across the load for an 8 stage Marx Bank with an input voltage of 8 kV in which the peaking switch gap distance is varied between 0 mm and 8 mm. The optimized gap distance occurs at approximately 2 mm for the 8 kV and 3 mm for the 12 kV input .....	63
6.8. Voltage measured in front of the load with varying tailcut switch gap distances. The input voltage to the 8 stage Marx Bank was 8 kV, and the peaking switch gap distance was set to 2 mm .....	66
7.1. (a) Dimensions of the exposure chamber created with MAGIC. (b) Photograph of the exposure chamber and voltage probe. (c) Photograph of the interior of the exposure chamber .....	70
7.2. Results of the electric field distribution within the sample using MAGIC. The insert shows the electrodes in dark gray and the sample in light gray. The letters "w" – "z" represent where in the sample the electric field was simulated. The highest electric field occurs in the center of the sample, and deviates less than 10% at the edges .....	71
8.1. Schematic layout of the capacitive voltage divider probe. The capacitance between the inner conductor and metal tape is denoted $C_1$ and $C_2$ is the capacitance between the metal tape and outer conductor. Milar tape (medium gray) was used as the insulating material for $C_2$ .....	74
8.2. The inductance and stray capacitance of the capacitive voltage divider probe ( $L_s$ and $C_s$ , respectively) limit the maximum frequency at which the probe exhibits linearity. The frequency of the oscillations is defined by $L_s$ and $C_s$ , and the decay time of the oscillations is defined by $R_p$ and $C_s$ . The values of $L_s$ and $C_s$ were calculated using transmission line geometries .....	75
8.3. Peaking pulse (Chapter VI) measured with a capacitive voltage divider probe in which the value of d changed from 9 mm to 2 mm, thus decreasing the decay time and increasing the frequency of the oscillation beyond the resolution of the oscilloscope (4 GHz) .....	76
8.4. Simulation of a pulse ( $\tau_{pw} = 1$ ns, $\tau_{rise} = \tau_{fall} = 200$ ps) into a resistive (80 ohm) and capacitive (5 pF) load. The black trace represents the measured incoming pulse superimposed with the reflected pulse with a time difference defined by the length of the transmission line between the measured point and the load (50 cm = 5 ns). The gray traces represent the voltage measured directly at the load. The solid traces are those of a capacitive (5 pF) and resistive load, while the dotted trace is the voltage neglecting the capacitance .....	78

8.5. Simulation ran with the same conditions as done in Fig. 8.2, except the pulse width was decreased from 1 ns to 200 ps. The amplitude of the pulse is decreased across the load since the pulse width is comparable to the charging time constant of the load, $\tau = R \cdot C = 400$ ps .....	80
8.6. The solid black traces are averages of 100 shots, and the gray is an envelope of 100 shots. (a) Average of 100 pulses of the incoming pulse determined by adding the pulse shapes of an open and shorted load, and dividing by two as done in (5.5). (b) The traces measured in front of the load at 25°C and 47°C showing the effects of temperatures on the reflected portion of the pulse .....	82
8.7. The voltage across the load determined by superimposing the reflected pulse to the incoming pulse, in which the reflected pulse was shifted to the left by 0.95 ns. The gray trace represents the voltage across the load for a sample temperature of 25°C, and the black trace is for 47°C .....	84
8.8. Reflected pulse determined by separating the input voltage from the voltage measured across the load. The capacitance, determined from the decay time of the pulse, was found to be 3.2 pF .....	85
8.9. Comparison of the simulated voltage (gray trace) and the measured voltage (black trace) in front of the load (a) and at the load (b) for a sample temperature of 25°C and 47°C .....	87
9.1. Concept of the leveling temperature ( $T_{\text{level}}$ ) of a sample due to pulsed electric fields. The temperature of the sample will be increased by $dT$ for each pulse. As the temperature of the sample is increased, the decay of the temperature increases until the loss of temperature between pulses is equal to the change in temperature due to one pulse .....	91
9.2. The measured temperature decay of the sample chamber (black) compared to the calculated temperature decay (gray) .....	92
9.3. At $t = 0$ , the temperature of the sample is at $T_1$ , and the temperature of the electrodes is at $T_0$ , which creates a large temperature gradient at the electrode-sample interface. Past 2 seconds, the temperature gradient in the electrodes as decreased, leaving a larger gradient in the sample.....	93
9.4. Calculated temperature diagram for cells within the exposure chamber exposed to a voltage of 30 kV, 200 ps, at a pulse repetition rate of 10 Hz. The diagram suggests the temperature increase due to pulsing will not be raised by more than 1°C.....	94
9.5. Conceptual layout of the experimental setup. The sample chamber was placed in a box made of plexiglass, which was heated to the desired temperature with a heat gun and a fan. The temperature of the sample was measured indirectly by placing the temperature probe in a hole of the cap 1 mm above the sample.....	95
11.1. Trypan blue exclusion versus exposure time of cells placed in a water bath of 42°C, 47°C and 52°C.....	99
11.2. Trypan blue exclusion 4 hours after experimental exposure to 1,000 and 2,000, 200 ps long pulses, dependent on temperature. The measured electric field at room temperature was kept constant at 84 kV/cm, but decreased to 78 kV/cm at 47°C. The data is based on 3 to 5 experiments each ( $n=3-5$ ). .....	101

11.3. Trypan blue exclusion results 4 hours after pulsing conditions in terms of the energy density of the medium. The red lines represent same experimental conditions (applied field and number of pulses). .....	103
11.4. Trypan blue exclusion 4 hours after experimental exposure at 47°C. The electrical energy density, $W$ , was kept constant by decreasing the pulse number for an increase in electric field strength. The dashed lines show the range of the sham results.....	105
12.1. Trypan blue exclusion 4 hours after experimental conditions ( $E_{\text{applied}} = 90$ kV/cm, 200 ps pulse width, $N = 100, 1000, 2000$ ) in terms of the scaling parameter. The red line represents same pulsing conditions (applied electric field and number of pulses). The blue represents a different scaling parameter for 42°C and 47°C.....	111
12.2. Energy density of the membrane with respect to the temperature for cells exposed to an applied electric field of 90 kV/cm and pulse numbers of 100 (left) 1000 (middle) and 2000 (right). The red line connects the data points for cells exposed to the same pulse number. Temperatures at and below 37°C create a negligible effect on the cells. For temperatures at and above 42°C, a linear relation between the trypan blue exclusion and the energy density of the membrane exists, as shown by the blue highlight. ....	113
12.3. Evolution of a pore formation due to an external electric field. At $t_0$ , the heads of the lipids are in random motion. At $t_1$ , an external electric field is applied and the lipid heads facing the cathode will align with the electric field. The heads of the lipids facing the anode will rotate to try and align, causing repulsion between them. This repulsion may cause an opening to allow the aqueous solution through the membrane as depicted at time $t_2$ [48] .....	115
12.4. Molecular dynamic simulations of a lipid bilayer exposed to a constant electric field strength of 0.5 V/nm for 1 ns at 25°C and 47°C [48].....	117

## CHAPTER I

### INTRODUCTION

#### 1.1 INTRODUCTION TO SUBNANOSECOND PULSES

The combined and/or synergistic effect of subnanosecond pulsed electric fields and temperature increase on cells is a new study within the field of Bioelectrics. The effects of temperature on cells, in the absence of pulsed electric fields, is well known (hyperthermia), whereas the effects of subnanosecond pulsed electric fields have just recently been explored experimentally [1, 2] and theoretically [3-7]. Experimental results suggest the outer membrane of the cell becomes permeabilized immediately after subnanosecond pulsed conditions above a certain energy density threshold ( $0.8 \text{ kJ/cm}^3$  for B16 cells with pulse widths equal to 800 ps). One theory is the permeabilization is caused by electroporation or electropermeabilization, which is dependent on the voltage across the membrane induced by the applied electric field [1, 4, 5, 8-10].

Electropermeabilization is defined as an increase in ionic and molecular transport across a plasma membrane due to an external electric field [4]. This type of permeabilization may be a biological effect in which the cell increases the flow of ions in and out of the cell, or a physical effect in which molecules are able to push through the membrane due to a concentration gradient of the molecules. Electroporation describes the effect in which holes, or pores, are created in the membrane allowing for flow of ions through the membrane [4]. The voltage across the membrane induced from an external electric field is superimposed to an already existing voltage (resting potential) across the membrane due to an imbalance of ion concentration on the interior and exterior of the cell. The magnitude of the resting potential has been shown to increase with an increase in temperature [11-13], which would result in an increase in the voltage induced across the membrane by an external electric field facing the anode, and a decrease in the voltage across the membrane facing the cathode [14]. The viscosity of the membrane also decreases with



an increase in temperature [15], which decreases the energy needed to induce pore formation, and/or permeabilization [16, 17]. It is therefore believed that an increase in temperature will decrease the threshold needed to induce electroporation by pulsed electric fields. This effect has theoretically been studied [7] and has been shown experimentally on bacteria with microsecond pulses [18, 19].

## **1.1 MOTIVATION**

The effect of high-intensity nanosecond electrical pulses on biological cells and tissue has received considerable attention by the scientific community, particularly in the past ten years, and has led to the establishment of the research field: Bioelectrics [20-23]. In this time domain, the rise time of the pulse is faster than the charging time of the plasma membrane of most mammalian cells, meaning that the field will pass through the membrane and into the cytoplasm. This effect can be understood qualitatively by considering the cell as an electrical circuit (Fig. 1.1), describing the various cell membranes by their capacitances and the cytoplasm which they enclose, by its resistance. Fig. 1.1(a) shows the cross section of a mammalian cell, with the only membrane-bound substructure shown being the nucleus. The cytoplasm, which fills much of the cell, contains dissolved proteins, electrolytes, and glucose and is moderately conductive, as are the nucleoplasm and the cytoplasm in organelles. The membranes that surround the cell and subcellular structures have low conductivity due to the oily nature of the phospholipids which make up the membrane. A cell can therefore be thought of as a conductor surrounded by an ideally insulating envelope, containing substructures with similar properties. The equivalent circuit of such a cell (which is considered as spherical for modeling purposes) with one substructure, the nucleus, is shown in Fig. 1.1(b).

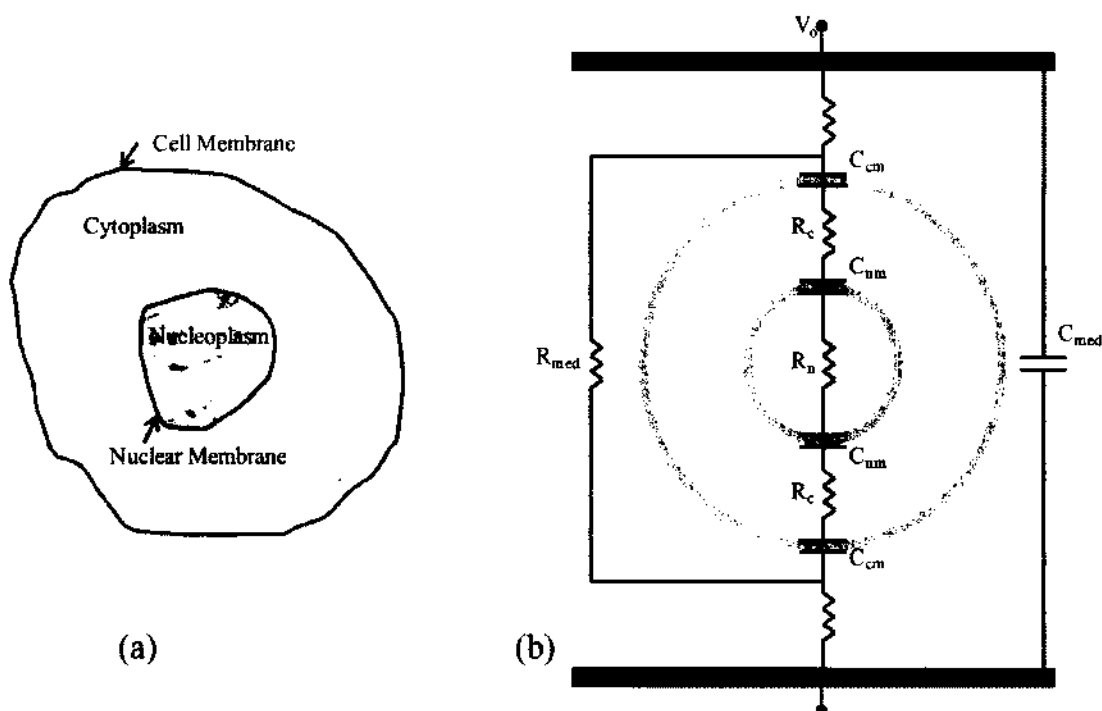


Fig. 1.1. (a) Basic structure of a mammalian cell. A cell membrane (aka plasma membrane) surrounds the cell and the intracellular components (nucleus shown here). A separate membrane surrounds the nucleoplasm which makes up the nucleus. (b) The double cell model with the circuit components [1].

If dc electric fields or pulses of long duration (compared to the charging time of the membrane) are applied, eventually, only the outer membrane will be charged. The electric field generated across subcellular membranes during charging will be zero for an ideal, fully insulating outer membrane. However, during the charging time of the outer membrane, potential differences are expected to be generated across subcellular membranes, an effect that will be stronger if the pulse rise time is shorter. Such charging times are in the submicrosecond range for human cells [1].

If the electric field is sufficiently large, it can have pronounced effects on intracellular organelles. High-voltage pulses that are nanoseconds to hundreds of nanoseconds long have been shown to penetrate into living cells to permeabilize intracellular organelles [22, 23] and release  $\text{Ca}^{2+}$  from the endoplasmic reticulum [24-26]. These short pulses provide a new approach for

physically targeting intracellular organelles with many applications including activation of platelets and release of growth factors for accelerated wound healing [27] and precise control of apoptosis [28- 31]. It has also been shown by Nuccitelli et al. that such pulsed electric fields cause shrinkage and even complete elimination of melanoma tumors [32]. Such tumors have successfully been eradicated in mice with pulsed electric fields with pulse widths of 300 ns with a 30 ns rise time and electric field strengths reaching 50 kV/cm [32, 33]. The penetrating electric field caused the tumor cell nuclei to shrink, while stopping the flow of blood to the tumor, which led to the tumor's death. Two separate treatments of 100 to 300 pulses were needed for complete remission [32, 33]. The electric field was, in these studies, applied with needle or clamp electrodes as shown in Fig. 1.2.

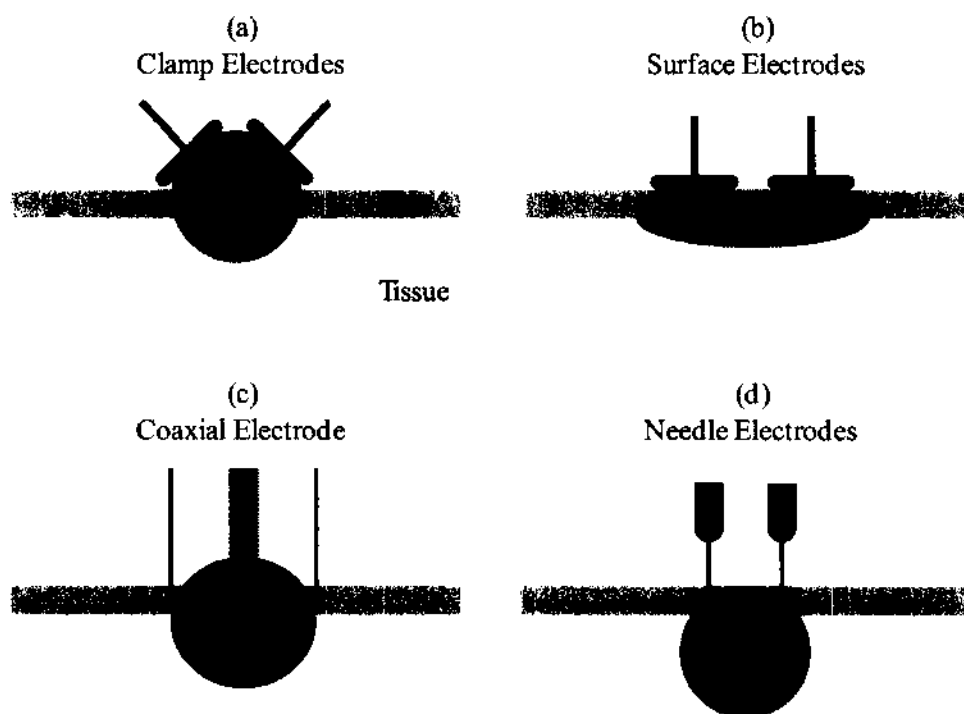


Fig. 1.2. Different types of electrodes for exposing cancerous tissue (dark gray) with electric fields.

The disadvantage of such electrodes is they can only apply electric fields on the surface of the skin. Needle electrodes may penetrate a small distance under the skin, but in order to move the electric field location, the needle must be removed and penetrate the new position. Deeper lying tissue, such as the liver or pancreas cannot be accessed with needle or clamp electrodes, unless surgical methods are used.

Another possibility is to use a catheter to deliver the electric field [34], but even this requires minimal surgery. By transitioning from the nanosecond to the subnanosecond regime, the electric field can be applied non-invasively by a reflector which focuses the electric field into the tissue, as shown in Fig. 1.3 [1]. The impulse at the second focal point of the IRA (within the tissue) is the differentiated signal of the input function fed into the reflector. The pulse width of the impulse (equal to the input of the risetime of the input function) determines the spatial resolution of the focal point, in that a shorter pulse width allows for a higher spatial resolution [35]. In order to achieve a spatial resolution on the order of 1 cm, pulses with rise times on the order of 100 ps are required [1].

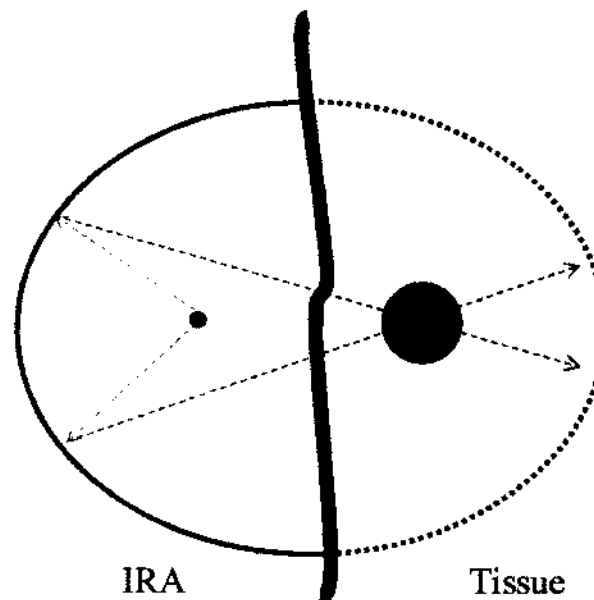


Fig. 1.3. A prolate spheroidal reflector, or irradiating antenna, can be used to focus electromagnetic energy at the second focal point within the tissue. The input magnetic wave is launched from the first focal point.

Schoenbach et al. have shown that sufficiently large electric field strengths (100's kV/cm) are needed to induce cell death with subnanosecond pulses (800 ps) [1]. The amplitude of the impulse is proportional to the amplitude of the input function multiplied by the reciprocal of the risetime of the input function [35]. Consequently, impulse voltages with subnanosecond rise times will account for higher electric field strengths at the second focal point than fields produced with nanosecond impulse rise times. The maximum attainable electric field with the antenna setup with current and near future technology at the focal point is no more than 50 kV/cm, which is due to attenuation of the signal within the tissue [36]. Therefore, we can expect the tissue to be exposed to monopolar electric field pulses with durations ranging from 100 ps to 200 ps, with electric fields of 100 kV/cm and less (ramp function input). This has been modeled, using MAGIC software [37], in which a ramp function with a 200 ps risetime is fed into the input and the impulse is simulated at the second, or output focal point (Fig. 1.4). The medium in the simulation was chosen to be water, which has a dielectric constant of 81.

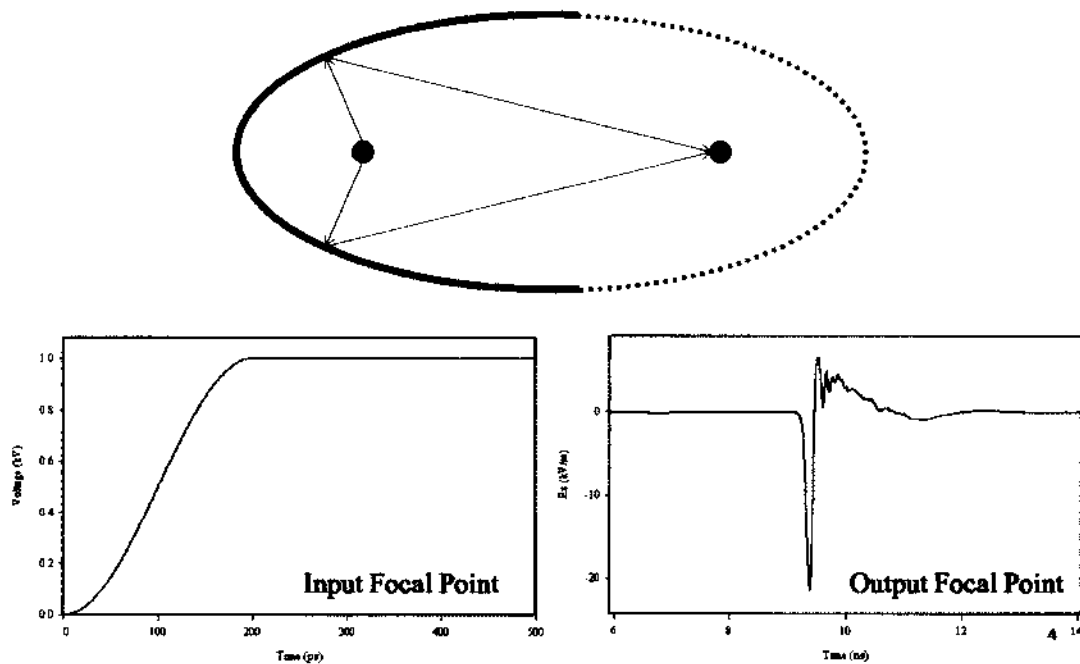


Fig. 1.4. A step function with a risetime of 200 ps is fed into the first focal point leads to an inverted pulse with a pulse width equal to 200 ps at the second focal point. The functions were determined by using MAGIC software [37].

The placement of the electric field can be moved easily by changing the position of the reflector. Such a system would not need surgical methods to reach deeper lying tissue. Subnanosecond pulses will ultimately allow medical applications for delivery of pulsed electric fields without invasive electrodes, using antennas instead. This same setup can also be used for medical imaging in which the reflected waves from a lower input power signal are determined by the electrical properties of the tissue [38]. It has been shown by Fear et al. that cancerous tissue has different dielectric properties than healthy tissue [39].

### **1.III PREVIOUS SUBNANOSECOND RESEARCH**

In an effort to study the effects of subnanosecond pulses on cells, experiments were conducted on B16 mouse melanoma cells and the energy densities required for trypan blue uptake, considered a measure for cell death, have been determined [1]. For durations of 800 ps, electric fields varying from 150 kV/cm to almost 1 MV/cm, and pulse numbers up to 20,000, it was determined that the threshold in energy density required to induce cell death was approximately  $0.8 \text{ kJ/cm}^3$ . At an energy density of  $5 \text{ kJ/cm}^3$  90% of the cells died [1, 2]. In these studies the initial temperature of the suspension was room temperature ( $22^\circ\text{C}$  to  $25^\circ\text{C}$ ) and, because of the relatively low repetition rate of approximately 10 Hz, the temperature increase due to pulsing was less than  $10^\circ\text{C}$ , and thermal effects were therefore considered to be negligible.

In follow-up studies where the pulse width was decreased to 200 ps at a constant electric field intensity of 25 kV/cm [2], using the same cell line as in the 800 ps studies, the results with respect to energy density were quite similar to those obtained with 800 ps pulses. Due to the low value of the electric field, the number of pulses needed to be increased by two orders of magnitude, resulting in  $2.4 \cdot 10^6$  pulses being applied for 90% cell death. However, in this case, it was found that the sample temperature played a major role in inducing cell death. In the 200 ps studies the temperature of the sample was measured with an optical temperature probe (TI C-11000 A, Neoptix, Canada) during pulsing. The temperature of the sample reached values as

high as 47°C after a 10 minute exposure, due to Joule heating caused by the high repetition rate of the pulsed electric fields (10 kHz, in a burst mode with 40 pulses per burst). This temperature increase contributed much to the measured cell death, which was confirmed by measuring the effect of the temperature alone on the cells by heating the sample in a water bath to similar temperatures as obtained with Joule heating. For exposures at 47 °C the survival rate, which was not affected by the high temperature for at least the first two minutes, decreased to approximately 80% at 5 minutes, and decreased to 10% for a 10 minute exposure. The effects of the pulsed electric fields and temperature could not be separated since the heating of the sample was due to the applied pulses. More on these studies are discussed in Chapter II.

#### **I.IV TOPICS OF THE DISSERTATION**

The focus of this dissertation is to study the effects of subnanosecond pulses on mammalian cells (liver cancer cells) in suspension at different temperatures. Expectations are that an increase in temperature will cause the cells to be more susceptible to the pulsed electric fields whether by increasing the fluidity of the membrane (Chapter IV), or changing the electrical properties of the cell (Chapter III). The results may be helpful in designing future non-invasive techniques in delivering the applied electric field to a cancerous target within the tissue. If heating the cells does make the cells more susceptible to the pulsed electric fields, then the question of how to heat the target within the tissue while applying electric fields will need to be addressed in future designs. The results can also be used to determine a threshold effect of cell death in that medical imaging would need to be completed at electric fields below this threshold to keep from harming the cells.

The effects of the pulsed electric fields and temperature of the cell suspension needed to be studied separately and combined. This has been accomplished by applying low energy pulses at a slow repetition rate (< 10 Hz) to a sample to minimize the temperature increase from ohmic heating. The cells were pulsed at room temperature (25°C), physiological temperature (37°C),

42°C, and 47°C in which the cell suspension was heated externally (Chapter IX). In order to apply the pulses, a subnanosecond pulse generator was designed and built based on the concept in reference [40] (Chapter VI). The pulse generator is capable of delivering a pulse with a width of 200 ps (FWHM), and an amplitude up to 20 kV. The pulse width was kept constant at 200 ps, and the electric field was varied from 52 kV/cm to 95 kV/cm. In order to expose the cells to the electric fields, a coaxial chamber was designed and built which provided a uniform electric field across the sample with less than 10% deviation (Chapter VII). A capacitive voltage divider was used to measure the incoming voltage to the load, which was superimposed with the reflected voltage from the sample, in which both were used to determine the voltage at the load (Chapter VIII).

Cell death has been determined by using trypan blue assay four hours after exposure, and membrane permeabilization was determined by using trypan blue immediately after pulsing. Trypan blue is normally impermeant to healthy cells. When cell membrane integrity is compromised, the dye is able to enter the cell and bind to protein, making the cell appear blue. Cells that take up this dye several hours after exposure to electrical pulses are usually considered dead or dying. In order to determine the temperature effect on permittivity and conductivity, which results in changing the electric field distribution across the cell membrane and energy transfer into the cell, particularly into the cell membrane, the electrical characteristics of the cell were measured using dielectric spectroscopy (Appendix B). The effect of increased temperature on pore formation in the cell membrane was modeled by means of molecular dynamic simulations (Appendix C).



## CHAPTER II

### BACKGROUND

Only in the past few years has the effect of subnanosecond pulses been explored on cells [1-3, 41]. In these experiments, the temperature increase due to pulsing was an unavoidable and sometimes undesired effect. The cells were exposed to a waterbath in order to distinguish between the effects of the pulsed electric fields, and increase in temperature. There are several references on the effect of temperature on cells, but very few that explore the effect of pulsing at different temperatures [42, 43]. However, these experiments involved pulses of durations much greater than 1 ns and were explored on bacteria. The next few sections will discuss what has already been studied in the field of applying subnanosecond pulses to cells, as well as pulsing cells (bacteria) at different temperatures.

#### II.1 800 PICOSECOND, > 100 kV/cm CONDITIONS

In an effort to study the effects of these short pulses on cells, 800 ps pulsing experiments were conducted on B16 mouse melanoma tumor cells; trypan blue exclusion was plotted four hours after pulsing, which was considered a measure for cell death, in relation to the electrical energy density [1]. The electrical energy density,  $W$ , for N square wave pulses is

$$W = \sigma \cdot N \cdot E^2 \cdot \tau \quad 2.1$$

in which  $E_0$  is the applied electric field,  $\sigma$  is the conductivity of the medium (100  $\Omega$ -cm), and  $\tau$  is the pulse width (800 ps). The experiments were conducted with a subnanosecond pulse generator [40] which generated 800 ps pulses, with electric field strengths varying between 100 kV/cm and 1 MV/cm. The gap of the exposure chamber varied between 3.15 mm and 10.67 mm in order to achieve the wide range of electric field strengths, and the pulse number ranged from 100 to 20,000. The electrical energy density ranged between 0.5 kJ/cm<sup>3</sup> and 5.5 kJ/cm<sup>3</sup>. In these studies, the initial temperature of the suspension was room temperature (22°C to 25°C) and,

because of the relatively low repetition rate of approximately 10 Hz, the temperature increase due to pulsing was less than 10°C. This was confirmed by measuring the sample temperature for a data point at 3.6 kJ/cm<sup>3</sup> (150 kV/cm, 20,000 pulses) during pulsing with an optical probe (FOT M fiber optic temperature sensor). In this case the temperature increase was 6°C, raising the sample temperature to a value approximately 7°C below the physiological temperature of 37°C. Thermal effects were therefore assumed to be negligible. The results are shown in Fig. 2.1.

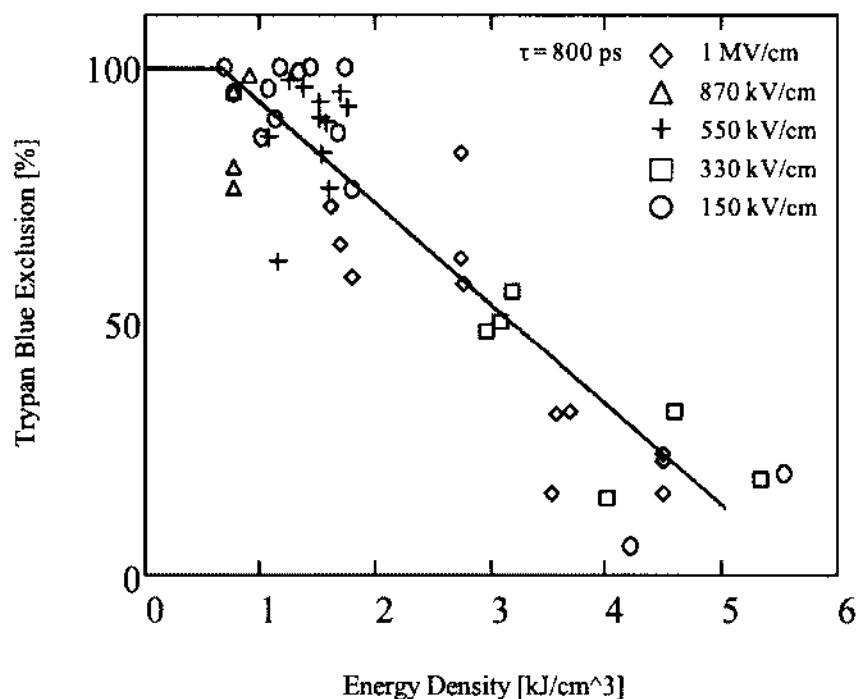


Fig. 2.1. Trypan blue exclusion of B16 cells exposed to 800 ps pulses of varying electric field strength and pulse number. The results were plotted in terms of energy density in which the conductivity was chosen to be that of the medium (100  $\Omega$ ·cm). The threshold of trypan blue uptake is approximately 0.8 kJ/cm<sup>3</sup>.

The threshold in energy density, required to induce cell death was found to be 0.8 kJ/cm<sup>3</sup>. At an energy density of approximately 5 kJ/cm<sup>3</sup>, 90% of the cells died [1]. The results seem to indicate that trypan blue uptake is a dose effect, scaling with the electrical energy density; however, this dependency on energy density does not hold true when the pulse duration is increased.

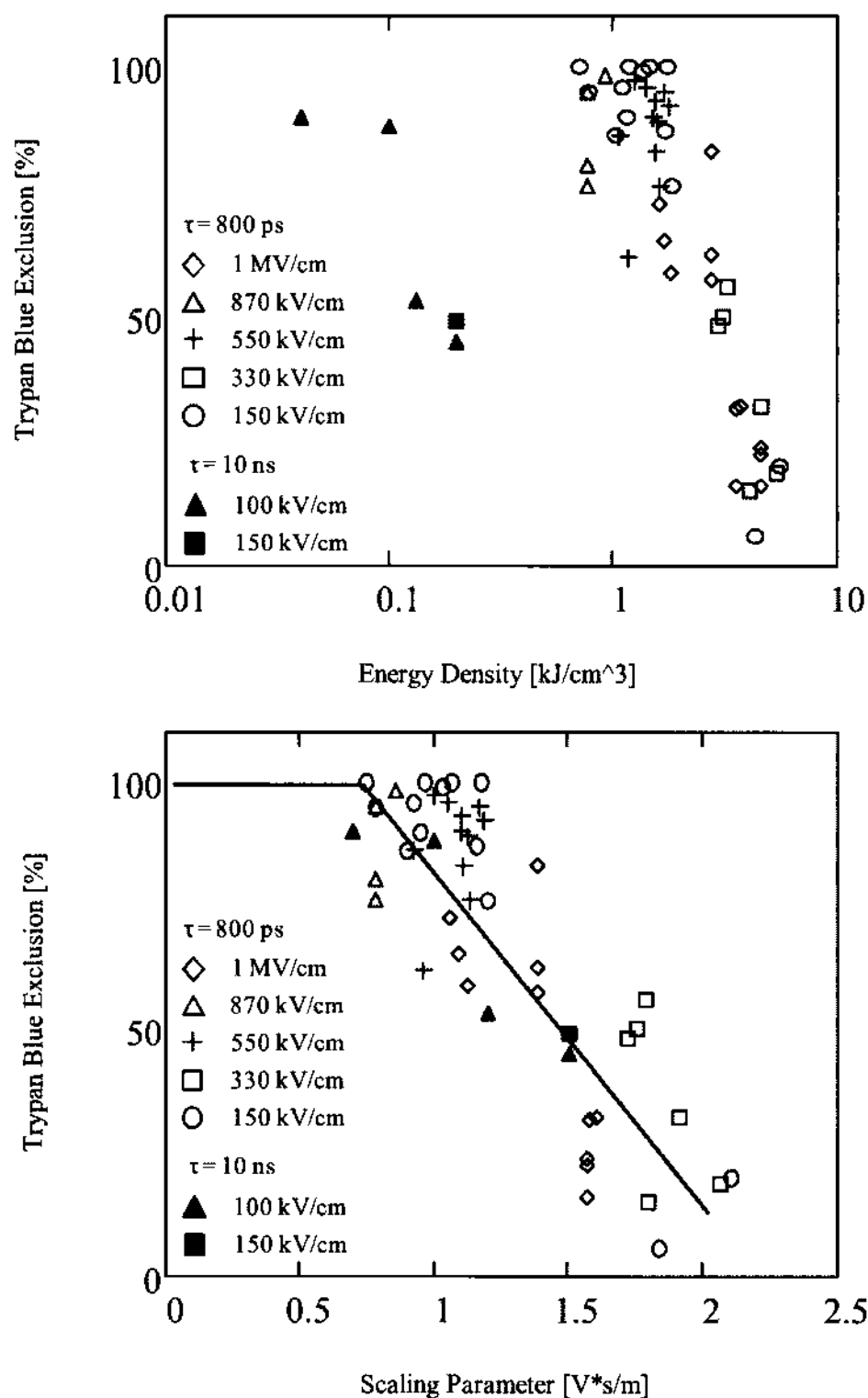


Fig. 2.2. Data from the 800 ps experiments are compared with B16 cells exposed to 10 ns pulses with less energy density. The data does not align in terms of energy density, but does when plotted versus the empirical scaling parameter. The scaling parameter was derived from two separate experiments in which data was plotted in terms of electrical impact ( $E \cdot \tau$ ) and a dose effect ( $E^2 \cdot N$ ) [4].

This is shown when the 800-ps data (Fig. 2.1) is compared with trypan blue uptake data obtained with pulses 10 ns long (Fig. 2.2(a)). In Fig. 2.2(a) experimental results on trypan blue exclusion reported in [45] were complemented by results of a recent experimental study where the procedures were kept exactly the same as described in [45] (which are identical to those described in [1]). The results show clearly that the observed biological effect is not an energy density-dependent effect, but follows a different scaling law. Such a scaling law for biological effects of pulses with durations short compared to the plasma membrane charging time constant, but longer than the dielectric relaxation time of the cytoplasm, was discussed in [1]. The law is based on the hypothesis that in this pulse duration range (which covers both 800 ps as well as 10 ns pulses), any bioelectric effect is due to membrane charging, whether it is at the plasma membrane or subcellular membranes. It postulates that identical effects can be expected if the product of applied electric field intensity  $E$ , pulse duration  $\tau$ , and the square root of the number of pulses  $N$  is kept constant. By replacing the energy density in the ordinate of Fig. 2.2(a), by an empirical scaling parameter (2.2), the trypan blue data for 800 ps and 10 ns can be described by the same parameter, shown in Fig. 2.2(b).

$$S = E_0 \cdot \sqrt{N} \cdot \tau \quad 2.2$$

Equation 2.2 combines the effects of energy density and the electrical impact factor,  $E_0 \cdot \tau$  [4]. The intensity of the observed effect (scaling factor) is represented by  $S$ . The threshold scaling factor needed for cell death for the 800 ps experiments is approximately 0.75 V·s/m. In order to achieve at least 80% cell death, a scaling factor of at least 1.8 V·s/m was needed, which equates to 20,000 pulses at 160 kV/cm for a 800 ps pulses. It indicates that the observed effect of trypan blue uptake is a primary effect caused by membrane charging (and subsequent poration) and is not a secondary bioelectric effect, such as an effect caused by the disintegration of the membrane after apoptosis has set in.

## II.II 200 PICOSECOND, < 100 kV/cm CONDITIONS

In reference [2], 200 ps pulsing experiments were conducted on B16 mouse melanoma tumor cells (same cell line used in reference [1]) in which cell viability was determined 18 hours after pulsing by trypan blue exclusion and a water soluble tetrazolium (WST) assay. In order to determine the effects of such short pulses at a more reasonable electric field, which could be expected with the use of an antenna, the electric field strength was reduced and kept constant at 25 kV/cm. The pulse generator used was an FPG 5-P, capable of delivering 5 kV, 200 ps pulses with a pulse repetition rate up to 10 kHz. An open sample chamber was designed such that the sample could be exposed to a uniform electric field of strength 25 kV/cm, while measuring the temperature with a Neoptix temperature sensor (TI C-11000 A, Neoptix, Canada) during the applied pulses. In this case, the sample temperature played a major role in inducing cell death.

Initial experiments conducted at a pulse repetition rate of 300 Hz, with a pulse number equal to 1,000 and 10,000 pulses resulted in no increase in the temperature of the sample as a result of the pulsing and no indication of cell death. In order to obtain cell death, based on the experiments shown in Fig. 2.1, an electrical energy density greater than  $0.8 \text{ kJ/cm}^3$  would be needed (scaling factor greater than  $0.75 \text{ V-s/m}$ ). With an electric field strength of 25 kV/cm, and a pulse width of 200 ps, more than 0.6 million pulses are needed to obtain values within the needed range for cell death. In order to decrease the amount of time during pulsing, the pulse repetition rate was increased to 10 kHz. However, the increase in frequency caused the temperature (due to Ohmic heating) of the sample to reach values greater than  $60^\circ\text{C}$ . In order to limit the increase in temperature, the pulses were applied in bursts, in which the bursts were repeated every 10 ms. The number of pulses per bursts was chosen such that the total time of pulsing was kept constant (10 min.). The temperature of the sample (starting temperature of  $23^\circ\text{C}$ ) with respect to the number of pulses was equal to  $37^\circ\text{C}$ ,  $42^\circ\text{C}$ , and  $47^\circ\text{C}$  for 1.2 M, 1.8 M, and 2.4 M pulses, respectively. The M stands for million. In each case, after 150 s into pulsing, the temperature of the sample leveled off (leveling temperature, Chapter IX). The results of the

200 ps experiments are compared to the 800 ps experiments in terms of the energy density in Fig. 2.3.

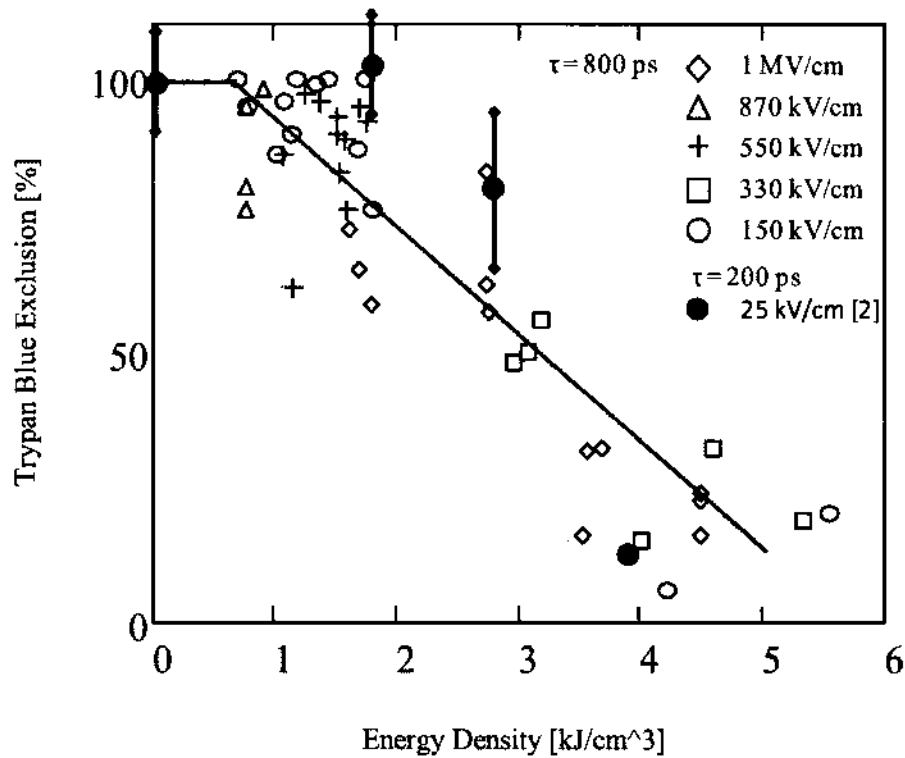


Fig. 2.3: The experimental results from [2] (200 ps, 25 kV/cm) compared with the 800 ps experiments [1] in terms of energy density.

The data point at 0 kJ/cm³ represents the sham control. For a 10 minute exposure of 1.2 M pulses (1.9 kJ/cm³), the temperature increased and leveled off at 37°C after 2 minutes, and there was no indication of cell death. The viability decreased to 80% for a ten minute exposure of 1.8 M pulses (2.9 kJ/cm³) in which the temperature increased to 42°C after 2 minutes and leveled off. For 2.4 M pulses (3.9 kJ/cm³), the temperature of the sample reached 47°C after 2 minutes of the 10 minute exposure (10 kHz, in a burst mode with 40 pulses per burst), and the viability decreased to 20%.

In order to distinguish between the effects of temperature and pulsing, the cells were exposed to the respected leveling temperature obtained with Joule heating (37°C, 42°C, 47°C) in a waterbath for 10 minutes. For exposure temperatures equal to 37°C and 42°C, there was no

indication of cell death after 10 minutes, suggesting that the cell death for an N of 1.8 M was attributed to the pulsed electric fields. For exposures at 47°C the survival rate, which was not affected by the high temperature for at least the first 2 minutes, decreased to approximately 80% at 5 minutes, and to 10% for a 10 minute exposure. This would suggest that the cell death for an N of 2.4 M pulses was attributed to the heating of the sample. However, there was an indication of cell death at 1.8 M pulses which was not attributed to the temperature alone, suggesting that, the pulsed electric field as well as the temperature had an effect on the cells for an N of 2.4 M pulses.

### **II.III EFFECT OF PULSED ELECTRIC FIELDS (PEF) AND TEMPERATURE ON BACTERIA**

To my knowledge, studies of the temperature dependence of pulsed electric field exposed cells, independent of Joule heating have only been performed on bacteria [42, 43]. The pulse durations in these cases were on the order of microseconds. There was a clear indication of a synergistic effect for bacteria pulsed at 60°C compared to those pulsed at 30°C [42]. The initial live cell count was  $10^9$  cells/cm<sup>3</sup> at 30°C, which decreased to  $10^7$  cells/cm<sup>3</sup> when the temperature was increased from 24°C to 60°C for 10 seconds. When exposed to 60 pulses, of amplitude 30 kV/cm, the survivability decreased to  $10^4$  cells/cm at 30°C, and was immeasurably small at 60°C.

The cause of cell death of bacteria due to the applied electric fields was assumed to be due to electroporation. The increase in temperature causes an increase in the conductivity of the medium and cytoplasm of the cell, as well as a decrease in the viscosity of the membrane. Based on the increase in membrane and cytoplasm conductivity, it was concluded that the observed increase in cell death at higher temperature is due to a more rapid increase in membrane potential, leading to an earlier breakdown of the membrane [42]. Similar results were obtained with *E. coli* [43] in which an increase in bacteria death was observed when pulses at elevated temperatures

were applied. Here, it was also assumed that this effect is due to a decrease in membrane viscosity.

## **II.IV CONCLUSIONS FROM PREVIOUS RESEARCH RESULTS**

The results of the 200 ps experiments fit in with the trypan blue exclusion versus the energy density of the 800 ps experiments, suggesting the energy density relationship follows not only for pulses of 800 ps, but for 200 ps pulses as well. However, such a statement may be misleading since the 800 ps experiments were performed under conditions where the temperature of the sample never reached values above physiological temperature (37°C) and the temperature of the two data points for the 200 ps experiments were above 37°C.

A change in temperature of the cell sample will cause a change in the electrical properties of the cell membrane and cytoplasm such that the ratio of the electric field across the membrane and cytoplasm will change (Chapter XI). A change in temperature will also change the fluidity of the membrane in that a higher fluidity decreases the threshold needed for electroporation or permeabilization (Chapter XII). The cell death for the 200 ps experiments conducted at 2.9 kJ/cm<sup>3</sup> occurred at a temperature of 42°C and cannot be directly compared to the 800 ps experiments, which were performed at temperatures less than 37°C. The same can be said for the 3.9 kJ/cm<sup>3</sup> data point, except the temperature of the 200 ps experiments was at 47°C which clearly was the major cause of cell death. If the 200 ps experiments are compared to the 800 ps experiments in terms of the scaling factor (Eq. 2.2), then the results do not line up, as shown in Fig. 2.4.



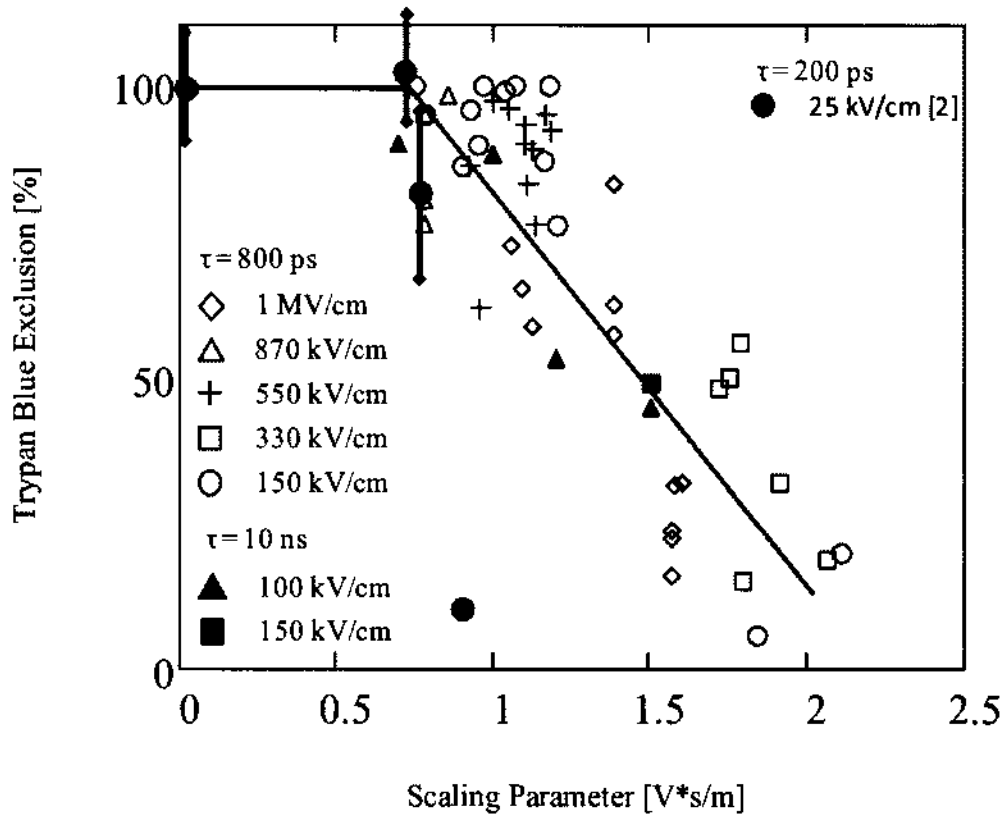


Fig. 2.4. The data from reference [2] plotted in terms of the empirical scaling parameter does not show the same effect due to cell death being attributed to heating rather than the pulse electric fields.

The data points for the 1.2 M and 1.4 M pulse number line up with the 800 ps and 10 ns data. However, the 2.4 M pulse number data is clearly outside the trend. Under the assumption that the results due to pulsing should follow the same scaling law, the effects at 2.4 M shots are not caused by pulsing, but by the temperature. The scaling law predicts that at 200 ps and 25 kV/cm, at least 12 M pulses are needed to induce 90% cell death. This would also suggest that a higher energy density is needed to induce cell death for a shorter pulse width, which is the trend as shown in Fig. 2.2(a). The 800 ps pulses required a higher energy density for the same effect as the 10 ns experiments. Stronger conclusions of this experiment can be made if the temperature effects and pulsing effects can be separated.

Based on the results given in [42, 43] for the bacteria, an increase in temperature from the cultured temperature of the cells make them more susceptible to pulsed electric fields by

decreasing the fluidity of the plasma membrane. Although the bacteria contains a cell wall (mammalian cells do not), the wall is more conductive than the membrane (2.5 mS/m), and porous such that it does not disturb the flow of small molecules [46]. Similar results can be expected, in that pulsed electric fields will have a greater effect on mammalian cells at temperatures above the physiological temperature of the cell (37°C). This effect may have been observed in the 200 ps experiments for the pulse number of 1.8 M pulses. The scaling law (based on the 800 ps and 10 ns experiments) predicts a higher scaling factor of approximately 1.25 Vs/m for 20% cell death. Yet, less than 1 Vs/m was needed when the cells were exposed to a temperature of 42°C during the applied pulses.

The experiments conducted in [1, 2] were conducted on mammalian cancer cells cultivated at 37°C and pulsed at an initial temperature between 22°C and 25°C. Already, this would suggest that the cells would be more resistive to the effects of the pulsed electric fields due to a decrease in the fluidity of the membrane as a result of the decrease in temperature. In order to see an effect, the temperature would need to be raised, as was done for this dissertation.

## CHAPTER III

### TEMPERATURE DEPENDENCE ON THE ELECTRICAL PROPERTIES OF THE CELL

The analytical approach used in this chapter to determine the membrane voltage is linear in that temporary changes in the electrical parameters of the cell, such as changes caused by electroporation, are not considered. Such an approach is sufficient for determining the electrical effects of the cell up to the threshold effect in which nonlinearities of the cell occur. Models which include the nonlinear effects have been presented elsewhere [47].

#### III.1 TDR ANALYSIS OF THE CELLS AND GROWTH MEDIUM

The measured conductivity and permittivity of the cytoplasm, plasma membrane, and the medium derived by TDR analysis with respect to temperature are shown in Table 3.1 (Appendix B).

Relative Permittivity						
Temperature	Membrane		Cytoplasm		Medium	
	Avg.	Std.	Avg.	Std.	Avg.	Std.
25°C	13.9	0.19	76.3	2.6	79.3	3.4
37°C	15.1	0.31	100	1.5	72.7	2.8
42°C	16.5	0.64	115	4.9	67.6	2.5
47°C	18	0.17	146	4.8	64.1	3.1

Conductivity						
Temperature	Membrane [10 <sup>-5</sup> S/m]		Cytoplasm [10 <sup>-1</sup> S/m]		Medium [S/m]	
	Avg.	Std.	Avg.	Std.	Avg.	Std.
25°C	2.44	0.28	3.79	0.08	1.37	0.09
37°C	4.05	0.13	4.53	0.07	1.74	0.17
42°C	5.13	0.24	4.73	0.27	1.88	0.13
47°C	9.21	0.21	5.1	0.23	2.03	0.16

Table 3.1. Permittivity (a) and conductivity (b) of cytoplasm, plasma membranes of Hepa 1-6 cells, and the growth medium at 25°C, 37°C, 42°C and 47°C [48].

The conductivities and permittivities of the cytoplasm and cell membrane will vary between different cell lines [49, 50]. For example, in reference [49], the membrane permittivity ranged between 7 and 13 for six different lines of B cells, and the membrane conductivity ranged between  $14 \mu\text{S/m}$  and  $27 \mu\text{S/m}$  for three different lines of T cells. The measured electrical values of both the cytoplasm and membrane at room temperature are within reasonable range of those within the literature [6, 49, 50-53]. The temperature dependence of the electrical properties of a cell has not been extensively explored. In fact, the only publications in which the temperature dependence is considered (to my knowledge) rely on theoretical considerations rather than experimental results [50, 54]. Sudsiri et al. assumed a linear relationship between the temperature of the cell and the permittivity and conductivity of the cell cytoplasm, as well as the conductivity of the membrane [50]. The permittivity of the membrane, however, is assumed to remain constant which is inconsistent with the measurements reported in Table 3.1. According to the measurements, a linear relation is plausible for values at and below  $42^\circ\text{C}$ , but such assumptions cannot be made for higher temperatures.

Sudsiri et al assume that the permittivity of the cytoplasm decreases with increasing temperature [50], while the measurements in Table 3.1 show just the opposite. This discrepancy between assumptions and experimental results is also prevalent in reference [54] in which the temperature dependence of the permittivity is based on the Curie Law:  $\Delta\epsilon = C/T$ , where the permittivity of the cytoplasm also decreases with temperature. These assumptions are generally based on the thermoelectric properties of polar liquids [54, 56]. The cytoplasm is a complex system of biological material which reacts with a change in temperature to keep the cell functioning normally. Considering such a system just as a polar liquid is an oversimplification. That may explain why the permittivity of the cytoplasm does not behave the same as the medium for which the cells are grown in, in which the permittivity does decrease with an increase in temperature. A study of the reason for the observed increase in permittivity of cell membranes and cytoplasm is beyond the scope of this dissertation.

### III.II IMPEDANCE AND RELAXATION TIME RELATIONSHIP

A simplified circuit model of a biological cell, which takes only the cell membrane of a homogeneous cytoplasm into account, can be used to determine the electrical characteristics of a cell due to an applied subnanosecond pulse with different temperatures.

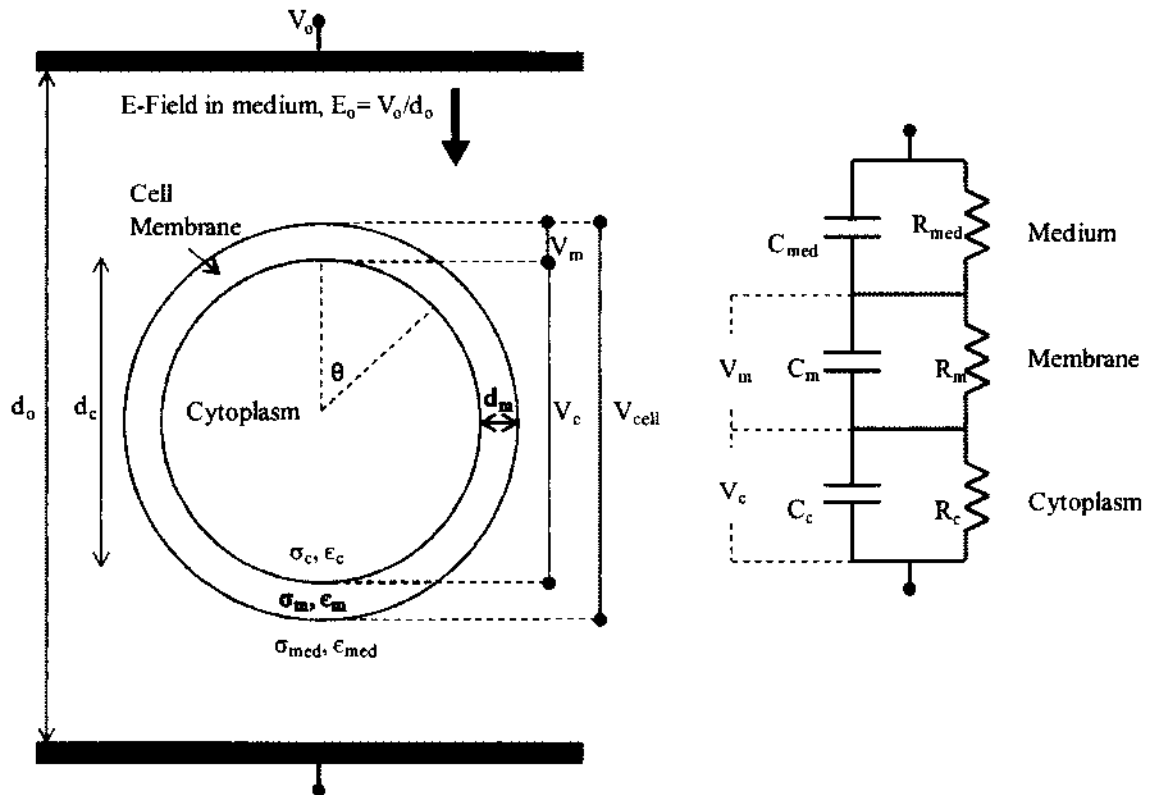


Fig. 3.1. Single shell cell model with the circuit diagram.

The diameter of the cell and the thickness of the membrane are approximately  $10 \mu\text{m}$ , and  $7 \text{ nm}$ , respectively. The volume of the cell, assuming a spherical shape, is approximately  $524 \mu\text{m}^3$ . For a cell concentration of  $6 \cdot 10^6 \text{ cells/mL}$ , the percentage of the total volume of the cells in the medium is only 0.314%. For a uniform distribution of the cells within the medium, the distance between each cell is approximately  $55 \mu\text{m}$ . This distance can be used to approximate the capacitance of the medium between the cells.

The impedance of the medium, membrane and the cytoplasm can be described as resistive or capacitive, depending on their relaxation time. The impedance of each layer is equal to its resistive component,  $R$ , in parallel with its capacitive component,  $C$ :

$$Z = \frac{R}{1 + j\omega RC} = \frac{R}{(\omega RC)^2 + 1} + j \frac{\omega R^2 C}{(\omega RC)^2 + 1} \quad 3.1$$

The absolute value of the impedance is equal to:

$$|Z| = \frac{R}{\sqrt{(\omega RC)^2 + 1}} \quad 3.2$$

If  $(\omega \cdot R \cdot C)^2 \gg 1$ , then the impedance of the layer is capacitive, whereas the impedance is resistive for  $(\omega \cdot R \cdot C)^2 \ll 1$ . The relaxation time ( $\tau_r$ ) is equal to  $R \cdot C$  and can be expressed in terms of the conductivity and permittivity of each respected layer through the following derivation.

$$(\omega \cdot R \cdot C)^2 + 1 = \left[ \omega \cdot \left( \frac{L}{\sigma \cdot A} \right) \cdot \left( \frac{\epsilon_o \cdot \epsilon \cdot A}{L} \right) \right]^2 + 1 = \left[ \omega \cdot \left( \frac{\epsilon_o \cdot \epsilon}{\sigma} \right) \right]^2 + 1 = \omega^2 \cdot \tau_r^2 + 1 \quad 3.3$$

In (3.3),  $L$  and  $A$  are the length and area of the portion of the cell of interest, respectively. However, the dimensions cancel out, leaving the relaxation time to be defined in terms of the conductivity and permittivity only. If the pulse width is much greater than the relaxation time, the impedance is resistive while it is capacitive of the pulse width is less than the relaxation time.

$$t \ll \tau_r \rightarrow \text{Capacitive} \quad t \gg \tau_r \rightarrow \text{Resistive}$$

The relaxation time of the membrane is on the order of a microsecond, and on the order of a nanosecond for the cytoplasm. The membrane charging model (Fig. 3.2) can be used for nanosecond pulses, but for pulses in the subnanosecond range, the dielectric model should be used. From the values in Table 3.1, the relaxation time of the cytoplasm increases from 1.8 ns to 2.5 ns with a temperature increase from 25°C to 47°C. For a pulse width of 200 ps (and less), the

electric fields in the various parts of the cell are then defined by their permittivity, rather than their conductivity. The electric field then acts directly on membrane proteins, rather than causing charging of the membrane, and, if sufficiently strong, can cause direct and instant conformational changes, such as voltage gating. Not only do these changes occur on the plasma membrane, but on intracellular membranes as well. Therefore, it is likely that these subnanosecond pulses will affect the plasma membrane in ways that nanosecond pulses are unable to do.

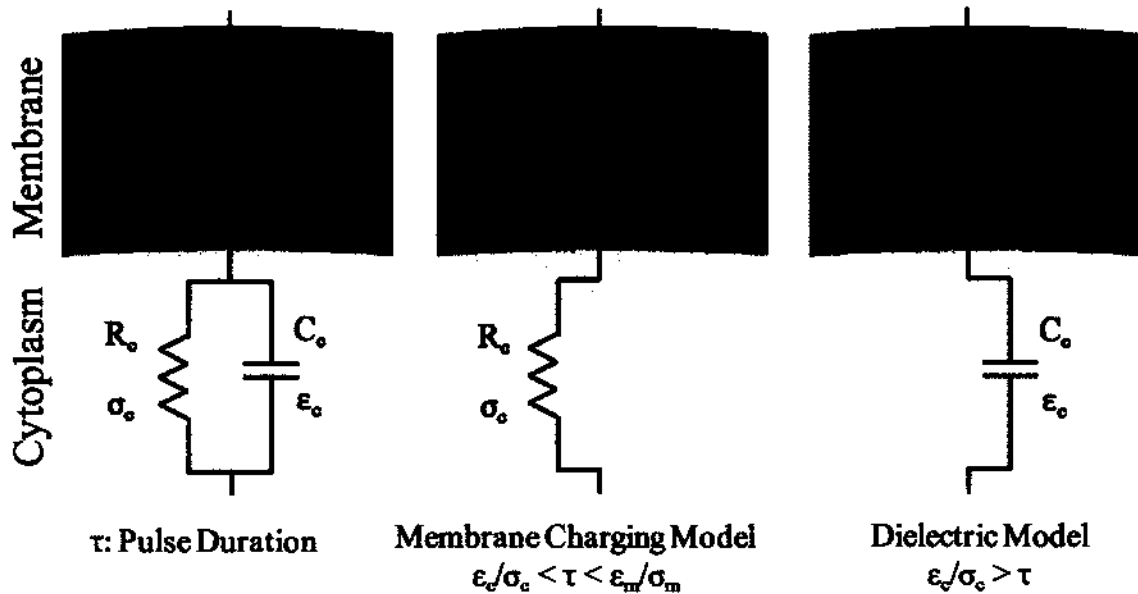


Fig. 3.2. Cell exposed to pulse durations greater than the relaxation time of the cytoplasm, and less than the relaxation time of the membrane can be expressed by the membrane charging model. Cells exposed to pulses less than the relaxation time of the cytoplasm can be expressed by the dielectric model in which the permittivity plays a higher role than the conductivity [47].

### III.III VOLTAGE INDUCED ACROSS THE MEMBRANE

The voltage across the membrane,  $V_m$ , in relationship to the applied voltage across the sample,  $V_o$ , is calculated as follows:

$$\frac{V_m}{V_o} = \frac{Z_m}{Z_m + Z_c + Z_{med}} \quad 3.4$$

The impedance of the medium, membrane and cytoplasm are represented by  $Z_{med}$ ,  $Z_m$ , and  $Z_c$ , respectively (Fig. 3.1). As stated above, the impedance of each portion can be determined by their respected relaxation time constants. From Table 3.1, the relaxation time for the membrane decreases from 5  $\mu$ s to 1.7  $\mu$ s for a temperature increase from 25°C to 47°C. Since the relaxation time for the temperature range is orders of magnitude larger than the pulse width (200 ps) the resistive component of the membrane can be neglected. The relaxation time of the cytoplasm increases from 1.8 ns to 2.5 ns for a temperature increase from 25°C to 47°C. Since the relaxation time is an order of magnitude larger than the pulse width, the resistive component of the cytoplasm can also be neglected. For the medium, the relaxation time decreases from 500 ps to 280 ps with an increase in temperature from 25°C to 47°C. The relaxation time of the medium is on the same order as the pulse. In this case, both resistive and capacitive components of the medium must be accounted for. Equation 3.4, with some algebraic manipulation, can now be expressed as

$$\frac{V_m}{V_o} = \frac{s \cdot R_{med} \cdot C_{med} + 1}{s \cdot R_{med} \cdot (C_{med} + C_m) + 1 + \frac{C_m}{C_c} + s \cdot R_{med} \cdot \frac{C_{med} \cdot C_m}{C_c}} \quad 3.5$$

The capacitance per unit area for the membrane and medium are approximately 2  $\mu$ F $\cdot$ cm<sup>-2</sup> and 1 nF $\cdot$ cm<sup>-2</sup>, respectively (using the permittivity values for room temperature in Table 3.1 and a thickness of 7 nm for the membrane, and 55  $\mu$ m for the medium). Therefore, the medium capacitance ( $C_{med}$ ) can be neglected in the first term of the denominator. The cytoplasm capacitance per unit area is approximately 25 nF $\cdot$ cm<sup>-2</sup>. Therefore, the 1 in the denominator can be neglected since  $C_m/C_c \gg 1$ . Equation 3.5 reduces to

$$\frac{V_m}{V_o} = \frac{s \cdot R_{med} \cdot C_{med} + 1}{s \cdot R_{med} \cdot C_m \cdot \left(1 + \frac{C_{med}}{C_c}\right) + \frac{C_m}{C_c}} \quad 3.6$$



The ratio of the medium capacitance to the cytoplasm capacitance ( $C_{med}/C_c$ ) is much less than 1, in which case, (3.6) can be reduced further:

$$\frac{V_m}{V_o} = \frac{s \cdot R_{med} \cdot C_{med} + 1}{s \cdot R_{med} \cdot C_m + \frac{C_m}{C_c}} \quad 3.7$$

The 200 ps (FWHM) pulses can be approximated by a triangular pulse, with a rise and fall time of 200 ps. In order to determine the voltage across the membrane at the peak of the pulse at 200 ps, only the rising portion of the pulse needs to be considered. The rise time of the triangular pulse can be expressed as a ramp function,  $V_o(t) = V_p \cdot t/\tau$ , in which  $\tau$  is the risetime of the pulse (200 ps) and  $V_p$  is the amplitude of the pulse. After performing an Inverse Laplace Transform and expressing the resistive and capacitive terms in terms of their conductivities, permittivities and characteristic dimensions, respectively, we obtain an expression for the temporal development of the voltage across the membrane:

$$V_m(t) = 2 \cdot \frac{d_m}{d_c} \cdot \frac{\epsilon_c}{\epsilon_m} \cdot V_o(t) + \frac{2 \cdot V_p \cdot \epsilon_o \cdot \epsilon_c \cdot d_m}{\tau \cdot \sigma_{med} \cdot \epsilon_m \cdot d_c} \cdot \left( 2 \cdot \epsilon_c \cdot \frac{d_o}{d_c} - \epsilon_{med} \right) \cdot \left( e^{-t \cdot \frac{\sigma_{med} \cdot d_c}{2 \cdot \epsilon_o \cdot \epsilon_c \cdot d_o}} - 1 \right) \quad 3.8$$

By setting  $t = \tau$ ,  $V_o(\tau)/d_o = V_p/d_o = E_o$ , and expanding the exponential function by Taylor's series to the second order (the value in the exponent is very small compared to one), (3.8) becomes:

$$V_m(\tau) = \frac{E_o \cdot d_m}{2 \cdot \epsilon_o \cdot \epsilon_m \cdot \epsilon_c \cdot d_o} \cdot \left( \tau \cdot d_o \cdot \epsilon_c \cdot \sigma_{med} + 2 \cdot \epsilon_o \cdot \epsilon_c \cdot \epsilon_{med} \cdot d_o - \tau \cdot \frac{d_c}{2} \cdot \sigma_{med} \cdot \epsilon_{med} \right) \quad 3.9$$

By neglecting the last term in the bracket, which is very small compared to the first two terms, the peak membrane voltage is given as:

$$V_m(\tau) = E_o \cdot \frac{d_m}{2 \cdot \epsilon_o \cdot \epsilon_m} \cdot (\tau \cdot \sigma_{med} + 2 \cdot \epsilon_o \cdot \epsilon_{med}) \quad 3.10$$

Equation 3.10 is in 99.99% agreement with the voltage across the membrane in which the full analytical solution was determined using Mathcad [57]. The membrane and medium, at 25°C, have a relative dielectric constant of 13.9 and 79, respectively. The electric field in the membrane is 5.6 times higher than the electric field in the adjacent cytoplasm at 25°C whereas this ratio is decreased to 3.5 for a temperature of 47°C. The conductivity of the medium increases from 1.37 S/m to 2.03 S/m with a temperature increase from 25°C to 47°C. For an applied electric field of 83 kV/cm, the voltage across the membrane, with a thickness of 7 nm, is 396 mV at a temperature of 25°C and decreases to 281 mV for 47°C. The induced membrane voltage, due to a constant applied electric field, decreases with an increase in temperature. This voltage will be superimposed to the resting potential of the membrane.

### III.IV TEMPERATURE EFFECT ON RESTING POTENTIAL

The temperature has a direct effect on the membrane potential [11 - 13]. The magnitude of the resting potential increases with an increase in temperature, most likely due to the change in the passive permeability ratio of the ions [12, 13]. It has been shown that the effects on the resting potential due to a change in temperature are immediate in muscle fibers and can drop 15 mV with a 10°C decrease in the temperature [12]. The voltage of the membrane with relation to the temperature can be expressed with the Nertz equation [5, 12, 13]:

$$V_m = \frac{R \cdot T}{F} \ln \left[ \frac{(P_K + P_{Na})_{intracellular}}{(P_K + P_{Na})_{extracellular}} \right] \quad 3.11$$

Where R, T, and F are the gas constant, temperature, and faraday constant. The permeability constant of potassium and sodium are denoted  $P_K$  and  $P_{Na}$ , respectively. A linear trend exists between the temperature and the resting potential of the membrane. An increase in temperature will cause an increase in the resting potential, which is superimposed on the voltage across the membrane induced by an external electric field (Fig. 3.3(a)). Therefore, less electric field

strength is needed to reach the threshold voltage at a higher temperature. For cells exposed to external electric fields in which the imposed voltage across the membrane is much greater than the resting potential, the effects of the resting potential becomes negligible [58]. This effect may only be applicable to membranes exposed to pulses with rise times/durations less than the charging time of the membrane. For cells exposed to short durations, the external electric field will be superimposed to the electric field across the membrane caused by the resting potential. Gehl has shown that the area of poration is greater on the side of the cell facing the anode while the degree of poration is greater on the cathode side [14]. However, if the risetime and/or pulse duration is long compared to the charging time, ions will line up across the membrane as depicted in Fig. 3.3(b) in which case, the effects of the membrane potential would be negligible.

The external field will be superimposed on the natural potential across the membrane which will cause depolarization on the cathode side and hyperpolarization on the side of the cell facing the anode (for  $\tau_p < \tau_r$ ) [8, 58]. As a result of the increased electric field on the side of the cell facing the anode, cells will be permeabilized on the anode side first, as depicted in Fig. 3.3(a).

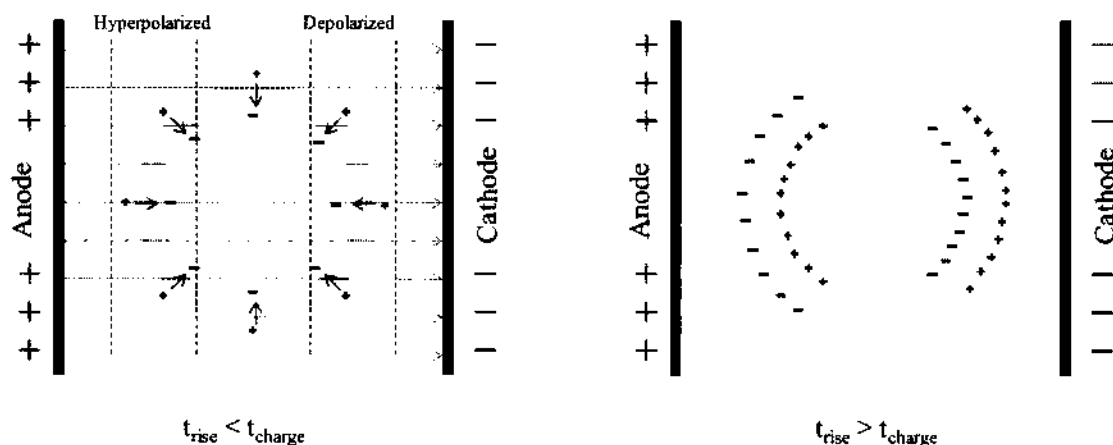


Fig. 3.3. The external electric field will be superimposed on the electric field across the membrane due to the resting potential. As a result, the field across the membrane facing the anode will be higher than the side facing the cathode. Therefore, electroporation begins on the anode side of the cell for cells exposed to pulsed electric fields with rise times less than the charging time of the membrane. For slow rise times, the cell membrane will be charged such that the resting potential can be neglected.

## **CHAPTER IV**

### **TEMPERATURE EFFECTS ON PLASMA MEMBRANE**

The temperature not only has an effect on the electrical properties of the cell (as discussed in Chapter III), but also on the mechanical properties of the cell, mainly the fluidity of the cell membrane. When the cell is exposed to an external electric field, the fluidity determines the ease at which electroporation or permeabilization can occur [42, 15-18]. A less viscous membrane will require a reduced voltage across the membrane to induce pore formation or electroporomeabilization. This chapter is divided into four sections; The first section contains the basic structure of the plasma membrane, and its method to maintain viscosity with a temperature change, which is known as homeoviscious adaptation. The second section is an overview of experiments studying homeoviscious adaptation, and in the third section, the effect of temperature during electroporation is discussed. The last section discusses the effect of temperature on the resting potential of the membrane.

#### **IV.I STRUCTURE OF THE PLASMA MEMBRANE**

The plasma membrane for almost every living cell has the same basic structure and can be described by the fluid mosaic model [59-62]. The membrane is a fluid like structure composed mostly of lipids, and proteins in which most of membrane's interactions among its components are noncovalent, leaving individual lipid and protein molecules to move about freely in the lateral plane of the membrane. This model is not only suited for the plasma membrane, but for intracellular membranes as well [59]. A majority of the lipids are phospholipids, which are lipids containing a hydrophilic polar head connected to two hydrophobic fatty acid chains. The chains of the phospholipids, also referred to as leaflets, are either saturated or unsaturated. Saturated fatty acids provide relatively straight chains while unsaturated fatty acids have kinks in the acid chain. The straight line of saturated chain allows for tight packing into a paracrystalline

array while the kink in the unsaturated chain hinders the formation of a crystalline state. Another major group of lipids in the plasma membrane are the sterol lipids, also known as cholesterol. The tail of the sterol is a rigid rod shape consisting of four fused rings composed of carbon which prevents the tight packing of the acid chains, thus keeping the membrane from crystallizing at low temperatures. At higher temperatures, the rigid composition of the sterol makes it difficult for neighboring fatty acid chains to rotate around the sterol, which keeps the viscosity of the membrane from increasing to the point in which it can no longer maintain its structure.

The fluidity of the membrane depends on the lipid composition and the temperature. Below a certain temperature (transition temperature), there is very little lipid motion and the membrane exists as a crystalline array. Above the transition temperature, the membrane acts as a fluid, in that the lipids undergo rapid motion. The transition temperature of bacteria and mammalian cells is approximately 10°C below the ambient growth temperature, 37°C [43, 63-65]. If the temperature is well above the growth temperature for a certain period of time, the membrane may increase fluidity beyond a certain point which causes cell blebbing, which can lead to cell death [66, 67].

The cell membrane uses several mechanisms to maintain its fluidity over a wide range of temperature (around ambient body temperature). The first mechanism involves changing the ratio of the saturated and unsaturated fatty acid chains. The transition temperature of the membrane decreases as the ratio of unsaturated to saturated acid chains increases. Several references which focus on the ratio of unsaturated to saturated acids in the membrane versus temperature show that cells will produce more saturated acids than unsaturated in order to maintain fluidity [18, 19, 68, 69]. The second mechanism that helps maintain the fluidity of the membrane is the sterol content within the membrane. The concentration of sterols also helps maintain fluidity in a wide range of temperatures around the physiological temperature in that a higher concentration will decrease the fluidity of the membrane, while a lower concentration

increases the fluidity [70]. The process of maintaining fluidity over a certain temperature range is known as homeoviscous adaptation.

#### **IV.II HEAT SHOCK VERSUS HOMEOVISCIOUS ADAPTATION**

Heat shock is defined as a short period of exposure in which the cell is above its physiological temperature, and the cell responds with heat shock genes. Heat adaptation is when the cell is exposed to elevated temperature for a long period of time, such that the cell adapts to the higher temperature, which involves alterations in the cell membrane to maintain fluidity [18, 19, 69, 71]. This adaptation is known as homeoviscous adaptation and mainly involves adjusting the ratio of saturated to unsaturated fatty acid chains.

There are two main methods in determining the degree of viscosity with respect to temperature: electron spin resonance (ESP) and permeabilization. In ESP, a lipophilic spin probe, which is a molecule containing one or more unpaired electrons, dissolves into the plasma membrane. Cell pellets containing the spin probes are exposed to magnetic fields on the order of 0.1 T followed by exposure to microwave radiation in the range of 9 GHz to 10 GHz [72]. Changes in the viscosity of the membrane will result in changes in the EPR line width and shape [64, 72, 73]. A spin probe in a low viscosity membrane is said to have higher activity than if in a membrane of higher viscosity [64]. Typically, the EPR line shape, which contains all the information in regards to the probes environment are computationally analyzed in order to determine the fluidity of the membrane [72, 73]. A more detailed description of the ESP method can be given in [64, 73]. For the permeabilization method, the cells are exposed to dyes, in which the cells are normally impermeant to (fluorescent or bleomycin uptake). Electric field pulses on the order of 100  $\mu$ s with fields between 400 V/cm and 900 V/cm are applied to effectively cause electroporation [15].

Sinensky used EPR to show the change in membrane fluidity for *E. coli* for different growth temperatures [64]. There was a negligible change in the activity of the spin probe for

bacteria grown at temperatures ranging from 15°C to 43°C, in which it was concluded the fluidity of the membranes were equal. However, the activity of the spin probe was immediately reduced when bacteria grown at 43°C were exposed to a temperature of 15°C, which meant there was an immediate decrease in the membrane fluidity. An increase in the spin probe activity was observed when Sinensky exposed bacteria, grown at 23°C, to a temperature of 37°C. He concluded that bacteria cultured for 24 hours at their respected growth temperatures experienced homeoviscous adaptation by varying the fatty-acid composition of the phospholipids [64].

Yuk and Marshall compared the ratio of lipid concentration for heat shock with that for heat adaptation for bacteria exposed to temperatures of 42°C and 45°C, and were compared to bacteria which remained at 37°C [18]. Cells exposed to the elevated temperatures for 15 minutes were described as heat shocked, while those exposed to the elevated temperatures for 18 hours were considered heat adapted. The cells exposed to the temperatures for 18 hours showed a much higher change in lipid concentration than those exposed to the same temperatures for 15 minutes, which showed the cells had adapted to the higher temperatures by increasing the lipid concentration in the membrane.

Kanduser et al., conducted membrane fluidity and permeabilization experiments on two different cell lines (V-79 and B16F-1) at 4°C and 37°C by EPR method and electroporabilization [15, 72]. Cells were exposed to a waterbath at 37°C or to ice water at 4°C for 5 minutes before measurements. The EPR experiments for both cell lines showed a decrease in activity of the spin probe at a lower temperature, suggesting a decrease in the membrane fluidity. However, the effects for the V-79 cell line greatly outweighed the effects of the B16F-1 cell line suggesting the B16 cell line was able to maintain its fluidity more effectively than the V-79 cell line. As concluded, cells can change the composition of their membranes to maintain fluidity, but this process must occur over time (> 18 hours). The experiments discussed in this dissertation would be classified as heat shock experiments. Therefore, it is possible the

cells will not have enough time to adjust their membrane viscosity with the increase in temperature. As a result, the fluidity of the membrane will most likely increase with an increase in temperature, making the cells more susceptible to the pulsed electric fields.

The electropermeabilization method, in reference [15] gave a similar conclusion as the EPR method. At 900 V/cm (100  $\mu$ s, 1 Hz) 80% of both cell lines were permeabilized (determined by bleomycin uptake) at 37°C. At 4°C, 40% of the B16 cells were permeabilized, while only 20% of the V79 cells were. This data also suggested the B16 cells are more adaptive to the change in temperature [15, 72]. This method shows the importance of the effect of temperature on electropermeabilization. A higher temperature increased the fluidity of the membrane which caused a higher degree of permeabilization of the cell. The increase in fluidity may have decreased the threshold energy needed for electropermeabilization, such that, for the same pulse conditions, a higher degree of permeabilization occurs for a higher temperature. This effect should hold true for pulses of shorter duration as well.

#### IV.III TEMPERATURE EFFECTS ON ELECTROPORATION

The energy needed for the reorientation of the lipid molecules forming the pore is lower if the fluidity of the membrane is higher [15, 42]. There are several models and simulations that show that an increase in temperature is favorable for pore formation on a cell membrane exposed to electric fields [7, 16, 17, 74]. In references [16, 17] a patch model type of analysis was used to derive the critical potential across a membrane to induce electroporation. Two models based on the law of conservation of energy and in terms of the impulse-momentum principle, were used to derive the minimum voltage needed for electroporation [16, 17].

$$\Delta V = \frac{-1}{q} \left( \frac{2mL^2}{\tau_o^2} + e^{\Delta E/RT} \Phi_w \right) \quad 4.1$$



In (4.1),  $q$ ,  $m$ , and  $L$  are the charge, mass and thickness of the patch of membrane, respectively. The electric field critical pulse width needed for electroporation is denoted by  $\tau_0$ . The temperature of sample is represented by  $T$ , and  $\Delta E$  is the thermodynamic energy of the molecules in the membrane of the cell. The amount of energy needed to overcome the dragging force,  $f(x)$ , is defined as [16, 17]:

$$\Phi_w = \int_0^L f(x) dx \quad 4.2$$

The dragging force, which is dependent on temperature, is the combination of the dipole-dipole electric attraction force of the lipids and other frictional forces, and is proportional to the viscosity of the membrane. A decrease in the energy is needed for the patch to overcome the dragging force if the viscosity is decreased, which is associated with an increase in temperature. The exponential function can be expressed as a Boltzmann factor, which gives the required portion of molecules with enough energy needed to break away from the dragging energy bond [16]. The correlation of their equation and experimental data was equal to 0.93 for pulses with pulse widths on the order of microseconds.

This observation is evident in the simulation of a lipid layer to an electric field at two different temperatures [7]. Song et al. simulated the effects of a three degree change in temperature on a biological membrane exposed to an external electric field in order to investigate the possibility of local temperature effects on the membrane caused by the pulsed electric fields. In this simulation, a constant electric field was applied to a membrane containing dipalmitoyl-phosphatidyl-choline (DPPC) lipids with an electric field equal to 0.5 V/nm across the membrane. At a time of 1 ns, no pore formation occurred at 40°C. However, at 43°C, pore formation was observed at 1 ns which consisted of water nanowires connecting the extra and intra-cellular regions through the membrane.

## **CHAPTER V**

### **SUBNANOSECOND PULSE GENERATORS**

High voltage subnanosecond pulse generators date back to the 1980's [75], and pulses with subnanosecond risetimes, and amplitudes in the 100's kV date back to 1965 [76]. Typically, amplitudes ranging into the 100's kilovolt range are created by transmission line with spark gaps [40, 76, 77], while those using semiconductor switches typically range in the low kV to V range [78, 79]. Recently, semiconductor switches (SOS, photoconductive, transistors, etc.) have been used to create voltages in the 100's of kV range with subnanosecond rise times [80-83]. The main advantages of semiconductor switches are the higher repetition rate (kHz – MHz), increased lifetime and lower jitter (< ns). The main advantages of spark gap switches are the simple design and wide range of transferable energy ( $\mu\text{J}$  – MJ). In the following four sections, subnanosecond pulse generators using avalanche transistors, SOS diodes, photoconductive switches, and spark gap switches will be discussed.

#### **V.I SUB NS PULSE GENERATORS WITH AVALANCHE TRANSISTORS AS SWITCHES**

A common method of creating high voltage pulses with fast risetimes (on the order of 1 ns) is to use a string of avalanche transistors, as depicted in Fig. 1 [75, 78].

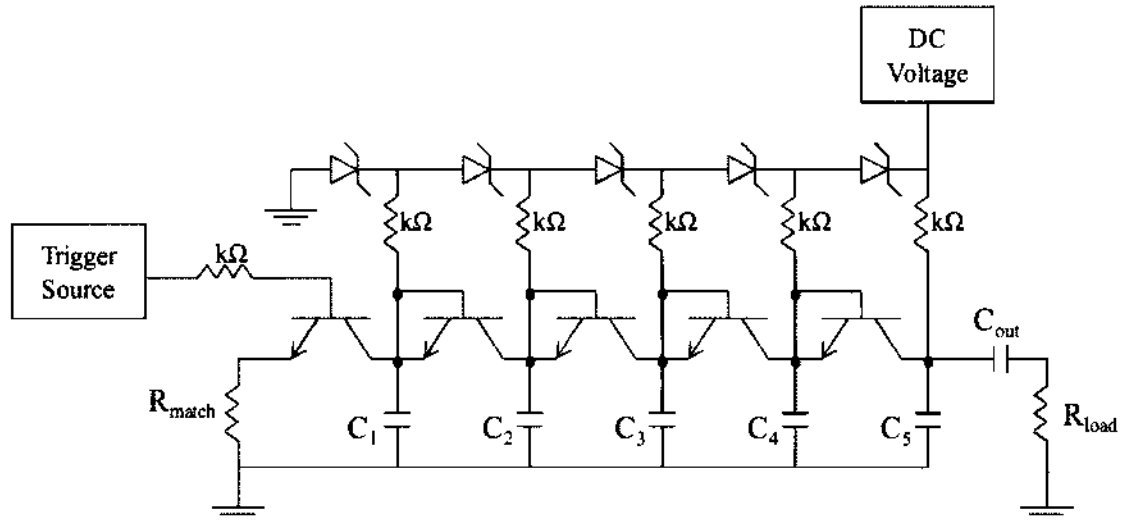


Fig. 5.1. Schematic of an avalanche transistor subnanosecond pulse generator. Each transistor has an inductance associated with it, which gives the circuit a transmission line type of setup. By decreasing the capacitance of each stage ( $C_1 < C_2 < C_3 < C_4 < C_5$ ), the impedance of each stage is increased, which sharpens the risetime of the pulse. The fall time of the pulse depends on the RC time constant of the load and  $C_{out}$ .

Avalanche transistors with nonlinear, high gain characteristics are currently able to switch in the 100 ps regime, which makes them ideal for creating subnanosecond pulses [78]. By placing the chain of transistors in a tapered transmission line configuration, the rise of the pulse sharpens progressively from stage to stage [78]. Each transistor has an associated inductance with it, which gives an impedance of each stage equal to  $(L_{trans}/C_N)^{0.5}$  in which N represents the stage number. The tapering of the impedance of the transmission line from low to high causes the avalanche process of each stage to occur faster than the preceding stage. The reason is as follows.

Because the transistors are in series, the current through each stage is approximately the same. Therefore, each stage is designed to have a higher impedance than the previous stage, which increases the voltage across that stage ( $V = I \cdot R$  where I is constant). A higher over voltage will create a faster avalanche process, effectively sharpening the risetime of the pulse. The change in impedance from stage to stage causes reflections between each stage. These reflections are reduced by placing a resistor of equal impedance to the first load between the emitter of the

first transistor and ground ( $R_{\text{match}}$  in Fig. 5.1), which absorbs the reflected signals. The final stage should have an impedance equal to the load impedance. As a result, reflections are absorbed from both sides of the transmission line. Krishnaswamy et al. were able to create a pulse with a 800 ps rise time, 1.3 ns pulse width with an amplitude up to 1.1 kV into a  $50\ \Omega$  load with a repetition rate of 200 kHz [78]. This pulse generator was used to study the effects of the pulses on cells between electrodes under a microscope.

## V.II SUB NS PULSE GENERATORS WITH SOS SWITCHES

The silicon or semiconductor opening switch (SOS), introduced in 1992 by Kotov et al. [84], is comprised of a diode, or chain of diodes, capable of interrupting current densities up to  $10\ \text{kA/cm}^2$  in time frames less than 10 ns [85]. This specific type of diode has a  $p^-p-n-n^+$  structure and is based on two different modes of operation: The junction recovery (JR) and the silicon opening switch (SOS) mode. The JR mode occurs in any rectifying diode during polarity inversion, and is the process by which the diode stops conducting due to the recovery of the PN junction. This mode is used for decreasing the turn off time and is capable of dissipating less energy during the switching process as opposed to the SOS mode [86].

In the SOS mode, the junction does not recover, but the switching is caused by a dramatic increase in the resistance of the low doped part of the p-layer [86]. The SOS mode is capable of switching higher energies than the JR mode. The main purpose of the diode is to function as an opening switch that commutes the current from an inductor to a resistive load [86]. The diode alone is not an opening switch. It must be activated by a forward current because it can only interrupt current (open) during the reverse bias operation. Therefore, the diode is coupled with an oscillatory circuit in order to cause the diode to behave as an opening switch [85, 86]. The basic setup of an SOS type pulse generator is shown in Fig. 5.2.

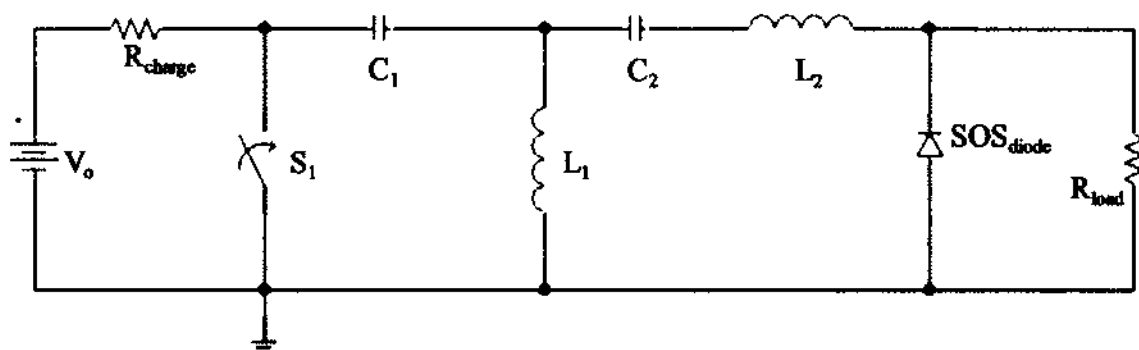


Fig. 5.2. Simple schematic layout of a pulse generator incorporating a single SOS switch, represented by the SOS diode. Typically,  $C_1$  will equal  $C_2$  and  $L_1$  will equal  $L_2$ .

With  $S_1$  open,  $C_1$  is charged up to  $V_o$  while  $C_2$  prevents any DC currents flowing to the load. When  $S_1$  closes,  $C_1$  discharges and the SOS diode acts as a short, causing the circuit creates an oscillating effect, as shown in Fig 5.3 (dashed black trace). When the current reverses polarity across the diode, a charge is still left over in the depletion region, and the diode is able to conduct in the reverse bias mode. However, once the charge is depleted, the resistance of the diode quickly increases (essentially opens), and the current is redirected into the load. This is designed to occur when most of the energy has been transferred from  $C_1$  to  $L_2$ . The voltage across the load is then equal to the current across the load (solid black trace) multiplied by the load resistance. The risetime of the pulse depends on the speed of the opening switch while the fall time depends on the time constant of  $L_2$  and  $R_{load}$ .

Two main aspects are to be considered when designing such a system. The first is that the diode needs to break down when the reverse current across the diode is at its peak, as shown in Fig. 5.3. This is achieved by matching the time difference between the negative and positive peak of the oscillating signal across the diode at a value twice as much as the reverse recovery time of the diode.

The second aspect is to insure that the majority of the energy stored in  $C_1$  as been transferred into  $L_2$ . This is to avoid having resonating signals across the load. In Fig. 5.3, the reverse current should be at maximum by the time the diode opens. The peak of the reverse

current should be twice the peak of the forward current, which is achieved by choosing optimal values of  $L$  and  $C$ . Such relations have been conducted in reference [86] and their values have been taken and simulated in PSpice, and the results are shown in Fig. 5.3. Both capacitors and inductors have values equal to 33 nF and 70 nH, respectively. The load resistance is 50  $\Omega$ , and the input voltage is 100 V. The output voltage across the load is equal to 2.25 kV (45 A x 50  $\Omega$ ).

The switches used in this circuit ( $S_1$ ) are typically solid state switches with voltage and current ratings in the 100's – 1000 V range, and 10's A range, respectively. These switches are primarily used for pulse amplitudes in the low kV range [86, 87]. In order to achieve voltages in the high kV range, typically magnetic switches are used [80, 85, 88].

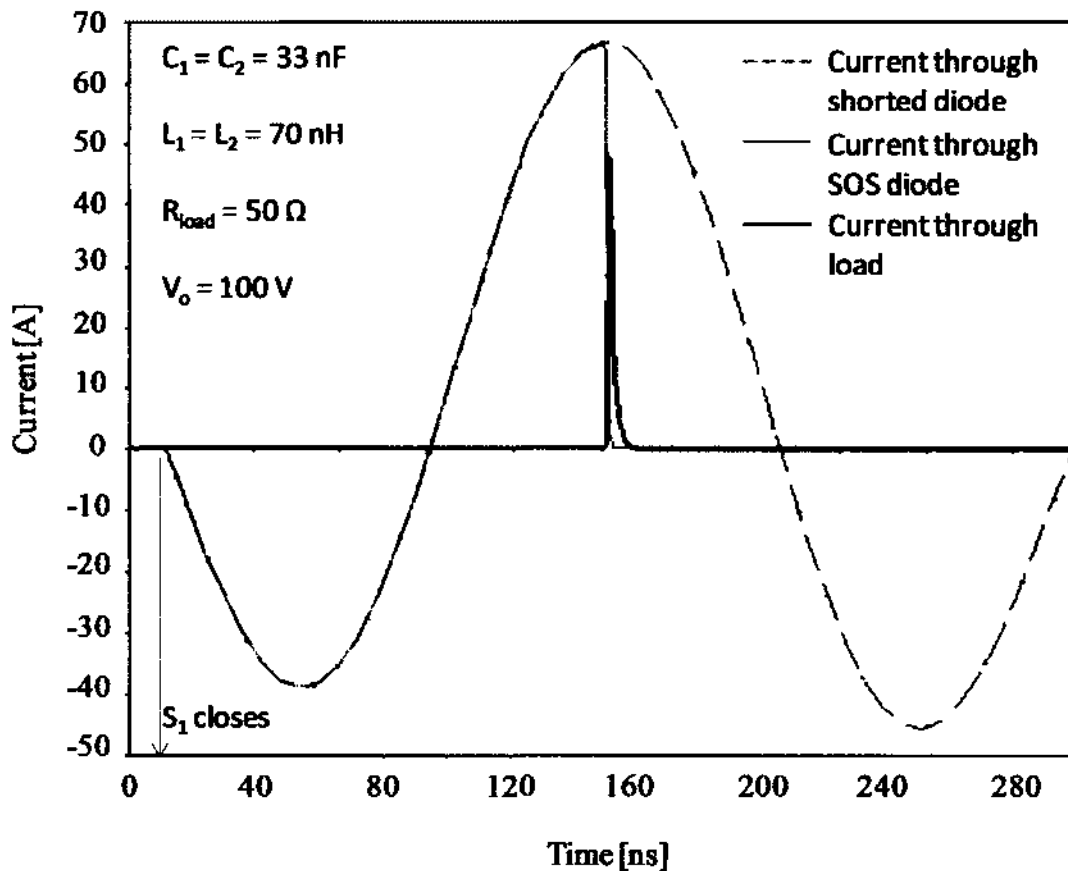


Fig. 5.3. The current through a shorted diode, when  $S_1$  closes, shows the oscillation of the circuit. In order for the SOS switch to open, the time between the negative and positive peak of the current across the diode needs to be twice that of the reverse recovery time of the diode. The voltage across the load is equal to the current across the load (solid black) multiplied by the resistance.

The major advantage of SOS switches is the lifetime of the switch ( $10^{11}$  pulses) and repetition rate (kHz) [85]. By stacking SOS switches, they are capable of holding off voltages in the 100's kV range, and even into the MV range [81].

SOS type pulse generators can be incorporated into a variety of ways either by simply stacking them or combining them with other pulse compression circuits to achieve a desired pulse across a given load. Engelko and Bluhm proposed a circuit consisting of three SOS switches to charge up inductors in series and discharging them in parallel which allows for a threefold increase in the current across a given load [85]. With magnetic switching, they were able to model a 235 kV pulse with a pulse width of 5 ns, and a risetime less than 1 ns across a 100  $\Omega$  load. Teramoto et al. were able to create a 20 ns pulse with an amplitude of 50 kV across a 300  $\Omega$  load by using an SOS generator [88]. The pulse generator consisted of three stages: charging, pulse compression, and pulse sharpening. The charging stage consisted of a capacitor charging a saturable inductor, which when saturated, transferred the stored energy to the second stage. The second stage used magnetic pulse compression to decrease the duration of the pulse from the ms time frame to the  $\mu$ s time frame. The third and final stage comprised of the SOS switch in a layout similar to one shown in Fig. 5.1. Voltages as high as 150 kV with pulse durations equal to 60 ns were achievable with a 300  $\Omega$  load.

Sanders et al. used air coils for the inductance in their pulse generator design, similar to the one shown in Fig. 5.1 [86]. In this case, they were able to achieve a 5 kV pulse with a pulse width of 2.5 ns into a 50 ohm load with using a solid state switch (APT37M100L MOSFET) opposed to a magnetic switch. In order to handle the high current, five chains of five stacked diodes were used, as is done in many SOS generator systems [86]. Yalandin et al. combined an SOS pulse generator with a pulse compression stage comprised of two hydrogen spark gaps [82]. They were able to achieve a 200 kV pulse with a risetime of 180 ps, pulse width of 420 ps at a repetition rate of 3.5 kHz.

### V.III SUB NS PULSE GENERATORS WITH PHOTOCONDUCTIVE SWITCHES

Photoconductive switches are semiconductor devices (most commonly GaAs), commonly used in high power microwave generation [89] and wideband radar applications [90]. The photoconductive switch is triggered optically with a laser (mJ range) which has the characteristic of optical isolation. Due to the finite leakage current of the semiconductor material, the switch requires pulsed charging opposed to DC charging.

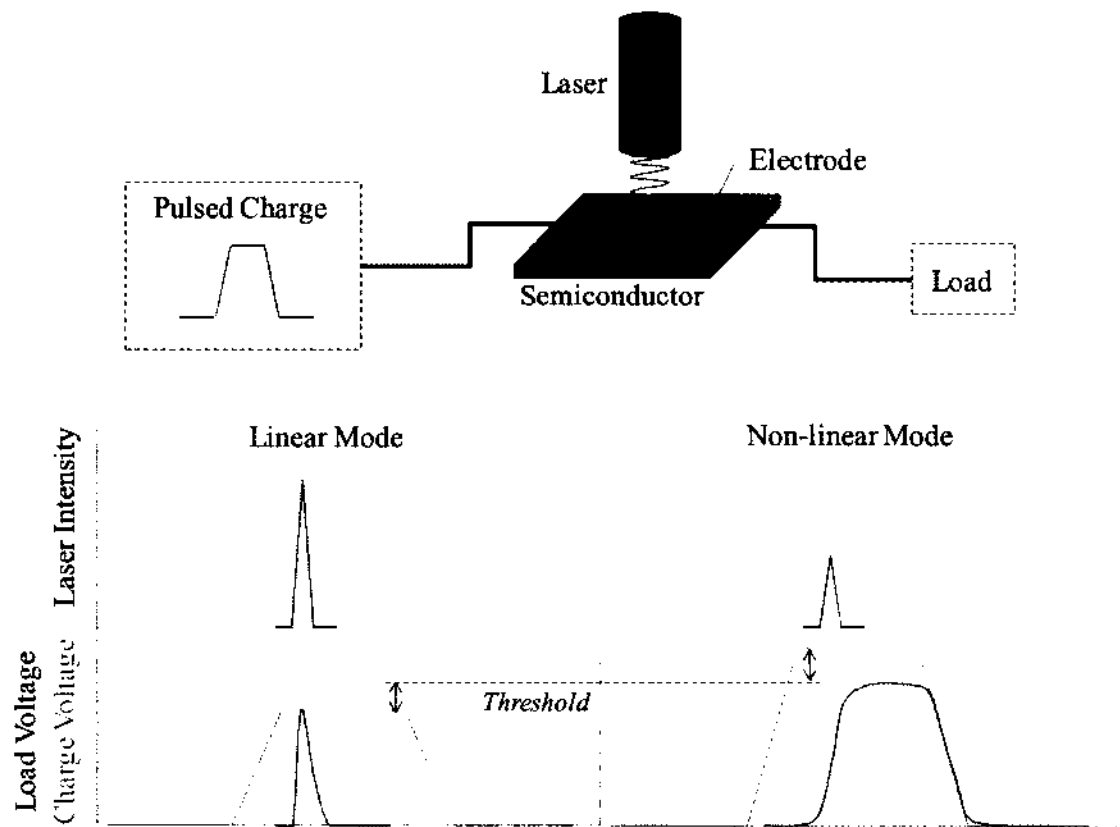


Fig. 5.4. Concept of a pulse generator incorporating a photoconductive switch. A pulsed power source is used to charge the electrodes. The mode depends on the magnitude of the electric field across the switch prior to triggering. In the linear mode, a high energy laser source is needed (mJ) to close the switch whereas the nonlinear mode requires less energy from the laser ( $\mu\text{J}$ ).



The concept of the photoconductive switch is shown in Fig. 5.4. When illuminated with a laser, the switch goes from a nonconductive state to a conductive state by photoionization and/or collisional ionization depending on the magnitude of the applied voltage across the switch [91]. There are two modes of operation for the GaAs: linear and nonlinear [91]. In the linear mode, the number of charge carriers is determined by the laser intensity, and the shape of the pulse across the load is largely determined by the shape of the laser pulse. In the nonlinear mode, the switch only partially recovers such that the field across the switch will decrease to a sustained field, which is known as the lock on field.

Due to the short generation time of GaAs ( $10^{-14}$  s), the closing time of GaAs switch in linear mode is theoretically limited by the risetime of the laser pulse [92]. Since relatively fast laser sources exist today (ps range), the risetime of the pulse generated with a photoconductive switch can be in the picosecond range. The opening time of the switch is limited by the recombination rate of the free carriers and the circuit parameters of the switch [83]. In the linear mode, the recombination rate is approximately the same as with no field applied. For GaAs, the recombination rate is on the order of 1 ns, whereas for Si, it is on the order of  $\mu$ s. Pocha et al. designed a switch, when charged to 12 kV and irradiated with a 1.32 mJ laser, created a 12 kV pulse with a risetime and fall time of 200 ps and 1.06 ns, respectively [83]. The disadvantage of the linear mode is the energy needed by the laser to induce the closing of the switch (without neutron irradiation) is on the order of mJ [90]. The closing time can be decreased by doping or by using neutron irradiation. Druce et al. were able to achieve a 3.5 kV pulse with a risetime and fall time of 176 ps and 306 ps, respectively, with a 227  $\mu$ J neutron irradiated source [92]. An electric field threshold in which the mode goes from linear to nonlinear exists. This threshold limits the power in which the photoconductive switch can be used as a fast opening and closing switch (10's kV/cm). Beyond this threshold, the switch behaves as just a closing switch.

As the electric field across the semiconductor is increased above this threshold, the number of charge carriers in the switch is increased by collisional ionization, in which the

increase is exponential, as with a gas switch [91]. This nonlinear mode is also referred to as the avalanche or lock on mode [83, 92]. In GaAs, the threshold is approximately 20 to 25 kV/cm [83]. For GaAs, the lock on field is between 3.5 kV/cm and 8.5 kV/cm, depending on the impurities in the material. For InP, the lock on field is approximately 14.4 kV/cm [90]. The energy needed from the laser to induce the nonlinear mode is in the  $\mu\text{J}$ , which is a distinct advantage over the linear mode [90]. However, the fall time of the voltage across the switch is longer since it depends on the voltage across the switch, unless using a high power laser. This mode is typically used for closing switches in high power microwave generation [92]. Pocha et al. demonstrated a switch in lock on mode charged to 30 kV, with a gap of 5 mm which produced a pulse with a risetime of 302 ps. The risetime is comparable to a switch operating in the linear mode since they used a high energy laser, 2.1 mJ [83]. Zutavern et al. experimentally determined the lock on field to be independent of the charging voltage [90]. A 1.5 cm long GaAs PCSS was triggered with a 150 W laser in which the charge voltage ranged from 6.1 kV to 11.3 kV.

The lock on mode occurs at fields lower than what is needed to induce avalanche breakdown, which is approximately 200 kV/cm in GaAs. The mechanism which leads to this mode is not well understood, but the most widely accepted theory is the combination of impact ionization of impurity or defect levels in the semiconductor, the Gunn effect, thermal runaway and double injection through the contacts [90, 93].

The most common material used is GaAs which has a bandgap energy of 1.43 eV. The maximum wavelength needed to create an electron hole pair in a perfect crystal of GaAs is 860 nm, which has an absorption depth of approximately 10  $\mu\text{m}$  at this wavelength [92]. Due to impurities, a large concentration of mid gaps appear which lead to extrinsic generation, which allow the wavelength of the light needed to create excitation to increase to values above 1  $\mu\text{m}$ . For wavelengths above 0.9  $\mu\text{m}$ , the absorption depth of GaAs increases to approximately 1000  $\mu\text{m}$ , effectively decreasing the resistance of the channel [83, 92]. The Nd:YAG laser has a wavelength of 1.06  $\mu\text{m}$  which makes it suitable for triggering the GaAs semiconductor switch.

Laser intensities need to induce charge carriers is on the order of  $\text{MW}/\text{cm}^2$  [92]. Other semiconductor materials used are InP and Silicon [90]. The semiconductor material for the switch can be characterized by the photoconductive gain [94],

$$G = \tau \cdot (\mu_n + \mu_p) \cdot E / L \quad 5.1$$

in which the carrier lifetime, electron mobility and hole mobility are represented by  $\tau$ ,  $\mu_n$  and  $\mu_p$ , respectively. The electric field across the switch of length  $L$  is denoted  $E$ . GaAs has a mobility of approximately  $0.85 \text{ m}^2/\text{V}\cdot\text{s}$ , which is higher than both InP ( $0.65 \text{ m}^2/\text{V}\cdot\text{s}$ ) and Si ( $0.13 \text{ m}^2/\text{V}\cdot\text{s}$ ). In order to have a fast response, the carrier lifetime must be on order of ns; however a short carrier lifetime decreases the gain. In order to compensate for the decrease in gain, it is desirable to have material with a strong hold off voltage. The hold off field of GaAs is approximately  $200 \text{ kV}/\text{cm}$ . The surface breakdown of GaAs occurs at approximately  $40 \text{ kV}/\text{cm}$  [94]. To compensate, measures are taken to increase the breakdown strength which include coating, pressurizing the switch in  $\text{SF}_6$ , and shaping the electric field away from the switch [92]. Another way to compensate is to create a vertical switch in which the electrodes are placed on opposite sides of the material. Therefore, breakdown is determined by the bulk property of the semiconductor. The disadvantage of the electrodes placed on opposite sides of the material is a decrease in efficiency since the entire gap cannot be illuminated [89].

Because such a short gap distance is needed, the resistivity of the semiconductor material with no illumination (dark resistivity) needs to be high. GaAs and InP both have a resistivity of  $200 \text{ M}\Omega\cdot\text{cm}$ , whereas Si has a resistivity of  $200 \text{ k}\Omega\cdot\text{cm}$ . Each material has its advantages over the other. The advantage of Si is a much higher gain, and requires less laser power to trigger than GaAs or InP. However, GaAs has a much shorter carrier lifetime which allows for subnanosecond rise and fall times, while Si has a decay time in the  $\mu\text{s}$  range.

The lifetime of the switch depends on which mode it operates in. In linear mode ( $< 20 \text{ kV}/\text{cm}$ ) the switch has an almost infinite lifetime, while in the nonlinear mode ( $100 \text{ kV}/\text{cm}$ ), it

has had lifetimes as short as 10 pulses [83]. In the nonlinear mode, the filamentary discharge causes localized heating which can decrease the lifetime of the switch [95]. By using a Rogowskii profile for the electrode, the filamentary discharge is random, as in a gas switch, and local heating is reduced, effectively increasing the lifetime of the switch [89].

The advantages of photoconductive switches are low trigger jitter ( $< 10$ 's ps), optical isolation of the trigger from the switch, high repetition rate (kHz), and relatively simple circuit setup [83, 92]. The disadvantages are a limited hold off voltage (100 kV), requirement of a pulsed charging circuit opposed to DC charging due to finite leakage current of the semiconductor material, and requires a high power laser source for triggering [83, 90, 91]. However, since the trigger is isolated and the jitter is low, the switches can be stacked in series to achieve higher hold off voltages, and in parallel for higher current capabilities [92, 94]. With this technique, current densities as high as  $2 \cdot 10^6$  A/cm<sup>2</sup> have been reached [83].

#### **V.IV SUB NS PULSE GENERATORS WITH SPARK GAP SWITCHES**

Probably the most familiar types of high power subnanosecond pulse generators are those that incorporate spark gap switches [40, 76, 77]. Spark gap switches are most commonly used as capacitive discharge circuits, transmission line and Blumlein line pulse generators, and Marx Banks. They are also used to sharpen the risetime of an already existing pulse, which is dated back to 1965 [76]. McDonald and Benning used a high voltage power supply to charge a capacitor which was then discharged through a 3.8 cm 1 atm air gap through a high voltage coaxial cable. A second spark gap was pressurized with hydrogen gas at a 1 cm gap to decrease the risetime of the pulse to 100 ps at amplitudes up to 100 kV [76]. This type of switch is known as a peaking switch and is used to sharpen the risetime of pulses to values in the subnanosecond range [40, 77]. Another spark gap switch has also been incorporated to cut off the tail portion, or decaying portion of the pulse, to decrease the pulse width to subnanosecond values and is known

as a crowbar switch, or tailcut switch [40, 77]. The layout of a pulse generating system incorporating both switches is shown in Fig. 5.5.

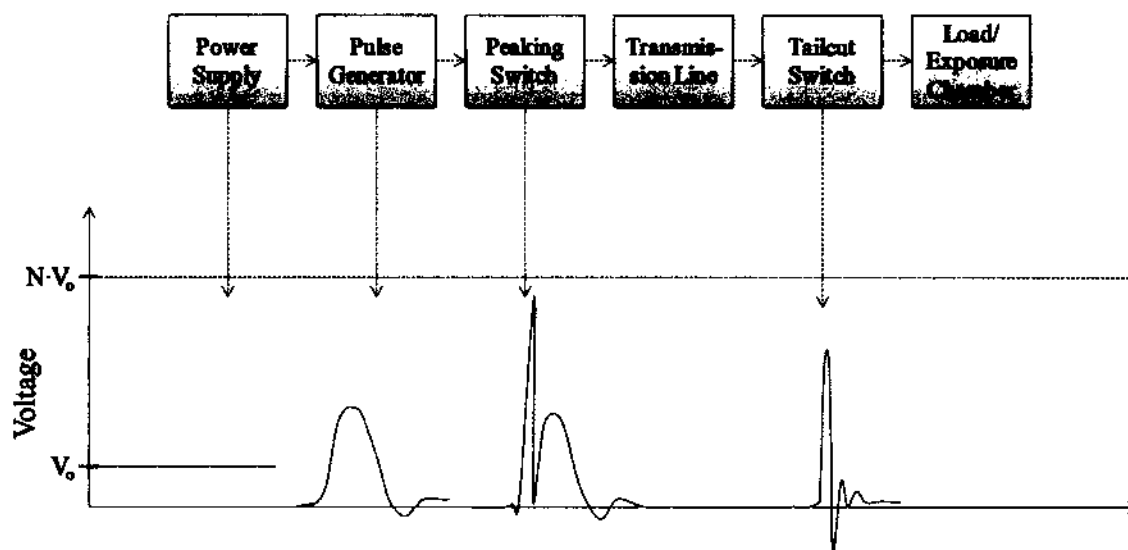
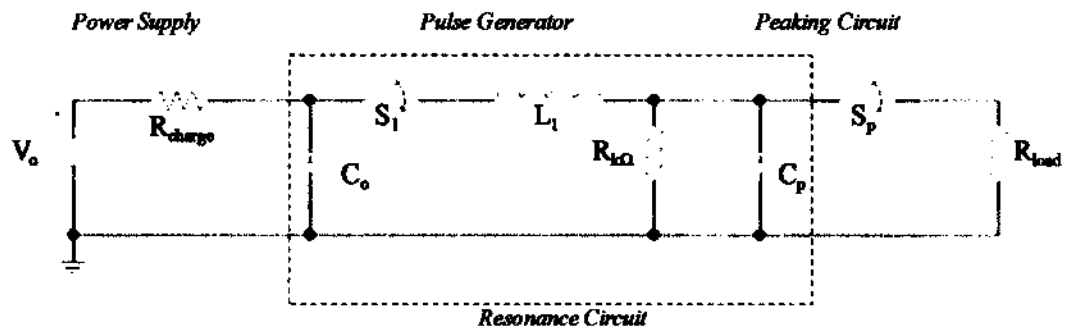


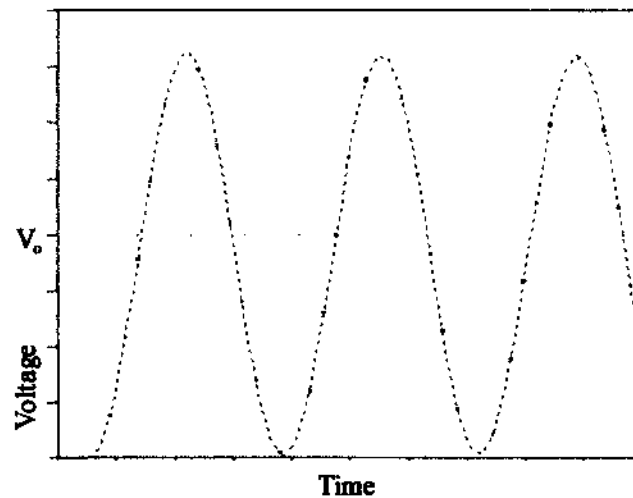
Fig. 5.5. Quantitative description of the development of a high voltage, subnanosecond pulse from a pulse generator layout incorporating a peaking and tailcut switch. The pulse generator (second stage) in this dissertation is an 8 stage ( $N$ ) Marx Bank. A peaking switch decreases the risetime of the pulse by effectively reducing the inductance of the pulse generator [40]. A tailcut switch is used to ground the decaying portion of the pulse.

The pulse generator is generally a voltage multiplier, such as a Marx Bank, pulsed transformer, or a transistor or SOS pulse generator. It can also be an energy storage component as simple as a high voltage capacitor as in [76].

The peaking switch is incorporated in a peaking circuit, which consists of a peaking capacitor. This circuit (Fig. 5.6) effectively reduces the effect of the inductance of pulse generator ( $L_1$ ) by charging the peaking capacitor ( $C_p$ ) and discharging it into the load through a path with a much lower inductance than that of the pulse generator.



*Voltage Across  $R_{k\Omega}$  without closing the peaking switch*



*Voltage Across  $R_{k\Omega}$  (broken lines) and the load (solid lines) with a closing peaking switch*

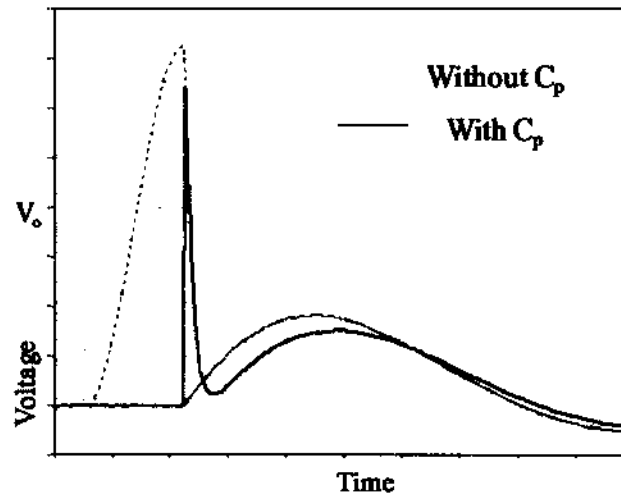


Fig. 5.6. Concept of the peaking circuit incorporating both the peaking switch ( $S_p$ ) and peaking capacitor ( $C_p$ ). The first graph is the voltage across  $R_{k\Omega}$  with (dotted black) and without (dashed gray) the peaking capacitor while the peaking switch remains open. The second graph compares the voltage across the load with the closing of the peaking switch.

The peaking capacitor is generally at least an order of magnitude less than the total capacitance of the pulse generator ( $C_o$ ) if the pulse generator is based on the capacitive discharge concept, as with the Marx Bank. The series inductance of the pulse generator ( $L_1$ ) will create a resonance charging circuit with the capacitance of the pulse generator and the peaking capacitor, effectively doubling the input voltage across the peaking capacitor (when fully charged). If the peaking switch closes ( $S_p$ ) when the peaking capacitor is fully charged, then both the capacitance of the pulse generator and the peaking capacitor will discharge into the load, resulting in a sharp pulse from the discharge of  $C_p$  into  $R_{load}$ , followed by the characteristic pulse of the  $R_{load}L_1C_1$  circuit [96].

The fast risetime of the peaking pulse is due to a small inductance between the peaking capacitor and load. The risetime and amplitude of the peaking pulse depends on the breakdown speed of the peaking switch, while the decay time depends on the  $R_{load}C_p$  time constant. Without the peaking capacitor, the pulse will only follow the trace of an  $R_{load}L_1C_1$  circuit even with the peaking switch since there is not a second capacitor to discharge into the load. The peaking capacitor can be physically placed as part of the system, or as shown in Chapter VI, can come from the stray capacitance of the switches in the pulse generator (switches of the Marx Bank).

A transmission line, usually a few meters in length, is placed between the load and the peaking circuit to separate reflections. The tailcut switch, also called a crowbar switch, is placed within the cable to break down to ground, effectively cutting off the tail portion of the pulse, as depicted in Fig. 1.9. In [40], this concept was used with a 20 stage Marx Bank and pulses with duration of 800 ps and amplitude of 200 kV were produced. In [77], pulse widths on the order of 500 ps were generated with voltage amplitudes up to 160 kV by using a high pressured hydrogen spark gap.

In order for this concept to be effective, the switches must be able to break down in the picosecond range. This fast breakdown is achieved by increasing the  $E/n$  ratio to values above 40

Td by means of pressuring and over voltaging the spark gap. A more detailed discussion of spark gap switches is covered in Appendix A.

Another approach to create subnanosecond pulses without a tailcut switch is to superimpose two pulses of opposite, but equal amplitudes, such that the pulse width is defined by the time difference between the two pulses [79, 97]. This concept is shown in Fig. 5.7.

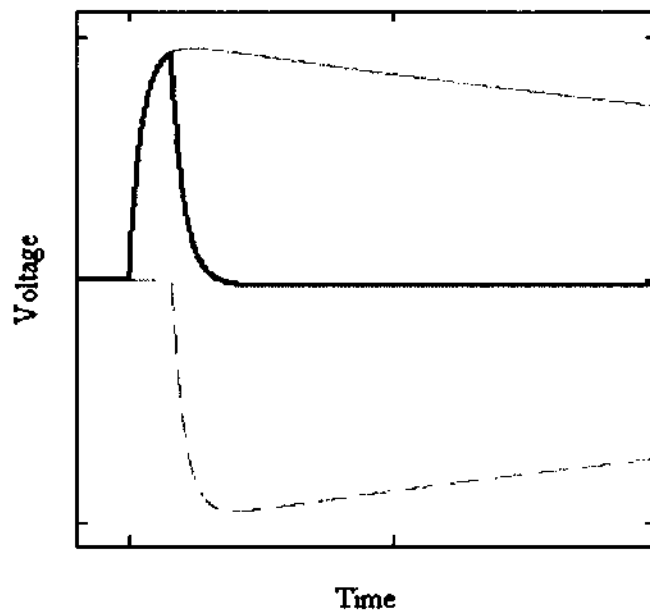


Fig. 5.7. Concept of a differential subnanosecond pulse. Two pulses of equal magnitude but opposite polarity (gray traces) are superimposed with one another with a time difference, which will define the pulse width of the resulting pulse (black trace).

Two pulses of equal magnitude but opposite polarity are superimposed with one another with a time difference which will be equal to the pulse width of the resulting pulse (black trace). A subnanosecond pulse will only be generated if the risetime of the two superimposed pulses is less than 1 ns. One way to achieve this is with two separate Marx Banks with opposite polarity under the condition the risetime of the Marx Bank pulse is below 1 ns [79]. A 6 stage, duel Marx Bank generator was used to generate a 1.5 kV pulse whose pulse width could be varied between 4 ns and 65 ns with rise and fall times on the order of 1 ns [79].



The advantage of spark gap switches is the simplicity of the design, ease of adjustment, variety of design choices, and most importantly, the ability to switch a high range of energies from  $\mu\text{J}$  to  $\text{MJ}$ . The disadvantage of spark gap switches is the repetition rate limited by the recovery time of the gas (100's of Hz), high jitter, and short lifetime due to erosion of the electrodes. There are, however, several techniques used to improve these issues (Appendix A). The advantage of a spark gap based pulse generator over those incorporating semiconductor switches is the simplicity of the design, low cost, and ability to withstand high currents and voltages in the  $10^6$  A and  $10^7$  V range, respectively.

## **CHAPTER VI**

### **DESIGN AND SETUP OF PULSE GENERATOR**

In order to expose the biological sample to high electric fields, a high voltage pulse generator was designed and built to deliver a pulse with an amplitude within the tens of kilovolt range into a load, in which the impedance is determined by the electrical properties of the biological sample. A peaking switch and tailcut switch were incorporated into the design to decrease the pulse width to 200 ps. This chapter will focus on the design of the pulse generator. In order to characterize the pulse generator, the resistive load of  $50\ \Omega$  was chosen (low inductance carbon based resistor), and connected at the end of a 14 cm  $50\ \Omega$  coaxial cable. In order to measure the pulse delivered to the load, a capacitive voltage divider (Chapter VIII) was incorporated into the coaxial cable 1.7 mm in front of the load. The overall design of the pulse generator is discussed in section VI.I, followed by a detailed discussion on the Marx Bank (VI.II), peaking switch (VI.III) and tailcut switch (VI.IV).

#### **VI.I DESIGN OF SUB NS PULSE GENERATOR**

The pulse generator used for this dissertation is based on the design used in [40], which follows the model shown in Fig. 4.4. The entire design is based off the concept discussed in Chapter V, in which a peaking switch and tailcut switch are used to shape the pulse. A negative DC input voltage between 5 kV and 15 kV in amplitude is fed into an 8 stage Marx Bank as depicted in Fig. 6.1a.

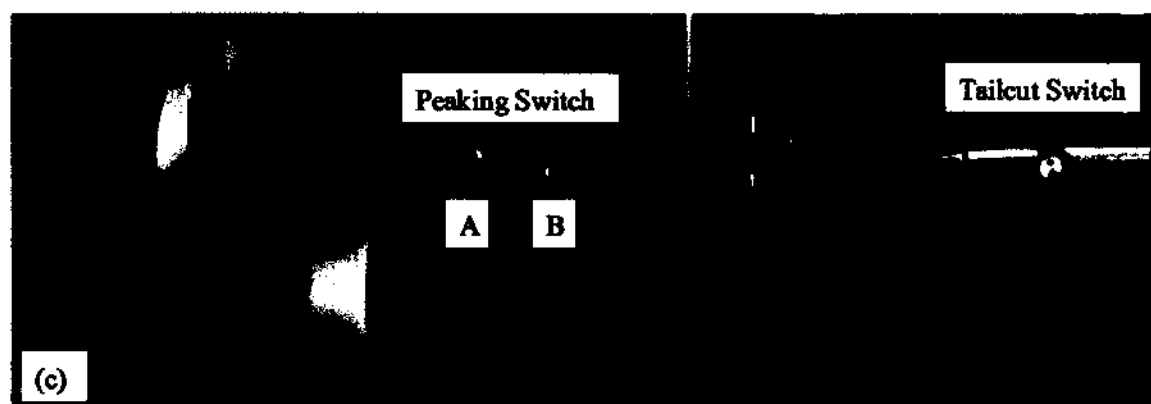
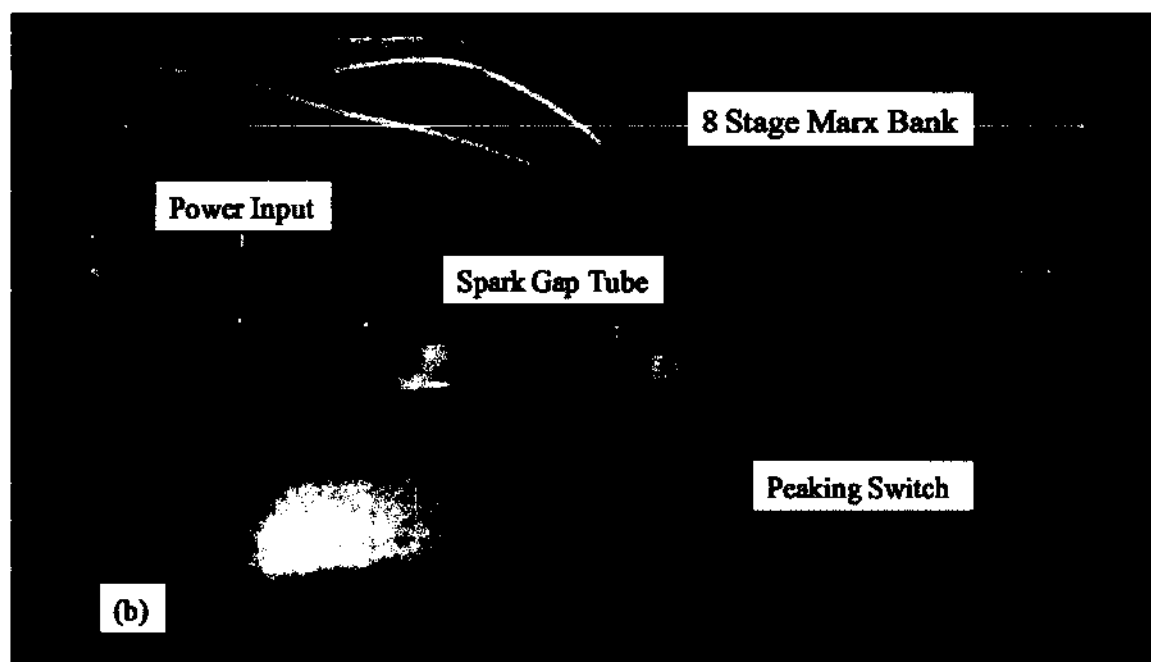
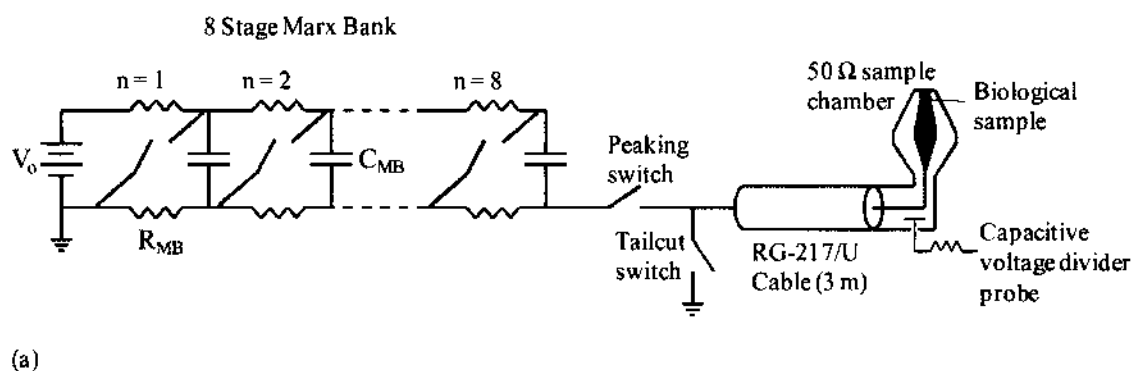


Fig. 6.1. (a) Conceptual layout of the subnanosecond pulse generator. An 8 stage Marx Bank feeds into a  $50\ \Omega$  cable through a peaking switch. A tailcut switch is placed within the cable. The load is a conical exposure chamber. The voltage is measured with a capacitive voltage divider placed in front of the exposure chamber. (b) Photograph of the Marx Bank and peaking switch. (c) Photograph of the peaking switch and tailcut switch. The electrodes of the peaking switch are labeled "A" and "B" for discussion purposes.

A peaking switch is placed at the output of the Marx Bank which causes a sharpening of the output pulse. A tailcut switch is placed within the cable to cut off the decaying portion of the pulse, thus decreasing the width and amplitude of the pulse. A voltage pulse varying from 10 kV to 20 kV, with a pulse width on the order of 200 ps is a result of the system. The pulse width and amplitude are adjusted by adjusting the gap distance of the peaking and tailcut switch. The pulse repetition rate is limited to 25 pps due to the charging time of the Marx Bank.

## VI.II MARX BANK

The Marx Bank consists of 8 stages ( $N$ ), each with a capacitance ( $C_{MB}$ ) and charging resistance ( $R_{MB}$ ) of 2.3 nF (2 nF measured) and 100 k $\Omega$ , respectively. The capacitors used are ceramic door knob capacitors with a hold off voltage of 40 kV (RF Parts, San Marcos, California). The Marx Bank is triggered by applying a DC voltage across the first switch causing breakdown, which triggers the following switches. The switches are composed of brass electrodes with a semi-spherical shape and are placed in a tube and pressurized with nitrogen between 1 and 3 atm.

The first set of electrodes is placed 1.5 mm apart while the remaining 7 are placed 2.5 mm apart. This placement is to insure self breakdown at the first electrode at all times. The time between closing of the first and second switch was measured to be 10 ns, while the time between the remaining switches was 1 ns. The decrease in delay may be a result of the increase in voltage across the remaining switches, which results in a shorter delay in breakdown. After all the switches close ( $\approx 16$  ns time span), the Marx Bank is erected, and its equivalent circuit is a capacitor ( $C_{MB}/N$ ) charged up to  $N \cdot V_{in}$  in series with an inductor (which is determined by the circuit components and wiring of the stages) and the load. The simplified schematic of the Marx Bank (neglecting capacitance of Marx Bank switches) is shown in Fig. 6.2.

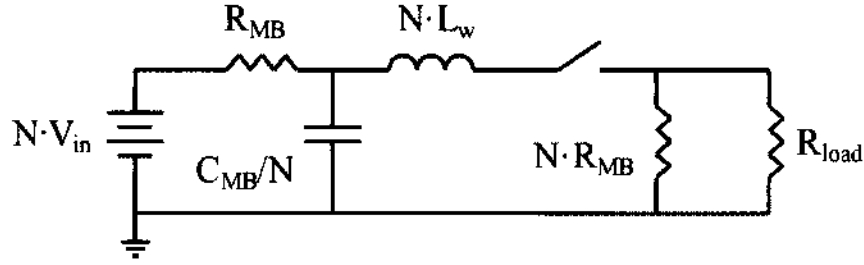


Fig. 6.2. Equivalent circuit of erected Marx Bank. The individual stage capacitance and inductance is represented by  $C_{MB}$  and  $L_w$ , respectively. The charging resistor of each stage is denoted  $R_{MB}$  and  $N$  is the number of stages.

The load resistor is denoted  $R_{load}$ , and the inductance of each stage is denoted  $L_w$ , which is largely determined by the wire conductor which connects the capacitors, switches, and resistors. The connections between each stage have approximately a circular shape. Accordingly, the inductance of a single loop,  $L_w$ , can be calculated as:

$$L_w = \mu \cdot R_L [\ln(8 R_L / R_w) - 1.75] \quad 6.1$$

with  $\mu$  being the permittivity of free space [98]. With the radius of the loop,  $R_L$ , being 40 mm, and the radius of the wire,  $R_w$ , being 1.5 mm, the inductance is approximately 182 nH. The total inductance of the erected Marx Bank, with 8 stages is consequently 1.45  $\mu$ H.

The shape of the voltage pulse across the resistive load (without the peaking or tailcut switch) is determined by the properties of a series RLC circuit. The pulse is critically damped when the load is equal to

$$R_{load} = 2N\sqrt{L_w/C_{MB}} = 150 \, \Omega \quad 6.2$$

for an  $N$  of 8, and a stage capacitance and inductance of 2 nF and 182 nH, respectively. A load of 50  $\Omega$  will give an underdamped pulse as shown in Fig. 6.3.

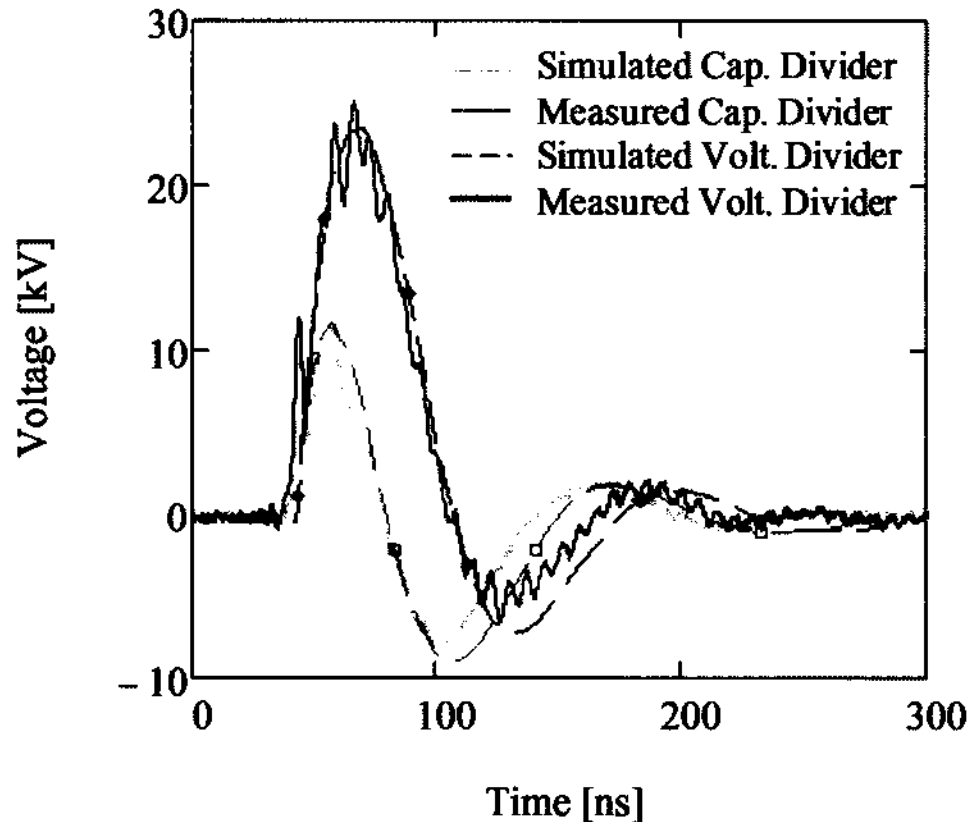


Fig. 6.3. The comparison of the measured voltage (solid) to the simulated voltage (dashed) for an 8 stage Marx Bank with a  $50\ \Omega$  load. The black traces represent the voltage measured and simulated with a resistive voltage divider, and the gray traces are those measured and simulated with a capacitive voltage divider whose time constant is 8.3 ns (Chapter VIII).

Figure 6.3 is a comparison of the output voltage of a Marx Bank across a  $50\ \Omega$  load (8 kV input) between the simulated (dashed lines) and experimentally measured (solid lines) voltage. The gray line represents the voltage measured with a capacitive voltage divider (Chapter VIII) displayed on a 4 GHz oscilloscope (TDS-7404), and the black lines represent the measurements obtained with a voltage divider probe (Tektronix P6015A, 75 MHz) displayed on a 100 MHz oscilloscope (TDS-3012B). The rise time (10%- 90%) of the voltage pulse was measured to be 17 ns. The results in Fig. 6.3 suggest that the RLC series circuit with the calculated value of  $L_w$  accurately characterizes the temporal development of the erected Marx Bank voltage. The time constant of the capacitive divider probe is 8.3 ns (Chapter VIII) and is therefore differentiating

the voltage. However, when incorporating the peaking switch, the capacitive probe will be able to accurately measure the voltage whereas the voltage divider probe will not due to its limited bandwidth of 75 MHz.

The frequency of the oscillations superimposed on the pulse is approximately 200 MHz. Although this frequency is larger than the bandwidth of the resistive probe, it is also measured with the capacitive probe which would suggest it is not due to either probe. This effect decreases with a decreasing number of stages, as shown in Fig. 6.4 in which the voltage was measured (capacitive divider) for a 1, 2, and 8 stage Marx Bank. When the 1 stage Marx Bank switch closes, the voltage across the load follows that of an  $R_{load}L_{MB}C_{MB}$  circuit. However, when a second stage is added, there is a slight oscillation at a frequency of 143 MHz in the front of the pulse, which is not characteristic of the  $R_{load}2 \cdot L_{MB}C_{MB}/2$  circuit. For an 8 stage Marx Bank, the effect is very evident. It is unclear on the exact reason behind the oscillations, but it is evident that they only occur when more than one Marx Bank stage is used. It was believed the effect is due to a delay in the closing of the Marx Bank switches. However, this effect cannot be simulated in PSpice. The switches were modeled as an ideal step function switch in series with the respected inductance of the switch and in parallel with the capacitance of the switch. The delay between the closing of the first and second switch was 10 ns and 1 ns between the remaining switches. Other variations in delay were also simulated. It may be possible the oscillations come from the temporal development of the switch which PSpice cannot model, such as plasma oscillations of the switch, stray capacitance, and/or nonlinear changes in the inductance and resistance of the switch during breakdown formation.

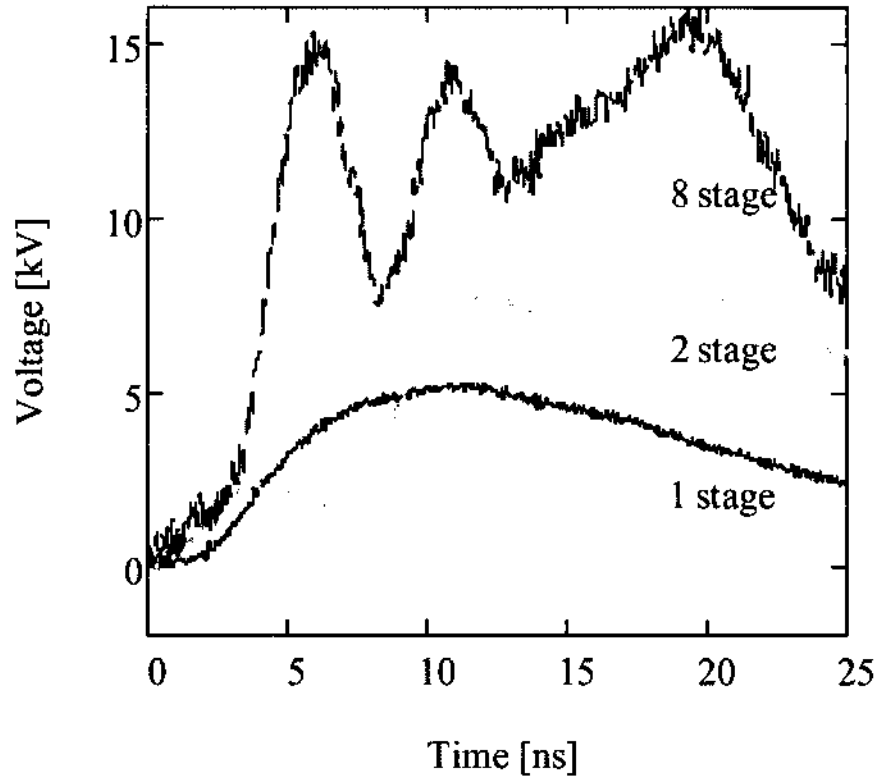


Fig. 6.4. Voltage measured with a capacitive voltage divider across a  $50 \Omega$  load for a 1, 2, and 8 stage Marx Bank without a peaking switch. The 1 stage Marx Bank does not have oscillations in the pulse whereas the 2 and 8 stage do.

The inductance at each stage of the Marx Bank limits the ratio of the output voltage to the input voltage. This ratio, dependent on the number of stages, is equal to

$$V_{out}/V_{in} = (2 \cdot R_{load}/L_w \cdot \beta) \cdot \exp(-(R_{load} \cdot t_{max}/2 \cdot L_w \cdot N)) \cdot \sin(0.5 \cdot t_{max} \cdot \beta) \quad 6.3.a$$

$$\beta = \sqrt{(4/L_w \cdot C_{MB}) - \sqrt{R_{load}/N \cdot L_w}} \quad 6.3.b$$

$$t_{max} = 2 \cdot \tan^{-1}(-\beta \cdot L_w \cdot N/R_{load})/\beta \quad 6.3.c$$

The time at which the voltage reaches its maximum value ( $dV/dt = 0$ ) is denoted  $t_{max}$ . Equation (6.3) was derived by solving for the response of an RLC circuit with  $L$  being  $N \cdot L_w$  and  $C$  being  $C_{MB}/N$ . With an input of 8 kV, the maximum output determined from (6.3) with 8 stages is 27



kV, which is within 1 kV of the measured output shown in Fig. 6.3 (26 kV). In order to achieve an output voltage of 35 kV (with an input of 8 kV), a minimum of 22 stages is required. As the number of stages is increased to infinity, the overall limit of the system is defined as:

$$V_{out}/V_{in} = R_{load}\sqrt{C_{MB}/L_w} \quad 6.4$$

The ratio for the Marx Bank used for this pulse generator is equal to 5.2 with a load of 50  $\Omega$ . In other words, with an 8 kV input, the maximum output voltage attainable with an infinite number of stages is 42 kV.

## VI.III PEAKING SWITCH

### VI.III.I Peaking Switch Geometry

Peaking switches are commonly used with Marx Banks, generally in combination with a shunt capacitor (or peaking capacitor) in front of the switch [40, 96]. If the peaking capacitor is on the order of a magnitude less than the total capacitance of the erected Marx Bank, then the maximum voltage across the switch (prior to breakdown) is twice that of an erected Marx Bank with an infinite load ( $2 \cdot V_{in} \cdot N$ ). However, due to the small gap distance of the peaking switch in this system ( $< 5$  mm) and without pressurizing the air, the voltage will not reach this maximum attainable value before breakdown of the peaking switch occurs.

The peaking switch in this system consists of two spherical electrodes made of brass with a diameter of 1.9 cm. The capacitance between the electrodes was calculated to be between 0.74 pF and 0.4 pF for a gap distance between 0.5 mm and 8 mm, respectively. The inductance of the peaking switch depends on the radius of the spark gap channel, which can be approximated by the Braginskii Model (Appendix A) and is approximately 1 nH for a gap distance of 2 mm. The first electrode (electrode A, Fig. 6.1(c)) is connected to the output of the Marx Bank, and the second electrode (electrode B) is connected directly to the inner conductor of a 50  $\Omega$  output cable (R-

217/U). The gap distance can be varied from 0 mm to 10 mm, and operates at atmospheric pressure in air.

### VI.III.II Peaking Circuit

The peaking capacitance in this system comes from the capacitance between the electrodes of the spark gap in the last stage of the Marx Bank. Therefore, the placement of an external peaking capacitor is not required. The circuitry of the peaking circuit is shown in Fig. 6.5 for a one stage Marx Bank.

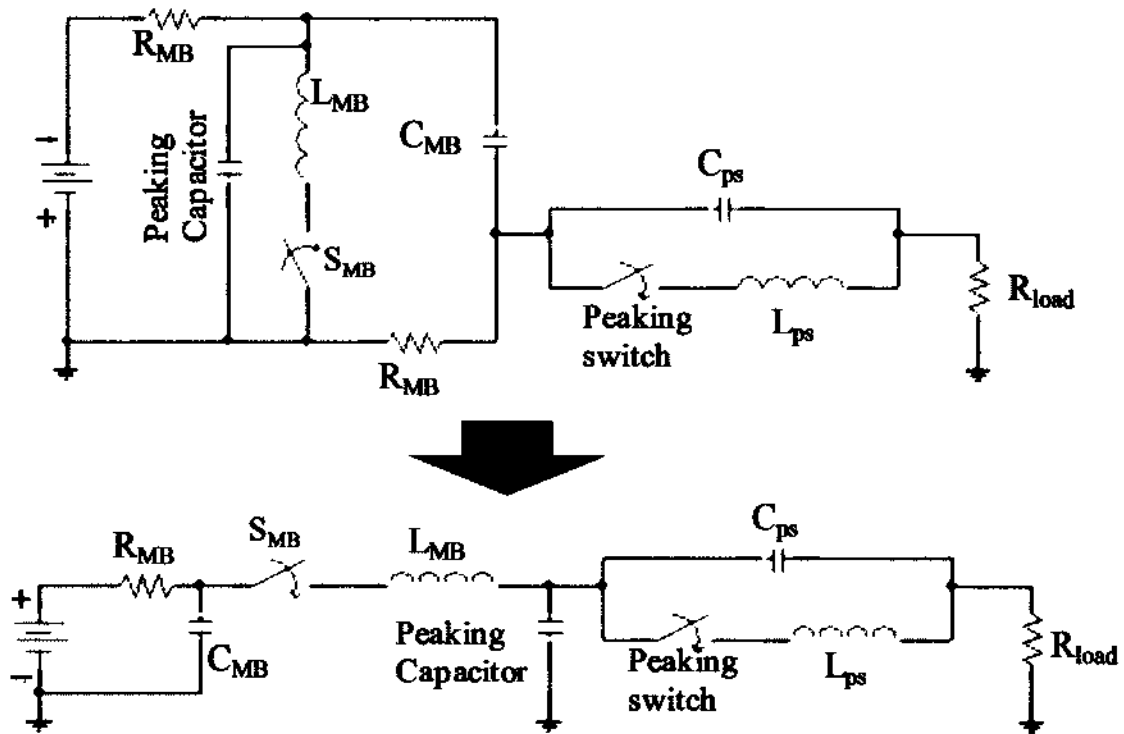


Fig. 6.5. The circuit diagram of the peaking circuit connected to the output of a 1 stage Marx Bank. Both the peaking switch and Marx Bank switch are represented by their respected capacitance and inductance. The capacitance of the Marx Bank switch makes up the peaking capacitor. The arrow points to the equivalent circuit, which is similar to Fig. 4.5.

The capacitance and inductance between the electrodes of the peaking switch are denoted  $C_{ps}$  and  $L_{ps}$ , respectively. In order to create a short risetime,  $L_{ps}$  should be at least an order of magnitude

smaller than the inductance of the single stage of the Marx Bank,  $L_{MB}$ . The peaking capacitor is the capacitance between the electrodes of the single stage Marx Bank switch,  $S_{MB}$ , and is calculated to be approximately 0.5 pF for a gap distance of 2 mm. Typically, due to the small surface area of the electrodes, the peaking capacitance is orders of magnitude less than the capacitance of the single stage charging capacitance of the Marx Bank,  $C_{MB}$ .

If sufficiently large, the capacitance and inductance of the peaking switch will introduce oscillations at the front of the pulse once the peaking switch closes. The frequency and decay constant of the oscillations can be approximated by

$$f \approx \left| \frac{1}{4\pi} \sqrt{[L_{ps}^2 - 4 \cdot R_{load}^2 \cdot L_p \cdot C_{ps}] / [R \cdot L_{ps} \cdot C_{ps}]^2} \right| \quad 6.5.a$$

$$\tau \approx \frac{8}{3} \pi [L_{ps} \cdot C_{ps}] / [R_{load} \cdot C_{pc}] \quad 6.5.b$$

respectively. These equations are valid for  $L_{ps} < 4 \cdot R_{load}^2 \cdot C_{ps}$ . In order to determine an expression for the frequency and decay constant, the circuit in Fig. 6.5(b) was solved by removing the electrical components of the Marx Bank and solving only for the peaking circuit. This circuit resulted in a 3<sup>rd</sup> order differential equation in which the condition  $L_{ps} < 4 \cdot R_{load}^2 \cdot C_{ps}$  was invoked in order to determine an analytical solution. If  $L_{ps} > 4 \cdot R_{load}^2 \cdot C_{ps}$ , the system is overdamped, in which case no oscillations will occur. For a peaking switch gap distance of 2 mm, the frequency and decay time constant are 6 GHz and 0.18 ns, respectively. A decrease in the gap distance will cause an increase in the oscillation frequency, while an increase in the gap distance has the opposite effect.

As the number of Marx Bank stages increases, the peaking capacitance will theoretically decrease by  $C_{pc}/N$  which will not have an effect on the frequency, but will increase the decay time constant for a constant peaking switch gap distance. However, this assumption is based on the Marx Bank switches closing at the same time. Realistically, there is a delay between the closing

of the switches in the Marx Bank, which may cause only the last stage of the Marx Bank to act as the peaking capacitor. This explanation is validated by the fact that the fall time of the peaking pulse, (VI.III.IV) is approximately the same for a 1 stage and an 8 stage Marx Bank. The decay time of the peaking pulse is defined by the  $R_{load}C_{pc}$  time constant (Chapter IV) and is 25 ps for a 50  $\Omega$  load and a peaking capacitance of 0.5 pF. A peaking capacitance of 0.063 pF (0.5/8) would result in a decay constant of 3 ps, which cannot be recorded due to the limited bandwidth of the voltage probe and the oscilloscope (4 GHz).

#### **VI.III.IV The Effect of the Number of Stages on the Peaking Pulse**

Voltage measurements of a single and 8 stage Marx Bank with and without the peaking switch across a 50  $\Omega$  load with an input voltage of 13 kV are shown in Fig. 6.6. Fig. 6.6(a) is for 1 stage and Fig. 6.6(b) is for an 8 stage Marx Bank. The voltage measurements were made with the capacitive voltage divider. The gray traces represent a closed peaking switch, and the black traces are an open peaking switch with a gap distance of 0.5 mm for the 1 stage and 2 mm for the 8 stage. For the one stage Marx Bank, the risetime in the voltage from 0 to 5 kV (amplitude of the first peak) decreased from 4.5 ns to 150 ps. The pulse width of the peaking pulse is approximately 450 ps. For the 8 stage Marx Bank, the risetime in the voltage from 0 to 18 kV for the closed switch is approximately 3.3 ns. With the peaking switch gap at 2 mm, the risetime in voltage from 0 to 24 kV (amplitude of the first peak) decreased to 160 ps, which is also the pulse width of the peaking pulse (FWHM). As will be shown in the next section, there is an optimum gap distance to achieve the highest voltage. However, there is a consistence increase in the pulse width with an increase in gap distance.

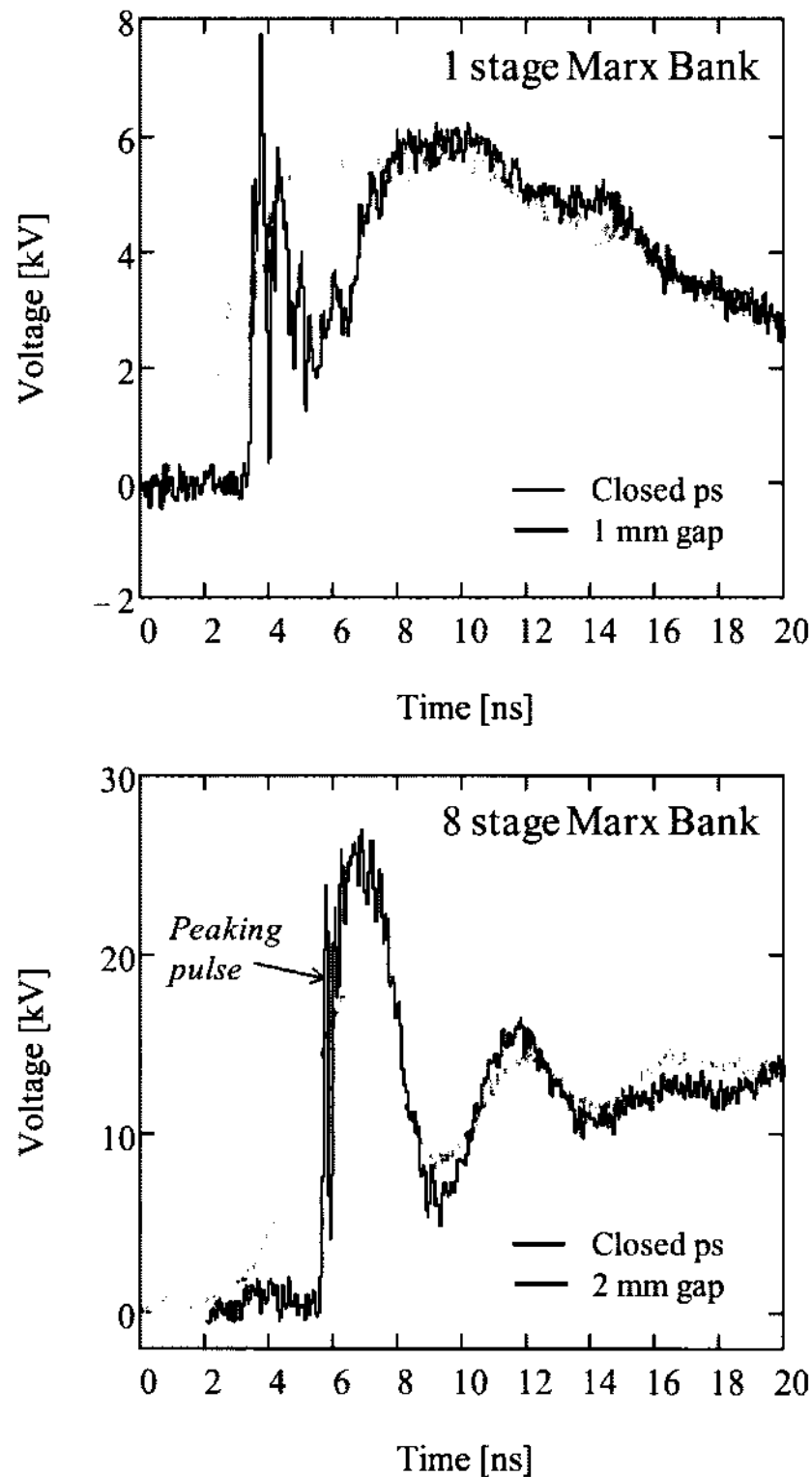


Fig. 6.6. (a) Voltage measured across a 50 ohm resistor with a capacitive voltage divider for a 1 stage Marx Bank whose input voltage is 13 kV. The gray trace is with a closed peaking switch, and the black trace represents an open peaking switch with a gap distance of 2 mm. (b) Same conditions as in (a) except with an 8 stage Marx Bank.

### VI.III.V Varying the Gap Distance

For the 8 stage Marx Bank with an input voltage of 8 kV and 12 kV, the gap distance of the peaking switch was varied between 0 mm and 8 mm. The voltage across the load, measured with the capacitive voltage divider, is shown in Fig. 6.7 for both the 8 kV and 12 kV input conditions.

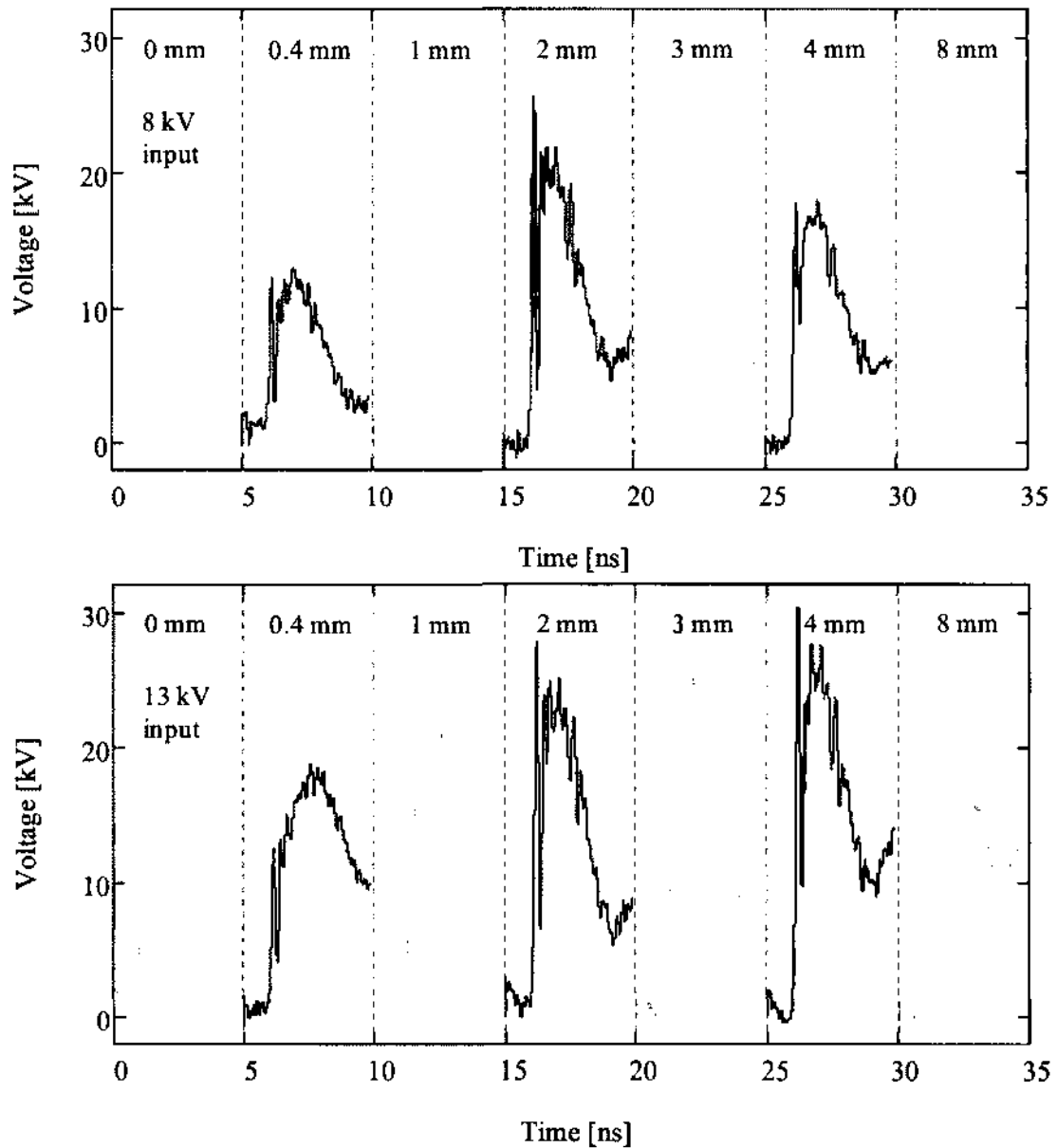


Fig. 6.7. Voltage measured across the load for an 8 stage Marx Bank with an input voltage of 8 kV in which the peaking switch gap distance is varied between 0 mm and 8 mm. The optimized gap distance occurs at approximately 2 mm for the 8 kV and 3 mm for the 12 kV input.

The optimization of the peaking switch occurs when the amplitude of the peaking pulse voltage is at its highest, which occurs at approximately 2 mm for the 8 kV input and 3 mm for the 12 kV input. As the input voltage is increased, the optimized distance of the spark gap is increased. As the gap distance is increased beyond the optimization distance, the amplitude of the voltage is decreased until the effect of the peaking capacitance is no longer observed. This effect is due to the breakdown properties of the peaking switch; a larger gap distance not only increases the inductance of the switch, but also increases the time required for the switch to go from a conductive state from a nonconductive state. The condition for fast breakdown occurs when the ratio of the electric field and the gas density reaches values greater than 40 Td (Appendix A). The breakdown voltage of the peaking switch was measured with the Tektronix voltage divider. The Townsend value ( $V_{bd}/d \cdot n$ ) of each condition of Fig. 6.7 is shown in Table 6.1, along with the breakdown voltage and pulse width (FWHM) of the peaking pulse created by the peaking capacitor.

$V_{in}$		Gap Distance [mm]					
		0.5	1	2	3	4	8
8 kV	$V_{bd}$ [kV]	14	23	38	39	43	46
	$E/n$ [Td]	105	90	77	55	47	30
12 kV	$V_{bd}$ [kV]	22	35	40	48	49	60
	$E/n$ [Td]	165	135	81	68	59	39

Table 6.1. The breakdown voltage and  $E/n$  ratio of the peaking switch, along with the pulse width of the peaking pulse for an 8 kV and 12 kV input voltage to an 8 stage Marx Bank.

The pulse width is indirectly proportional to the Townsend coefficient in that a decrease in Td causes an increase in the pulse width. As the amplitude of the breakdown voltage across the gap increases, the amplitude of the peaking pulse increases until the Townsend coefficient reaches a

value of approximately 55 Td for both the 8 kV input and 12 kV input condition. At this point, the time it takes for the peaking switch to reach a conductive state once breakdown is initiated may be increased. A slower decrease in the resistance of the channel may cause the peaking capacitor to discharge its voltage across the resistance of the switch rather than the load. By the time the resistance of the switch decreases below the load resistance, a less amount of voltage from the peaking switch is discharged into the load. Once the value of the Townsend coefficient reaches values below 40 Td, which is an approximate requirement for subnanosecond breakdowns, the peaking pulse is no longer observed.

#### **VI.IV TAILCUT SWITCH**

In this section, the 14 cm cable was replaced with the 3 meter 50  $\Omega$  cable used in the experimental setup. The load continued to be the 50  $\Omega$  low inductance, carbon based resistor. The tailcut switch in this system was integrated into the cable. The pulse front traveling along the cable to the load causes the voltage at the inner conductor to break down to the outer conductor of the cable by the use of a needle electrode 1 mm in diameter. The 50  $\Omega$  cable with polyethylene insulator is connected to a 1 cm long 50  $\Omega$  cable with air insulator and back to the RG-217/U cable. The needle electrode is placed within the air insulated portion of the cable. This setup allows the signal to travel with negligible disturbance through the tailcut switch. This arrangement decreases the jitter of pulses by having the breakdown occur strictly between the two electrodes rather than the wall of the hole of the insulator (surface breakdown). The pulse duration in this system is determined by the delay time from the application of the pulse across the switch to its full breakdown. By varying the gap distance of the tailcut switch, it is possible to vary this delay time [40], and consequently determine the pulse width and amplitude across the load. A larger pulse width is associated with a higher amplitude.



Figure 6.8 compares the voltage across the load with and without the tailcut switch for an input of 8 kV into the 8 stage Marx Bank. The gap of the peaking switch was set to 2 mm, which was the optimum gap distance for an 8 kV input, as shown in the previous section.

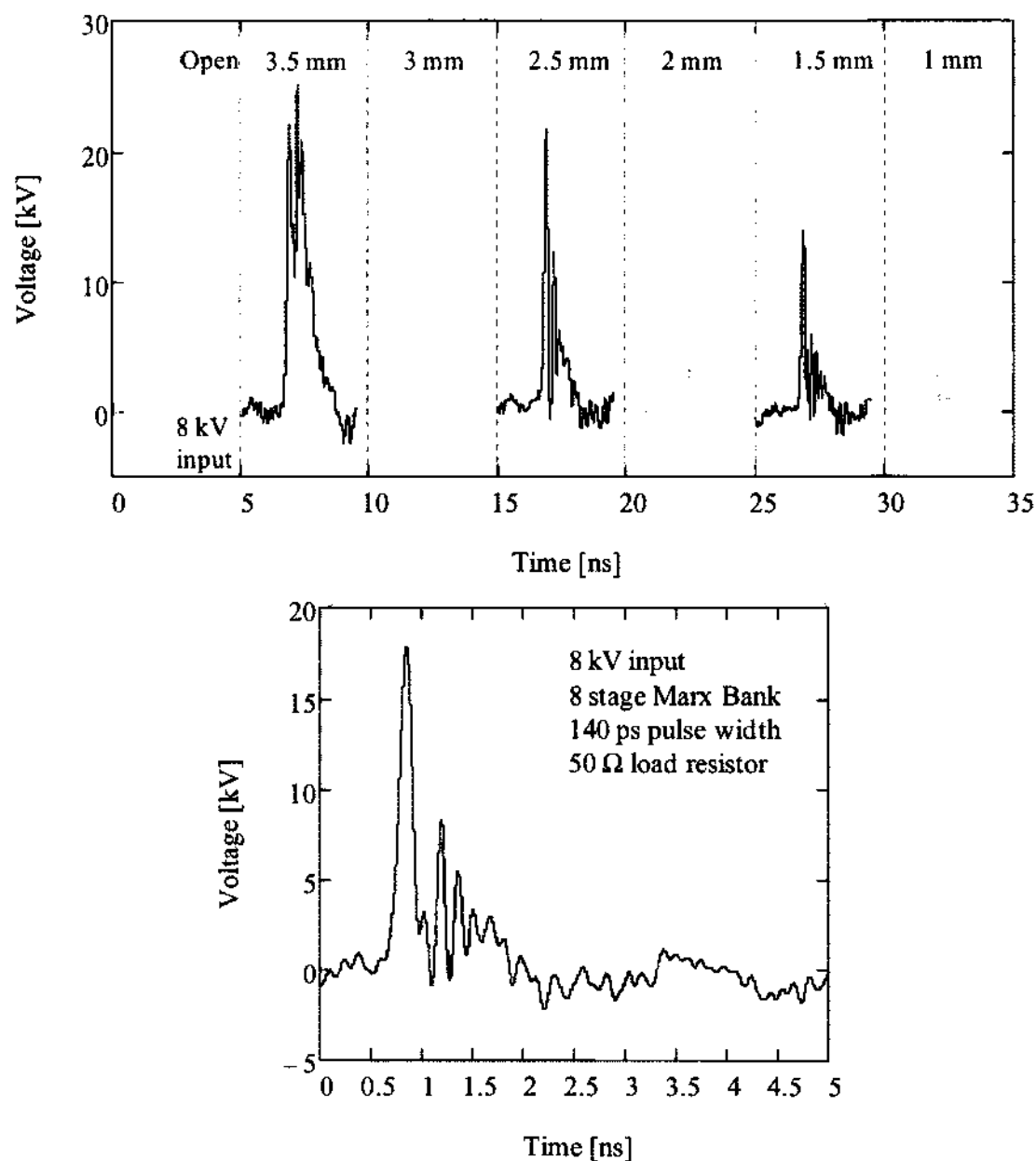


Fig. 6.8. Voltage measured in front of the load with varying tailcut switch gap distances. The input voltage to the 8 stage Marx Bank was 8 kV, and the peaking switch gap distance was set to 2 mm.

Figure 6.8(a) is the voltage across the  $50\ \Omega$  load with the tailcut switch gap distance varying from 3.5 mm to 1 mm. The pulse width of the peaking pulse is equal to 140 ps, and is eventually the final output pulse of the system once the tailcut switch shorts out the remainder of the pulse. The pulse for the 2 mm tailcut switch gap distance is shown in a higher resolution in Fig. 6.8(b).

## CHAPTER VII

### DESIGN AND SETUP OF EXPOSURE CHAMBER

The load consists of a biological sample which was placed in an exposure chamber between disc-shaped electrodes made of stainless steel. The exposure chamber was designed to provide a uniform electric field between 50 kV/cm and 120 kV/cm across the biological sample at pulse amplitudes ranging from 10 kV to 20 kV. The electrode separation in the chamber was, consequently, 1.8 mm. In order to provide a sample volume of 30  $\mu\text{L}$ , a minimum volume required for the biological analysis, the radius of the electrodes must exceed 2.3 mm. A radius of 2.4 mm was chosen, which resulted in a sample volume of 32.5  $\mu\text{L}$ .

The conductivity and the permittivity of the medium in which the biological cells were placed (complete medium containing Dulbecco's Modification of Eagle's Medium (Cellgro, Fisher Scientific cat# 10-013-CV) supplemented with 10% FBS (Cellgro, Fisher Scientific cat#35-015-CV)), which was used for the cell suspension, was measured by means of Time Domain Dielectric Spectroscopy [51] at frequencies of 100 MHz and 1 MHz for varying temperatures (Table 7.1). Assuming that the electrical parameters of the medium are identical to the cell suspension, a reasonable assumption considering the relatively small concentration of cells in the medium (0.314%), these values were used to calculate the resistance and capacitance of the sample. With a conductivity of 1.37 S/m and a relative permittivity of 79.3 at room temperature (25°C), the sample resistance and capacitance was calculated as 72.6  $\Omega$ , and 7 pF, respectively. However, since the gap distance is comparable to the electrode radius, the standard equation for parallel-plate capacitors, which was used in the calculation, needs to be modified in order to take the fringe fields into account. This could result in a smaller value of the capacitance, as will be shown at the end of the chapter.

Electrical Parameters of the Medium in the Chamber				
T (°C)	Permittivity	Conductivity [S/m]	C [pF]	R [Ω]
25	79.3	1.37	7	72.6
37	72.7	1.74	6.7	57.2
42	67.6	1.88	6	53
47	64.1	2.03	5.7	49

Table 7.1: Permittivity and conductivity of the medium used for the cell suspension depending on temperature. Also listed is the resulting capacitance and resistance of the sample.

Since the radius of the sample (2.4 mm) is larger than the radius of the inner conductor (1.34 mm) of the 50 Ω cable which connects to the chamber, a coaxial waveguide was designed and built (Fig. 7.1(a)) which expanded the inner conductor to the electrode diameter of the exposure chamber, while maintaining the 50 Ω impedance over the entire length from the cable to the chamber. The dielectric between the inner and outer conductor was polypropylene with a permittivity of 2.38, the same as that of the cable. The shape of the waveguide, with its conical shape at the chamber, is such that it allows a rather smooth transition from the transverse electric fields in the cable to the axial electric field in the sample [36].

In order to determine the distribution of the electric field within the sample, a three-dimensional, time dependent electromagnetic field solver (MAGIC) was used [37]. A voltage pulse of 200 ps with an amplitude of 10 kV was used in the simulation. The values of conductivity and permittivity of the sample were taken from Table 7.1 for room temperature. The axial electric field was calculated from the high voltage electrode to the ground electrode (0 mm – 1.8 mm) and from the inner radius to the outer radius (0 mm – 2.4 mm). The results are shown in Fig. 7.2. The insert in Fig. 7.2 is the enlarged exposure chamber (shown in white) between the two electrodes (shown in black). The letters (w, x, y, z) represent the axial positions at which three lateral positions at  $D = 0.1$  mm, 0.9 mm, and 1.78 mm between the electrodes, the electric

field values shown in Fig. 7.2 were obtained. The results show a good homogeneity in the axial direction with less than a 1.5% deviation. The electric field is less homogeneous in radial direction. It decreases from the center to the outer radius of the sample by 9.4%.

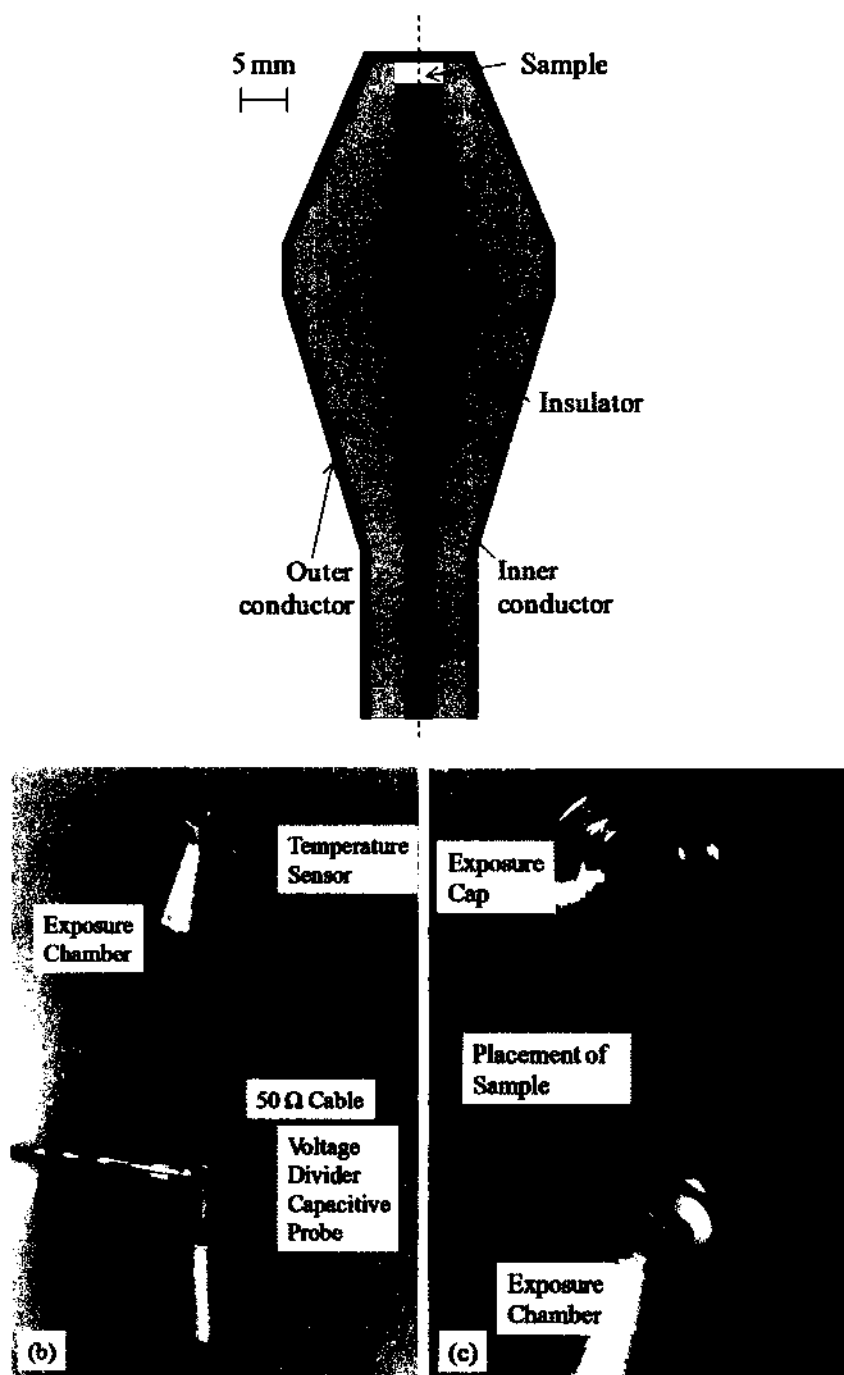


Fig. 7.1. (a) Dimensions of the exposure chamber created with MAGIC. (b) Photograph of the exposure chamber and voltage probe. (c) Photograph of the interior of the exposure chamber.

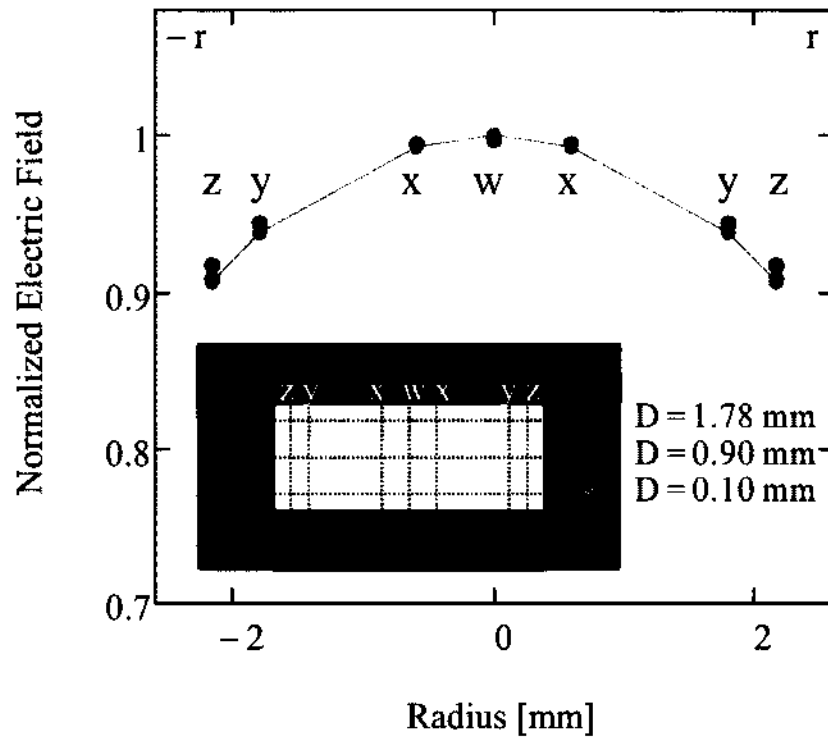


Fig. 7.2. Results of the electric field distribution within the sample using MAGIC. The insert shows the electrodes in dark gray and the sample in light gray. The letters “w” – “z” represent where in the sample the electric field was simulated. The highest electric field occurs in the center of the sample, and deviates less than 10% at the edges.

The non-uniform electric field may account for a decrease in the capacitance for the following simple qualitative reason. The capacitance of a parallel plate (neglecting fringe effects) is defined as  $C = \epsilon \cdot A/d$  in which  $A$  is the surface area of the electrode and  $d$  is the gap distance. The electric field between two plates is defined as  $E = V/d$ . By substituting in for  $d$ , we can express the capacitance in terms of the electric field:  $C = \epsilon \cdot A \cdot E/V$ . If the assumption is made that  $V$  is constant across the total surface area of the electrode, and  $E$  is a function of the radius of the electrode, as shown in Fig. 7.2, then the total capacitance of the chamber can be expressed as:

$$C = \frac{2 \cdot \epsilon \cdot \pi}{V} \cdot \int_0^{r_{outer}} E(r) \cdot r \cdot dr \quad 7.1$$

For a constant electric field, (7.1) reduces to the familiar equation associated with a parallel plate capacitor. From Fig. 7.2, we can approximate the electric field as a function of the radius with,

$$E(r) = E_o \cdot [1 - r \cdot (0.1/2.4 \text{ mm})] \quad 7.2$$

in which  $E_o = V/d$ . The value of the capacitance at room temperature, based on the electric field distribution in Fig. 7.2, is 6.5 pF, which is approximately 7% less than the calculated capacitance.

## **CHAPTER VIII**

### **VOLTAGE MEASUREMENTS**

Due to its encapsulation (Fig. 7.1), the voltage across the sample cannot be measured directly. Instead, a capacitive voltage divider measures the incoming voltage pulse from the Marx Bank towards the sample, which is superimposed with any reflected signal from the load. The placement of the probe is 9.23 cm in front of the load, resulting in a 0.95 ns time difference between the voltage towards the load and the reflected voltage. The reflected signal can be used to obtain the electrical characteristics of the load (capacitive, resistive, and inductive). As shown in Table 7.1, the load, which consists of the biological sample, has a capacitive and resistive component, which changes with a change in temperature. Therefore, with a constant input voltage, the voltage across the load is dependent on the temperature of the sample.

This chapter is divided into three sections; the first section covers the voltage diagnostics used to measure the voltage. The second section discusses the properties of a reflected signal for a capacitive and resistive load opposed to just a resistive load. The third section shows the steps and derivations needed to obtain the actual voltage across the load based on the measured voltage in front of the load. The measured voltage is then compared to simulations using P-Spice.

#### **VIII.1 VOLTAGE DIAGNOSTICS**

The voltage is measured with a capacitive voltage divider 9.23 cm in front of the load (4.5 cm from end of cable) within the cable as shown in Fig. 8.1.



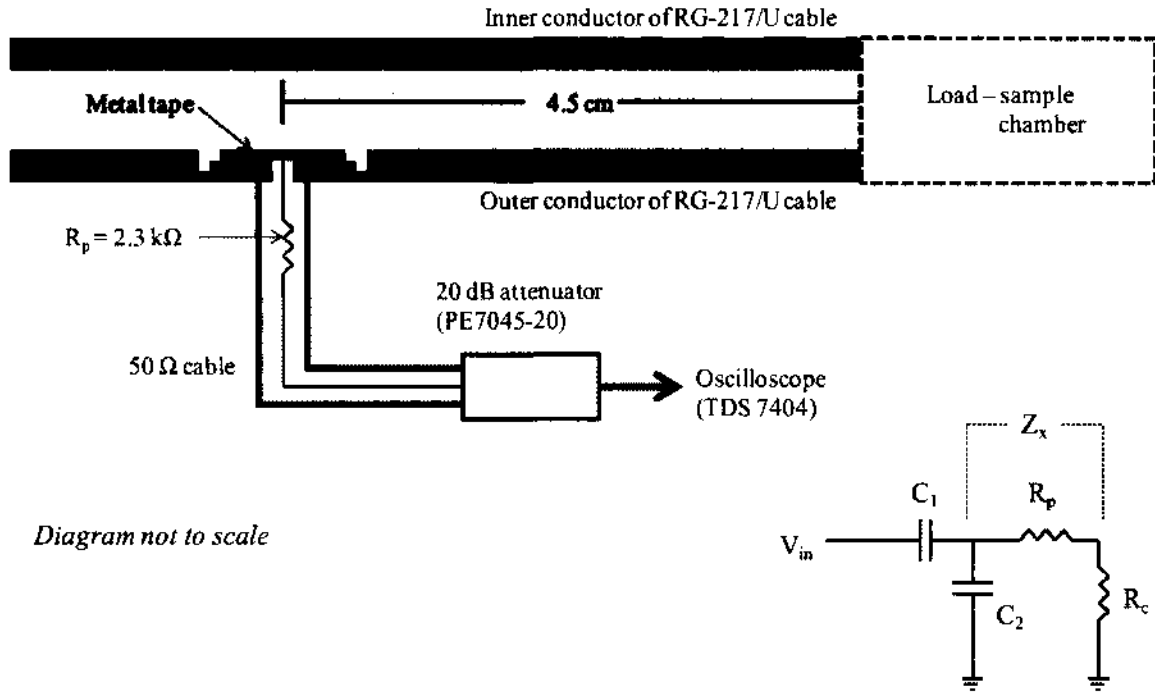


Fig. 8.1. Schematic layout of the capacitive voltage divider probe. The capacitance between the inner conductor and metal tape is denoted  $C_1$  and  $C_2$  is the capacitance between the metal tape and outer conductor. Milar tape (medium gray) was used as the insulating material for  $C_2$ .

Figure 8.1 also shows the electrical schematic of the probe (neglecting inductance). The capacitance between the inner conductor and the thin metal tape is denoted  $C_1$ , and  $C_2$  is the capacitance between the outer conductor and the metal tape. They are 0.1 pF and 6 pF, respectively. The voltage measured on the oscilloscope ( $V_s$ ) is the voltage measured across  $R_c$ , which is the impedance of the diagnostic cable (50  $\Omega$ ), and termination impedance of the oscilloscope. The damping resistor of the probe is denoted  $R_p$ . The ratio of the input voltage to the output voltage is equal to

$$\frac{V_s}{V_{in}} = [Z_x / (Z_x + Z_1)] \cdot [R_c / (R_c + R_p)] \quad 8.1$$

where  $Z_x$  is the total impedance of  $R_c$  and  $R_p$  in parallel with  $C_2$ , and  $Z_1$  is the impedance of  $C_1$ . In order to obtain an accurate voltage measurement, the time constant of the probe ( $R_p \cdot C_1$ ) must be very large compared to the pulse width (200 ps), where  $C_1$  is the series capacitance of  $C_1$  and

$C_2$ . To satisfy this condition, the resistive value of  $R_p$  was chosen to be  $2.3 \text{ k}\Omega$ , which gives a time constant of  $8.3 \text{ ns}$ . The voltage divider ratio of the probe, using (8.1), was calculated to be  $2873 (V_{in}/V_s)$ .

With  $R_p$  being much greater than  $R_c$  and  $Z_2$  (impedance of  $C_2$ ),  $Z_x$  can be approximated by  $Z_2$ . The frequency component of (8.1) would then cancel out, making the probe linear for frequencies above  $360 \text{ MHz}$  ( $3/[8.3 \text{ ns}]$ ,  $e^{-3} = 0.05$ ). The upper frequency limit of the probe is dependent upon the inductance and stray capacitance of the probe, shown in red in Fig. 8.2.

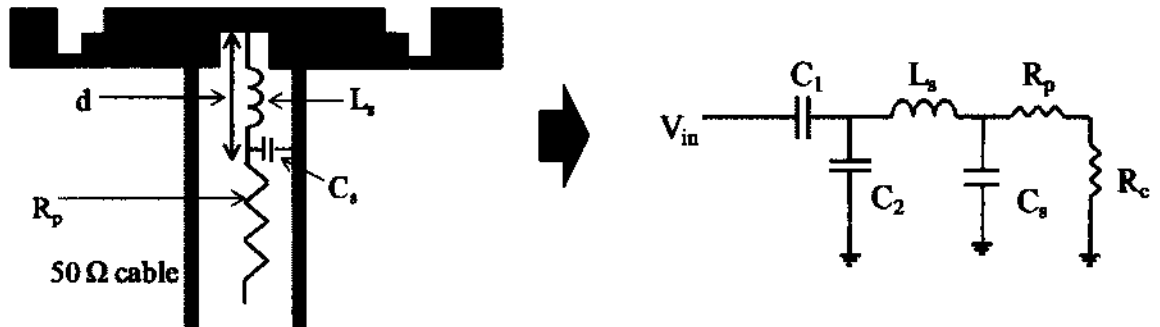


Fig. 8.2. The inductance and stray capacitance of the capacitive voltage divider probe ( $L_s$  and  $C_s$ , respectively) limit the maximum frequency at which the probe exhibits linearity. The frequency of the oscillations is defined by  $L_s$  and  $C_s$ , and the decay time of the oscillations is defined by  $R_p$  and  $C_s$ . The values of  $L_s$  and  $C_s$  were calculated using transmission line geometries.

The frequency of the oscillations is defined as:

$$f_s = 1/(2 \cdot \pi \cdot \sqrt{L_s \cdot C_s}) \quad 8.2$$

In which  $L_s$  and  $C_s$  are the inductance and stray capacitance of the probe, respectively. The inductance and capacitance comes from the conductor connecting  $R_p$  to the metal tape on the high voltage conductor. This conductor makes up a transmission line with the outer conductor of the probe. The decay constant of the oscillations is defined by:

$$\tau_{decay} = R_p \cdot C_s \quad 8.3$$

If the rise and/or fall time of the pulse is greater than the decay time of the oscillations, the oscillations will have a negligible impact on the voltage trace. If the rise and/or fall time is on the order of the decay time or shorter, the oscillations will be superimposed to the pulse, as shown in Fig. 8.3.

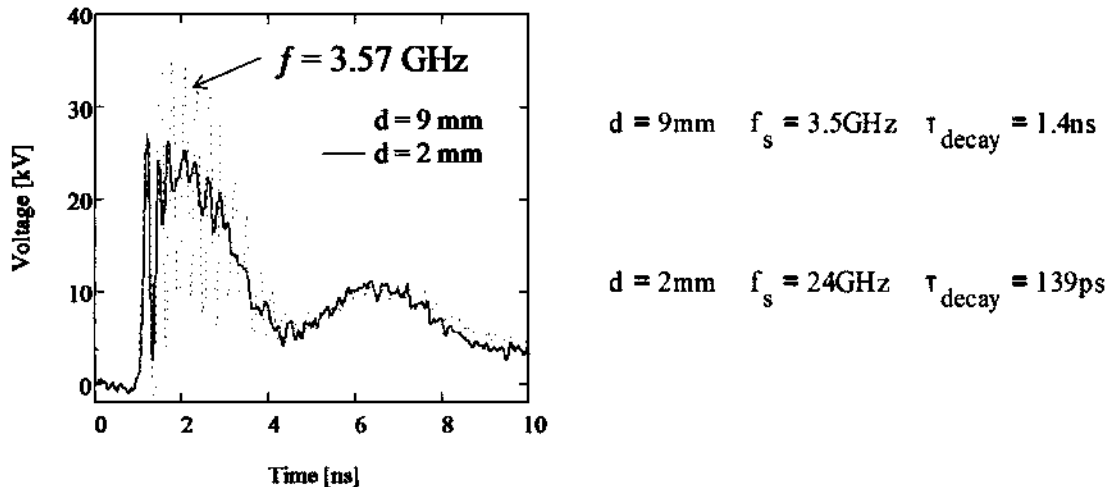


Fig. 8.3. Peaking pulse (Chapter VI) measured with a capacitive voltage divider probe in which the value of  $d$  changed from 9 mm to 2 mm, thus decreasing the decay time and increasing the frequency of the oscillation beyond the resolution of the oscilloscope (4 GHz).

The peaking pulse (see Chapter VI) has a pulse width of 150 ps, and for a connector distance of 9 mm ( $d$ ), the inductance and capacitance were high enough (0.63 pF, 3.3 nH) to induce oscillations on the pulse. The calculated frequency of 3.5 GHz is approximately the same as the measured frequency of the pulse (3.57 GHz). When the connector distance was decreased to 2 mm, the calculated decay constant decreased to 139 ps, and the oscillations increased to 24 GHz. However, the oscillations are essentially filtered out by the limited bandwidth of the oscilloscope (4 GHz).

Two techniques were used to calibrate the voltage probe. The first technique used a known pulse from a low voltage (< 1 kV) FID pulse generator FPG 5-P (FID GmbH, Germany). The voltage ratio was found to be 3220, which is about 12% higher than the calculated value.

The second technique, as described in reference [40], is based on discharging a 10 cm cable at a defined voltage into a matched load. The voltage was measured with a voltage probe (Tektronix P6015A), and the result was compared to that obtained with the capacitive voltage divider probe. This method provided a value of 3170 as the voltage divider ratio, which is close to the theoretical value. This value was used to determine the voltage.

The capacitive probe is connected to the oscilloscope by a 3 meter 50  $\Omega$  cable (RG58), and a 20 dB, SMA attenuator (PE7045-20). The frequency response of the cable and the attenuator was measured using an 8753E 3 GHz network analyzer. As the frequency was increased to 3 GHz, the change in the impedance of the system was found to be negligible.

The probe was placed as close to the load as possible, but at a distance which still allowed the incoming pulse to be separated from the reflected pulse. With the probe placed 4.5 cm from the end of the cable at the connector to the exposure chamber, and the length of the connector being 4.7 cm, at a relative permittivity of the dielectric of 2.38, the roundtrip time of the pulse from probe to exposure chamber and back is equal to 0.95 ns. This time corresponds to the temporal separation of incoming to reflected pulse.

## VIII.II REFLECTION CONCEPT OF CAPACITIVE AND RESISTIVE LOAD

The impedance of a capacitive and resistive load, which is characteristic of the sample within the exposure chamber, is given as

$$Z_{Load} = \frac{R}{1+(\omega \cdot R \cdot C)^2} - \frac{j \cdot \omega \cdot R^2 \cdot C}{1+(\omega \cdot R \cdot C)^2} \quad 8.4$$

where R and C are the resistive and capacitive components of the load, respectively. Using P-Spice (a circuit solver), a simulation of a square wave pulse with a rise and fall time of 200 ps, and a pulse width of 1 ns into a load consisting of a resistance of 80  $\Omega$  and capacitance of 5 pF is used to show the concept of a reflected pulse from a capacitive and resistive load compared to just a resistive load. The simulation result is shown in Fig. 8.4.

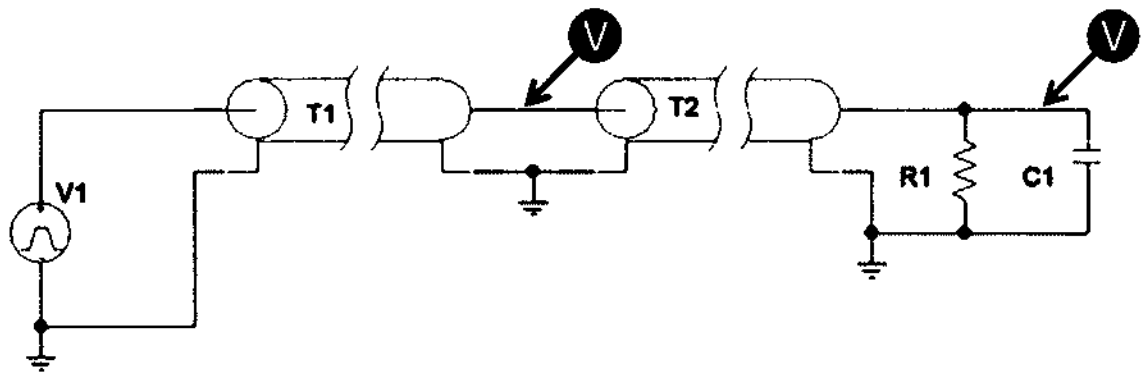
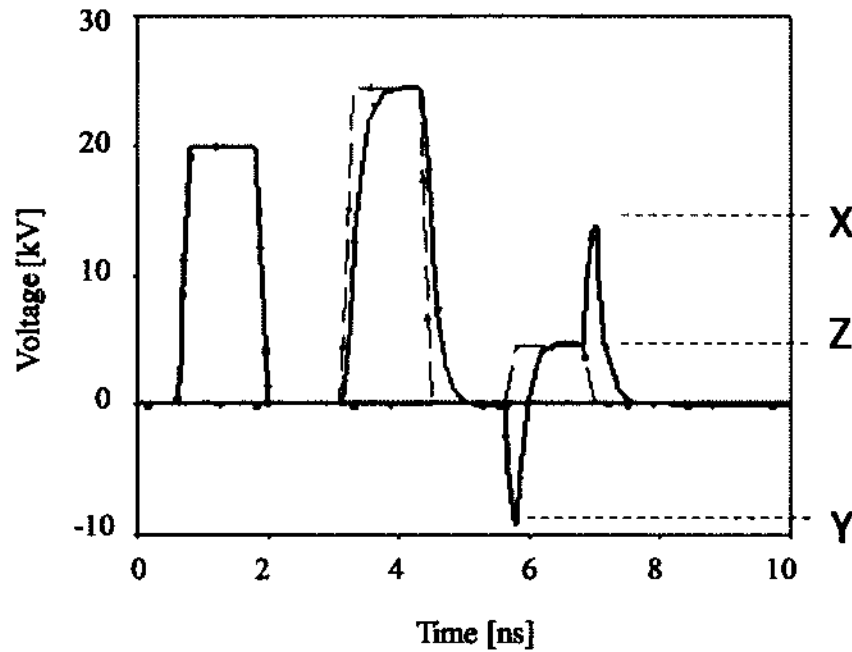


Fig. 8.4. Simulation of a pulse ( $\tau_{pw} = 1$  ns,  $\tau_{rise} = \tau_{fall} = 200$  ps) into a resistive (80 ohm) and capacitive (5 pF) load. The black trace represents the measured incoming pulse superimposed with the reflected pulse with a time difference defined by the length of the transmission line between the measured point and the load (50 cm = 5 ns). The gray traces represent the voltage measured directly at the load. The solid traces are those of a capacitive (5 pF) and resistive load, while the dotted trace is the voltage neglecting the capacitance.

The black traces represent the voltage measured in front of the load in which the length of the 50  $\Omega$  transmission line was set to be 50 cm, which equates to a 5 ns time difference between the incoming pulse and reflected pulse. The gray traces represent the voltage simulated directly at the load. The solid traces are the simulated voltage for a capacitive (5 pF) and resistive (80  $\Omega$ ) load while the dotted traces are for a purely resistive load of 80  $\Omega$ . There is a clear difference in

the reflected pulse for a load consisting of a capacitive component opposed to a purely resistive load. At the time the voltage reaches the load, the capacitor acts as a short circuit due to the high frequency component of the rise time of the pulse,  $\omega$ . Therefore, the phase is changed by  $180^\circ$ , resulting in a negative voltage. Once the voltage levels out, the impedance of the capacitance reaches 0 in which case  $Z_{load} = R$ , and the voltage rises to that of a purely resistive load. Once the fall time of the pulse reaches the load, the capacitance once again acts a short, again changing the polarity of the pulse [99]. The reflected pulse added to the incoming pulse will result in a pulse across the load, shown in gray.

The decaying portion of the reflected pulse is characterized by the time constant,  $\tau$ , which is determined by the parallel impedance of the load resistance and the impedance of the cable.

$$\tau = \frac{R \cdot Z_o}{R + Z_o} \cdot C \quad 8.5$$

The difference in the absolute value of the reflected signal for the complex load ( $X - Y$ ) is equal to the magnitude of the reflected signal for the resistive load ( $Z$ ). Using (8.6), the resistive value of the load can be determined.

$$R = Z_o \cdot \frac{V_{max} + (A - B)}{V_{max} - (A - B)} \quad 8.6$$

From these two equations, the resistive and capacitive component of the load can be determined. It should be noted that (8.4) is valid for pulse durations greater than the risetime of the pulse. If the pulse duration is equal to the risetime, as is for the pulses in this dissertation, the difference in  $X - Y$  may be decreased, suggesting a lower load voltage. This decrease is shown in Fig. 8.5 in which the simulation was repeated, but with a pulse width equal to 200 ps.

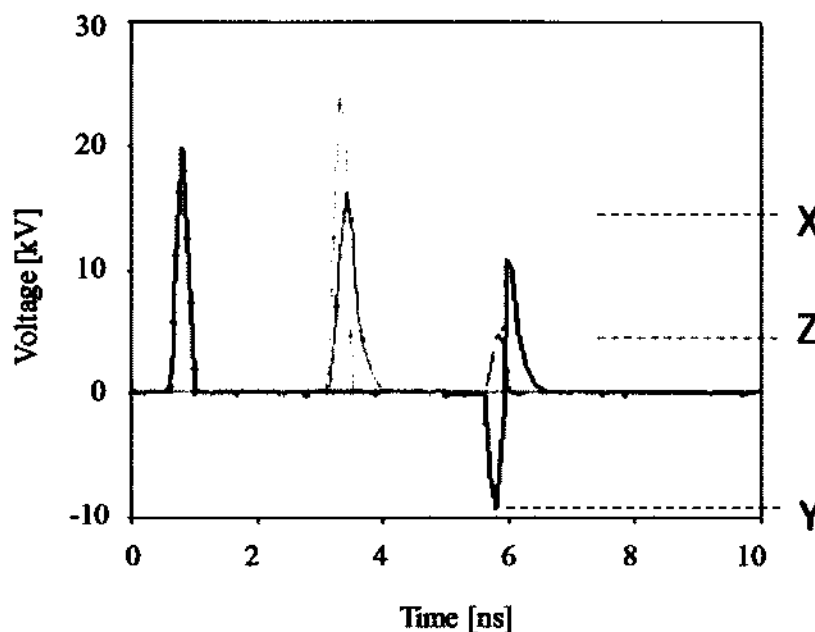


Fig. 8.5. Simulation ran with the same conditions as done in Fig. 8.2, except the pulse width was decreased from 1 ns to 200 ps. The amplitude of the pulse is decreased across the load since the pulse width is comparable to the charging time constant of the load,  $\tau = R \cdot C = 400$  ps.

Although the amplitude of the incoming pulse is the same, the magnitude of  $X - Y$  is decreased, in which case (8.4) cannot be used to accurately determine the resistance of the load,  $R$ . However, the resistive value of the sample can be easily calculated based on the geometry of the chamber and the measured conductivity of the sample, given in Table 7.1. Equation 8.5 can still be used to calculate the capacitance of the load, which will be slightly less (few percent) than the capacitance values in Table 7.1 due to the fringing effects, which is discussed in the next section.

### VIII.III DETERMINING THE VOLTAGE ACROSS THE LOAD

#### VIII.III.I Measurements

Although the resistance of the sample at room temperature ( $72.6 \Omega$ ) exceeds the impedance of the cable and waveguide ( $50 \Omega$ ), the relatively large capacitance of the exposure chamber, determined by the high permittivity of the medium, results in a reduction of the voltage

across the load,  $V(t)$ . The incoming signal,  $V_{in}(t)$ , that is seen by the load can be determined by recording the signals for the case of the load being infinite,  $V_{open}(t)$ , and zero,  $V_{short}(t)$ . With

$$V_{open}(t) = V_{in}(t) + u(\tau) \cdot V_{in}(t) \quad 8.7.a$$

and

$$V_{short}(t) = V_{in}(t) - u(\tau) \cdot V_{in}(t) \quad 8.7.b$$

where  $\tau$  is the roundtrip time of the pulse from voltage probe to load and back, and  $u(\tau)$  is a step function at the time  $\tau$ . The voltage of the incoming pulse can then be calculated as:

$$V_{in}(t) = \frac{V_{open}(t) + V_{short}(t)}{2} \quad 8.8$$

The voltage measurements are shown in Fig. 8.6. The solid black trace in Fig. 8.6(a) is the derived voltage trace ( $V_{in}(t)$ ) determined from (8.8). It shows a voltage pulse with a FWHM of 200 ps and amplitude of 15 kV, followed by a series of pulses with decreasing amplitude. The gray represents an envelope of 100 pulses. From the spread in voltage, the deviation from an average value is estimated to be approximately  $\pm 9\%$ . The reflected voltage pulse,  $V_{ref}(t)$ , can then be determined by subtracting the calculated incoming pulse voltage,  $V_{in}(t)$ , from the measured voltage,  $V_m(t)$ , with the load being the biological sample. The measured voltage 9.23 cm in front of the load, recorded at sample temperatures of 25°C and 47°C, is shown in Fig. 8.6(b). The reflected pulse, which is superimposed to the incoming pulse, is delayed by 0.95 ns with respect to the incoming pulse, in accordance with the roundtrip time of the pulse. By shifting the reflected pulse by the measured delay time toward the incoming pulse and superimposing the two pulses, the voltage across the load can be determined.



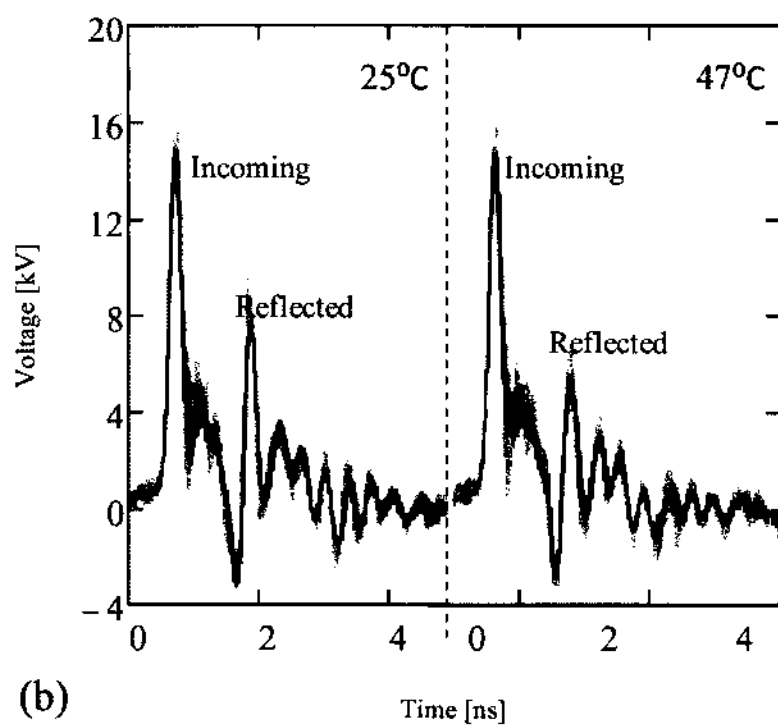
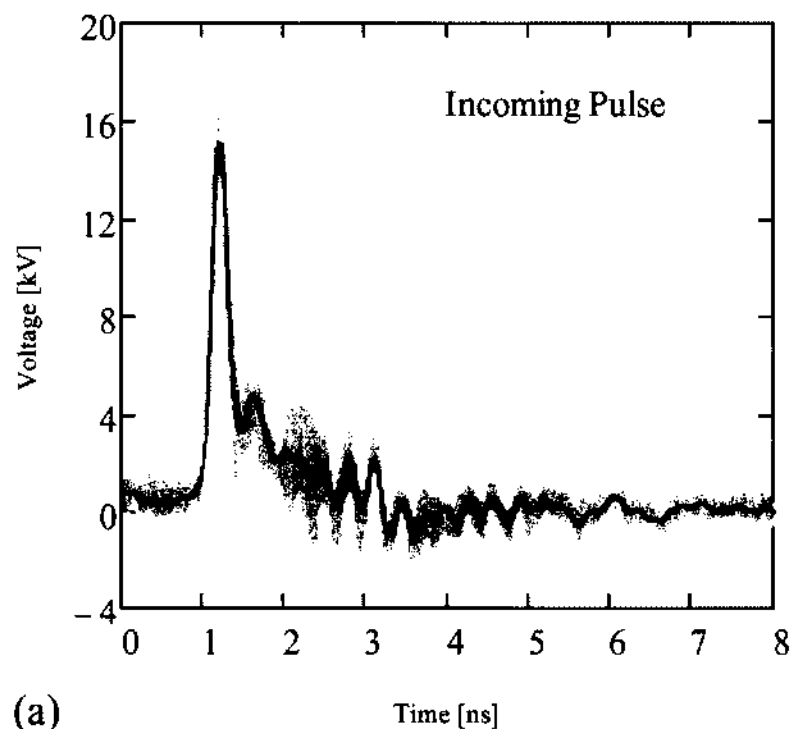


Fig. 8.6. The solid black traces are averages of 100 shots, and the gray is an envelope of 100 shots. (a) Average of 100 pulses of the incoming pulse determined by adding the pulse shapes of an open and shorted load, and dividing by two as done in (5.5). (b) The traces measured in front of the load at 25°C and 47°C showing the effects of temperatures on the reflected portion of the pulse.

The voltage across the load is shown in Fig. 8.7 for two temperatures, 25°C and 47°C. For 25°C, the amplitude of the voltage across the load is 7% lower than the amplitude of the pulse measured with the capacitive voltage divider. With increasing temperature, the difference between measured voltage and actual voltage across the load increases to 11% for 37°C. For 42°C and 47°C, the difference in amplitudes increased to 12% and 13%, respectively. The decrease in amplitude with an increase in temperature is a result of the decrease in the overall impedance of the load with increasing temperature. As the temperature of the sample increases, the conductivity increases more strongly compared to the inverse of the permittivity, causing a larger reduction in resistance which more than compensates for the increase in reactance.

During experiments, the voltage used to determine the voltage across the load will be the voltage measured in front of the load, as shown in Fig. 8.6(b), which consists of both the incoming pulse (Fig. 8.6(a)) and the reflected signal (Fig. 8.8). The values in Table 8.1 will be used to determine the magnitude of the pulse across the load in relationship to the measured pulse in front of the load.

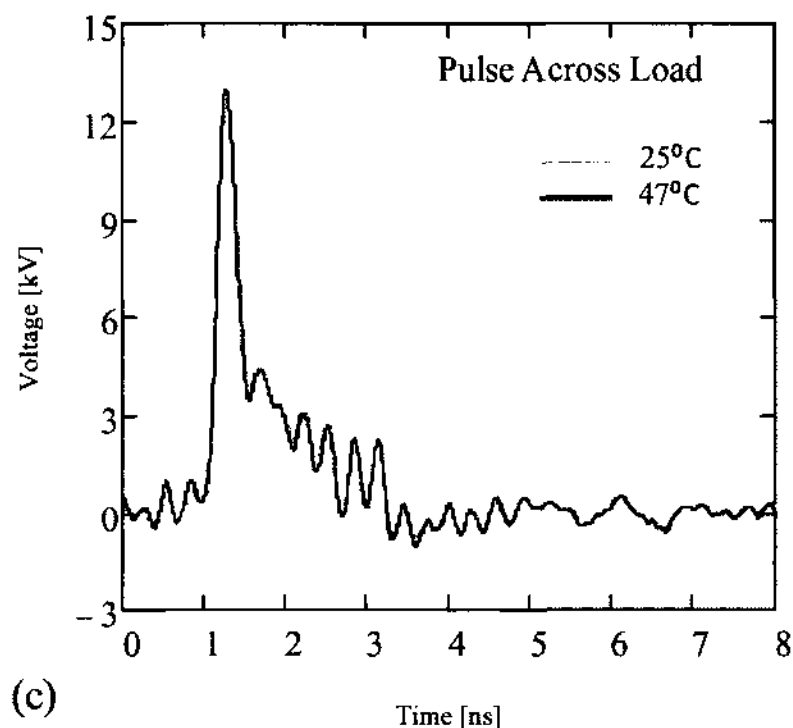


Fig. 8.7. The voltage across the load determined by superimposing the reflected pulse to the incoming pulse, in which the reflected pulse was shifted to the left by 0.95 ns. The gray trace represents the voltage across the load for a sample temperature of 25°C, and the black trace is for 47°C.

Temperature [°C]	Decrease in Amplitude [%]
25	7
37	11
42	12
47	13

Table 8.1. The amplitude of the voltage across the load will be determined by decreasing the amplitude of the voltage measured with the voltage probe in front of the load by the percentage given at its respected temperature.

### VIII.III.II Voltage Simulations Using PSpice

The validity of the resistive and capacitive values of the load obtained through TDR measurements (values taken from Table 7.1) was tested through modeling of the circuit with PSpice. The circuit was the same as the circuit used in Fig. 8.2, except the length of the transmission line, T2, between the load and the voltage probe was 9.23 cm, equating to a delay of 0.95 ns. The measured incoming pulse in Fig. 8.6(a) was used as the incoming pulse, V1, in the simulation. The resistive and capacitive values of the load, with respect to temperature, were taken from Table 7.1. The simulated voltages were not in agreement with the measured voltage. The magnitude of the simulated reflected voltage was 3 kV higher than the measured reflected voltage, and the simulated voltage across the load was 3 kV lower than the experimentally determined voltage across the load. However, as stated in Chapter VII, due to the fringing fields of the gap, the actual capacitance of the load is 7% lower than those listed in Table 7.1. Therefore, rather than using the TDR values, the capacitance was determined by measuring the decay constant of the reflected pulse (Fig. 8.8), and solving for C using (8.5).

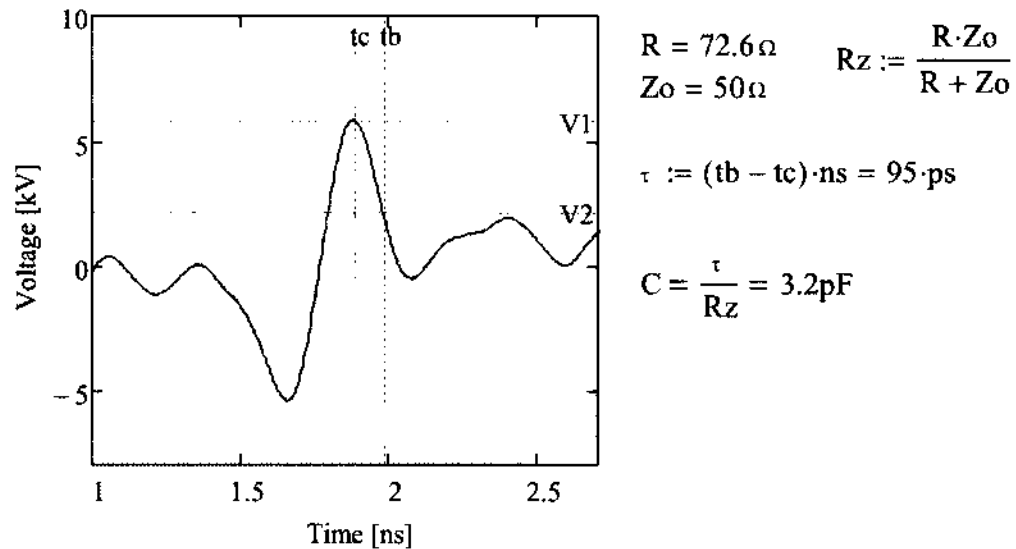
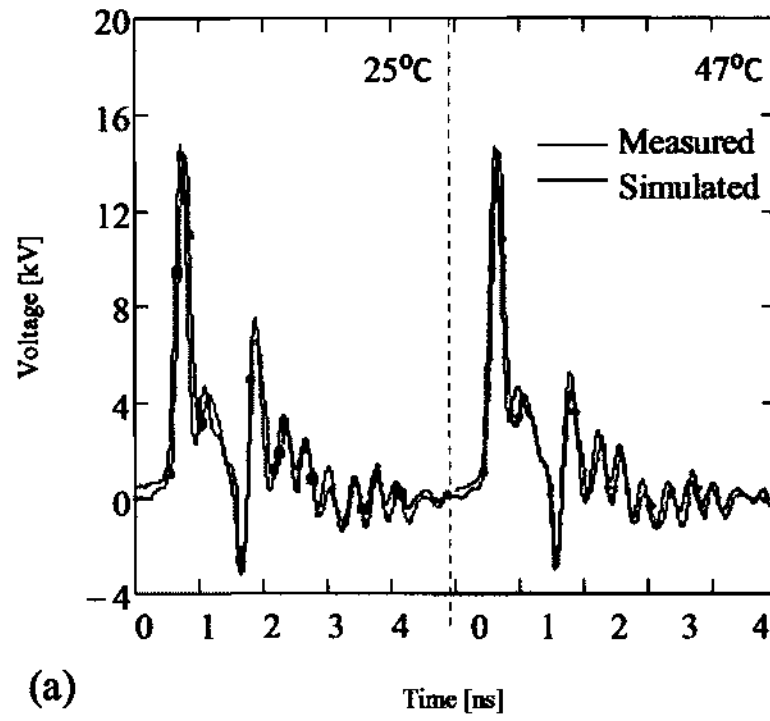


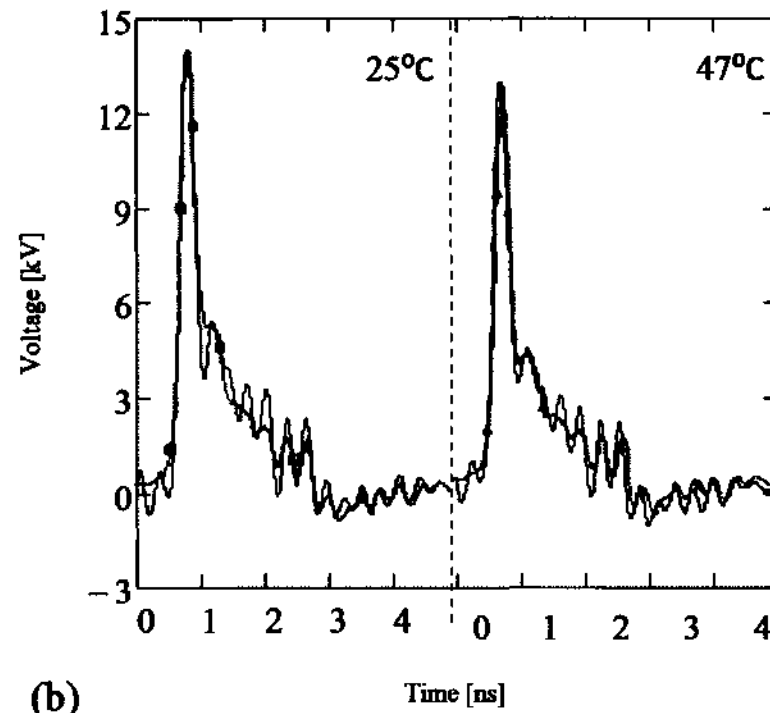
Fig. 8.8. Reflected pulse determined by separating the input voltage from the voltage measured across the load. The capacitance, determined from the decay time of the pulse, was found to be 3.2 pF.

At 25°C, the measured decay time is approximately 95 ps, and with a resistance of 72.6  $\Omega$  (Table 7.1), the calculated capacitance is 3.2 pF compared to 7 pF (calculated capacitance ignoring fringing effects using permittivity value in Table 7.1). The same technique used for a temperature of 47°C gave a capacitance of 2.6 pF, compared to calculated capacitance of 5.7 pF. The ratio of the capacitance at 47°C and 25°C is equal to the ratio of the permittivity measured at 47°C and 25°C, which confirms the validity of the ratio of the measured permittivities in Table 7.1. The values of the capacitance, obtained from the reflected pulse, are 45% of calculated capacitance. The decrease in capacitance due to the fringing effect (see Chapter VII) only accounted for a 7%. If the decrease in capacitance was attributed to an error in the TDR analysis of the medium, the permittivity of the medium at room temperature, to account for a 3.2 pF value, would be approximately 35. Such an error is very unlikely since there are no references which state the permittivity of growth medium of cells in this range at room temperature. The decrease in capacitance may come from other effects such as ferroelectric losses, dielectric conduction, and/or leakage current [100].

The comparison of the measured voltage traces to the simulated traces at 25°C and 47°C, using the capacitance determined from the reflected signal, are shown in Fig. 8.9. The measured and simulated traces are shown in black and gray, respectively. In Fig. 8.9(a) the voltage measured in front of the load is compared to the simulated voltage in front of the load. As with the measured traces, the simulation shows a decrease in the positive amplitude of the reflected pulse with an increase in temperature. Fig. 8.9(b) compares the simulated voltage at the load compared to the determined voltage at the load from the measured traces in the previous section. The simulation is in agreement with the measured traces, which confirms the validity of the measured resistive values of the load determined from TDR, and the capacitive values determined from the reflected signal.



(a)



(b)

Fig. 8.9. Comparison of the simulated voltage (gray trace) and the measured voltage (black trace) in front of the load (a) and at the load (b) for a sample temperature of 25°C and 47°C.

## CHAPTER IX

### TEMPERATURE MEASUREMENTS

The temperature of the sample could not be measured directly, but indirectly by measuring the temperature of the electrode directly over the sample. It is imperative for these experiments that the temperature of the sample is well recorded and remains constant during pulsing conditions. Therefore it is important to know the increase in temperature of the sample due to applied pulsed electric fields, which have been known to increase the temperature from a few degrees to over 20 degrees in previous experiments [2, 45, 101]. The increase in temperature due to pulsing, depending on the application, may be a desired or an undesired effect owing to the fact the temperature alone has an effect on the cells. The effect that the duration and the change in temperature above the physiological temperature (37°C) has on cells is known as hyperthermia, and has been studied rigorously [102-106].

This chapter is divided into three sections; in the first section, the effects of pulsed electric fields on the sample temperature are discussed. This section will also introduce the concept of the leveling temperature which is the maximum attainable temperature as a result of pulsed electric fields, which is independent on the number of pulses. The second section will cover the temperature increase of the sample for the conditions used in this dissertation, as well as the length of time needed for the sample temperature to equilibrium with the exposure chamber. The third section describes the setup for externally controlling and measuring the temperature of the sample.

#### IX.1 TEMPERATURE INCREASE DUE TO PULSING

Applying pulsed electric fields to a liquid solution of biological cells will cause the sample temperature to increase by  $dT$  with each pulse.

$$dT = \frac{V^2}{Z \cdot m \cdot c} \tau \quad 9.1$$

In (9.1), the voltage and duration of the pulsed are represented by  $V$  and  $\tau$ , respectively. The mass, specific heat, and impedance of the sample is represented by  $m$ ,  $c$ , and  $Z$ , respectively. A majority of the heat created from the pulses will be dissipated into the surface of the electrodes in contact with the sample, while a negligible amount will be dissipated into the dielectric walls surrounding the sample due to the large difference in the thermal conductivities. The duration of the pulse defines the time it takes the temperature to increase by  $dT$ , while the thermal properties of the sample determine the decay constant in which the temperature decreases. Since the risetime of the pulse is less than 1 ns, and the thermal decay constant is on the order of seconds, it is assumed the increase in temperature due to pulsing occurs instantly compared to the decay time.

In order to separate the effects of temperature and pulsing on cells, the additive effect of  $dT$  must be kept to a minimum for multiple pulses. The temperature response of a sample exposed to one pulse, under the assumptions that 100% of the heat is conducted through the electrodes, can be determined with Newton's Law of Cooling. This assumption is valid since a majority of the surface area of the sample is exposed to the electrode opposed to the insulator ( $36 \text{ mm}^2$  vs  $27 \text{ mm}^2$ ), and the thermal conductivity of stainless steel ( $16 \text{ W/m}\cdot\text{K}$ ) is approximately two orders of magnitude higher than the thermal conductivity of polyethylene ( $0.2 \text{ W/m}\cdot\text{K}$ ). Newton's Law of Cooling is calculated as [107]:

$$T(t) = T_{final} + (dT + T_0 - T_{final}) \cdot e^{-t \cdot \sigma / c \cdot m} \quad 9.2$$

The mass, specific heat, and thermal conductance of the sample is represented by  $m$ ,  $c$ , and  $\sigma$ , respectively. The thermal conductance is the thermal conductivity of the sample (value for water) multiplied by the cross sectional area of the electrode, divided by half the gap distance (sample is being heated by both electrodes). The specific heat was chosen to be that of water. These values make up a thermal decay constant ( $\tau_{th} = c \cdot m / \sigma$ ), which was calculated to be 4.75 s for the exposure chamber used in this dissertation. The temperature of the exposure chamber, which is



externally controlled, is denoted  $T_o$ , and the change in temperature as a result of one pulse is denoted  $dT$ . The final temperature of the sample depends on the geometry and specific heat of the material within the sample chamber and is approximated by

$$T_{final} = \frac{C_{ss} \cdot T_o + C_{sample} \cdot (T_o + dT)}{C_{ss} + C_{sample}} \quad 9.3$$

in which  $C_{ss}$  and  $C_{sample}$  are the specific heats of the conducting material of the electrodes (stainless steel = ss) and the sample, respectively. Due to the bulkiness of the exposure chamber ( $C_{ss} \gg C_{sample}$ ), it can be assumed that the final temperature is equal to the initial temperature of the chamber,  $T_o$ , which simplifies (9.2). The increase in temperature as a result of a pulse is assumed instantaneous while the drop in temperature depends on thermal decay constant,  $\tau_{th}$ .

With multiple pulses, the increase in temperature of the sample is proportional to the frequency of the applied pulses and the thermal decay time of the temperature of the sample within the chamber. The temperature of the sample will increase as a result of the pulsed electric fields until Joule heating and thermal losses (mainly due to heat conduction) balance out. This equilibrium temperature is known as the leveling temperature, which is derived from Newton's law of cooling:

$$T_{level} = T_o + \frac{dT}{1 - e^{-1/\tau_{th} \cdot f_r}} \quad 9.4$$

The number of pulses per second (pulse rate) is represented by  $f_r$ , and the thermal decay constant is represented by  $\tau_{th}$ . The concept of the leveling temperature is shown in Fig. 9.1, which shows the temperature profile of a sample exposed to 20 pulses.

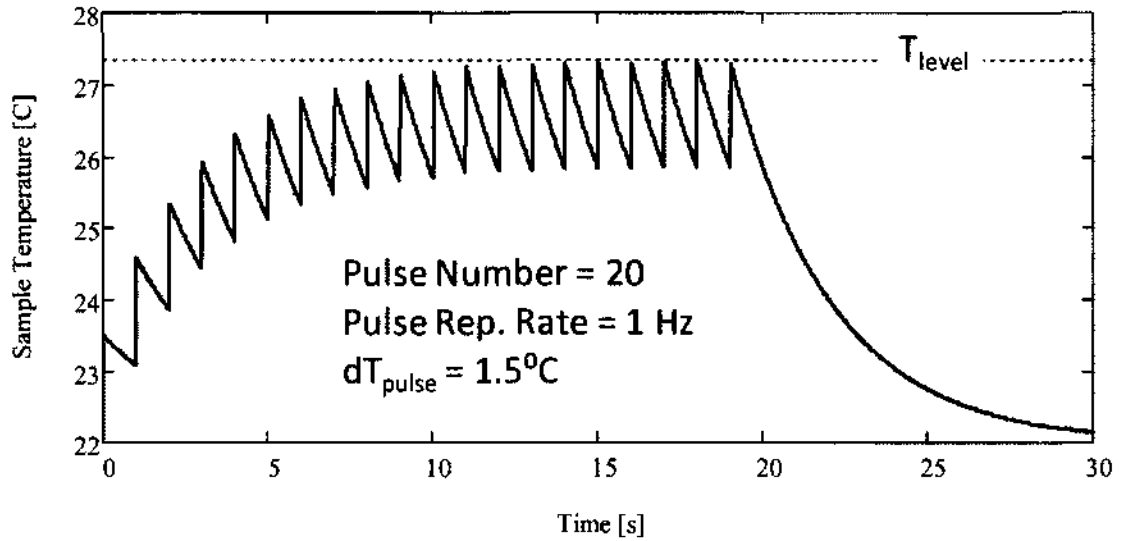


Fig. 9.1. Concept of the leveling temperature ( $T_{level}$ ) of a sample due to pulsed electric fields. The temperature of the sample will be increased by  $dT$  for each pulse. As the temperature of the sample is increased, the decay of the temperature increases until the loss of temperature between pulses is equal to the change in temperature due to one pulse.

The gray dotted line is the leveling temperature. Once the temperature of the sample reaches the leveling temperature, the temperature will not increase with continued pulsing. Therefore, the leveling temperature is independent of the number of pulses, and hence, independent of the total electrical energy density. Equation (9.4) can be used to determine the maximum repetition frequency to keep the leveling temperature below a desired value.

## IX.II THERMAL DECAY MEASUREMENT

In order to determine the leveling temperature for the experimental conditions in this dissertation, the thermal decay constant was measured with an optical temperature sensor, with a diameter of 30  $\mu m$  (FISO: FOT-HERO). This measurement was achieved by placing a sample, heated to 50°C, into the chamber ( $T_o = 23^{\circ}C$ ) and placing the top electrode which held the sensor (as depicted in Fig. 9.2) over the sample to measure the temperature decay. The constant is the same whether the temperature is increasing or decreasing. By the time the probe was placed into the sample, the temperature had already dropped to 40°C. From the measured thermal decay, it

was determined that 1 minute was sufficient time between the placement of the sample in the chamber and the start of the pulsing to allow the temperature of the sample to reach the ambient temperature.

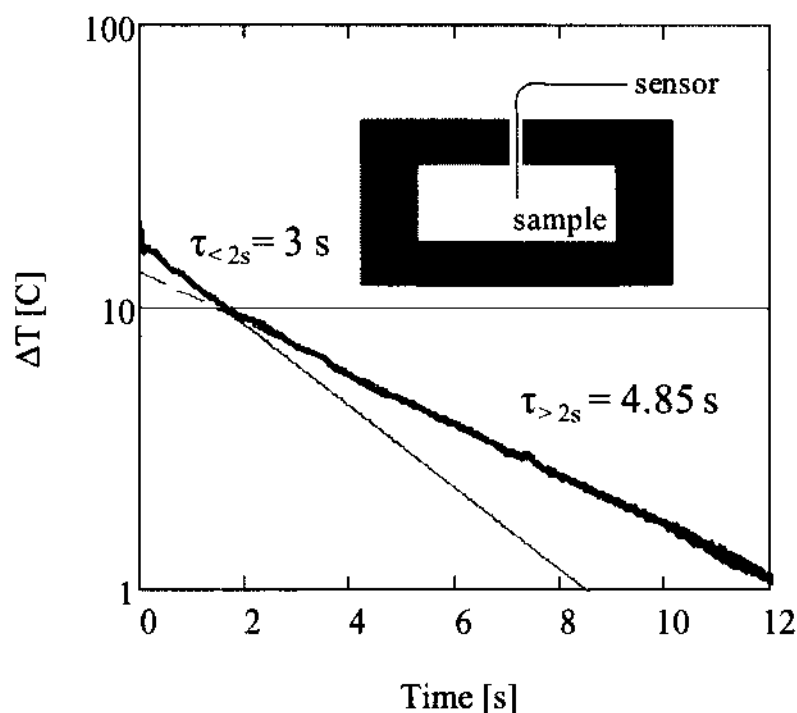


Fig. 9.2. The measured temperature decay of the sample chamber (black) compared to the calculated temperature decay (gray).

The initial temperature decay has a thermal constant of 3 s, while the thermal decay time, constant after 2 seconds, is equal to 4.85 seconds, which is in reasonable agreement with the calculated value, 4.75 seconds. The initial fast decay, prior to 2 seconds, is determined by the initial rapid decay of the temperature at the electrodes, which causes the build-up of a temperature gradient from the center of the sample to the electrodes, as shown in Fig. 9.3. As the temperature at the edge of the electrode facing the sample quickly decreases, the temperature gradient decreases within the electrode and increases within the sample. The sample has a lower thermal conductance, which accounts for a slower decay. Newton's Law of Cooling does not take into

account the thermal properties of the electrodes in that it assumes the electrodes are a perfect heat sink. The conditions for Newton's Law of cooling are observed in Fig. 9.2 after 2 seconds in which the temperature decay within the sample is mainly a function of the temperature gradient within the sample, as illustrated in Fig. 9.3 for  $t > 2$  s.

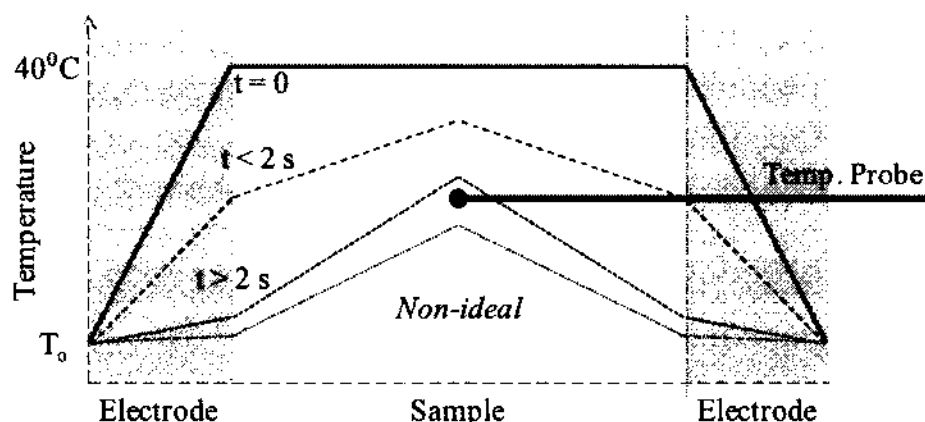


Fig. 9.3. At  $t = 0$ , the temperature of the sample is at  $T_1$ , and the temperature of the electrodes is at  $T_0$ , which creates a large temperature gradient at the electrode-sample interface. Past 2 seconds, the temperature gradient in the electrodes as decreased, leaving a larger gradient in the sample.

The thermal decay time constant,  $\tau_{th}$ , for pulses with repetition rates exceeding  $f = 0.5$  pps (1/2s), is determined by the initial, rapid decay in temperature. With a pulse repetition rate of 10 pps, the relevant time constant is 3 s. The energy of a single, 200 ps pulse of amplitude 30 kV into a  $72 \Omega$  load is equal to 2.5 mJ, which equates to a temperature increase of  $0.018^\circ\text{C}$  per pulse ( $dT$ ). The leveling temperature ( $T_{level}$ ) was calculated to be  $23.55^\circ\text{C}$ , with an initial temperature ( $T_i$ ) of  $23^\circ\text{C}$ , which equates to a temperature increase of  $0.55^\circ\text{C}$ . It is therefore safe to assume that Joule heating under the conditions of our experiment can be neglected compared to heating with the external source. The calculated temperature trace for a  $dT$  of  $0.018^\circ\text{C}$ , thermal constant of 3 s, 900 pulses, and 10 pps is shown in Fig. 9.4.

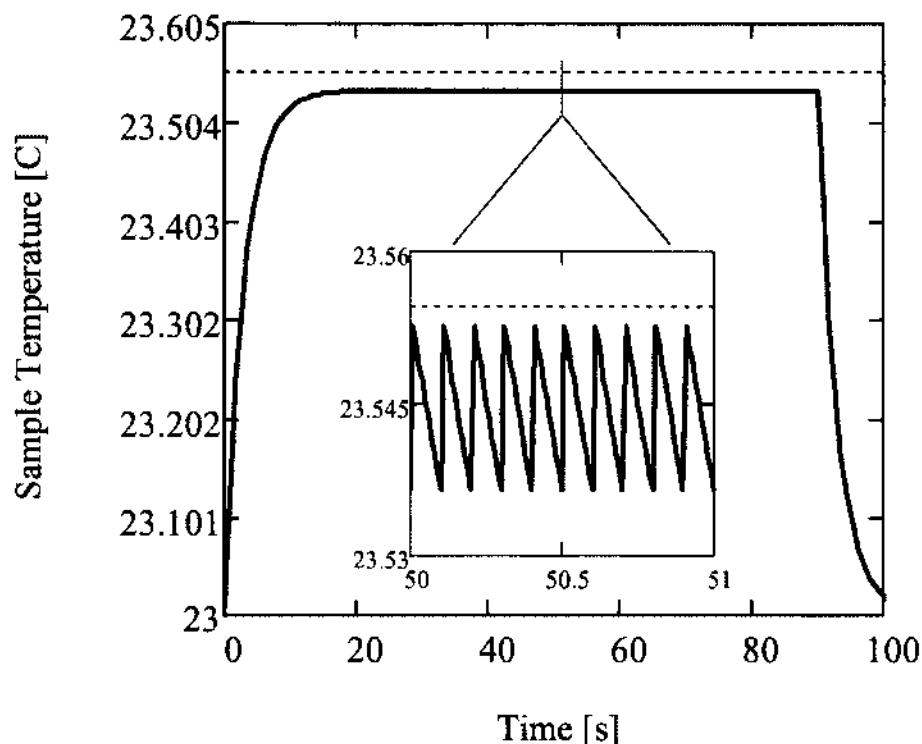
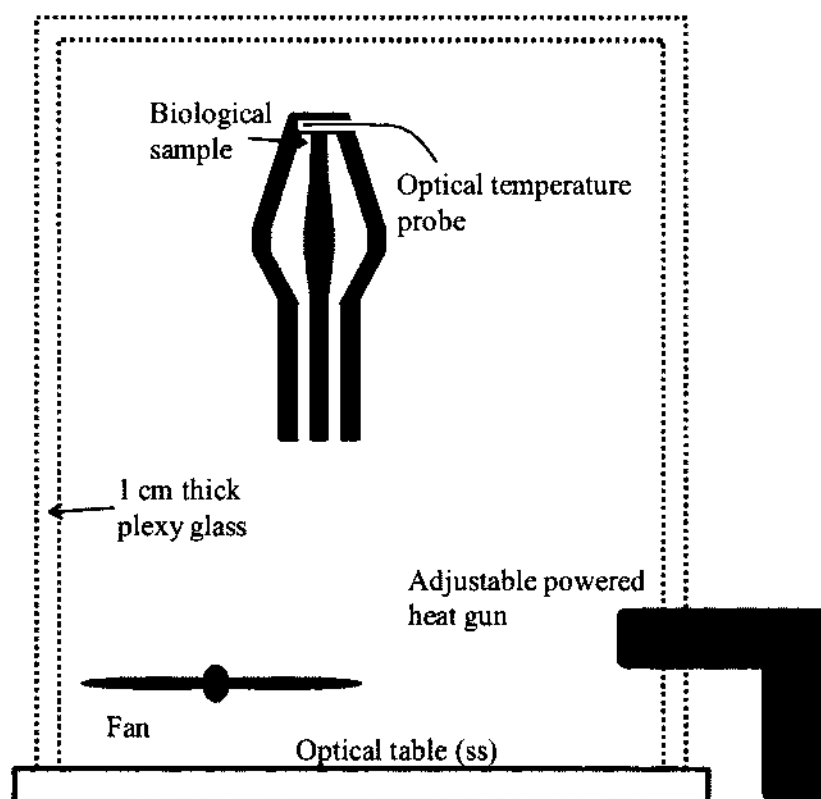


Fig. 9.4. Calculated temperature diagram for cells within the exposure chamber exposed to a voltage of 30 kV, 200 ps, at a pulse repetition rate of 10 Hz. The diagram suggests the temperature increase due to pulsing will not be raised by more than 1°C.

The leveling temperature (gray dotted line) is reached after approximately 250 pulses. The insert of Fig. 9.4 shows a higher temporal resolution of the temperature with respect to each pulse. The actual experimental conditions (20 kV, 200 ps, 7 pps) would result in even less increase in temperature with applied pulses.

### IX.III TEMPERATURE CONTROL

In order to heat the sample externally, the exposure chamber was placed into an insulated box (1 m x 0.5 m x 0.5 m) whose interior was heated with a heat gun, as depicted in Fig. 9.5.



*Diagram not to scale*

Fig. 9.5. Conceptual layout of the experimental setup. The sample chamber was placed in a box made of plexilass, which was heated to the desired temperature with a heat gun and a fan. The temperature of the sample was measured indirectly by placing the temperature probe in a hole of the cap 1 mm above the sample.

Once the interior of the box reached the desired temperature, the power of the heat gun was decreased in order to maintain the temperature. The sample was then placed within the chamber and given 1 minute to reach the ambient temperature. Based on the temperature studies described in the previous section, this time is more than sufficient for the sample to achieve temperature equilibrium with its environment.

Due to the fact that there was no access through the ground electrode, the temperature of the sample was not measured directly, but indirectly, by measuring the temperature of the conductive cap placed over the sample with a fiber optic temperature sensor (Neoptix, T1S-11854A).

## **CHAPTER X**

### **BIOLOGICAL PROTOCOLS AND PROCEDURES**

#### **X.I CELL CULTURE AND TRYPAN BLUE EXCLUSION ASSAY**

The mouse hepatoma epithelial cell line (Hepa 1-6) was obtained from American Type Culture Collection (ATCC, Manassas, VA) and cultured in complete medium containing Dulbecco's Modification of Eagle's Medium (Cellgro, Fisher Scientific cat#10-013-CV) supplemented with 10% FBS (Cellgro, Fisher Scientific cat#35-015-CV). The passage number of the cell line used in the experiments did not exceed 20.

To prepare for the experiment, Hepa 1-6 cells at 80-90% confluency in tissue culture flasks were washed with PBS (Cellgro, Fisher Scientific cat#21-040-CV) at room temperature and treated with trypsin-EDTA (Cellgro, Fisher Scientific cat#25-053-C1) at 37°C for 5 minutes. The trypsinized cell suspension was neutralized with a 4 times equivalent volume of complete medium and centrifuged at 100 g for 10 minutes, followed by the removal of the supernatant. The cells were resuspended in complete medium and counted by trypan blue exclusion assay on the hemocytometer (Fisher Scientific cat#02-671-54) under the microscope with the final concentration of 0.2% trypan blue. The use of a proper volume of resuspension medium ensures that every 16-square area on the hemocytometer contains 50-100 cells (200-400 cells in 4 areas). Cell viability, which equals the percentage of live cells among the total number of cells, was calculated. Then the required number of cells was transferred to a new tube, centrifuged and resuspended in an appropriate volume of complete medium to make a final concentration of 6 million cells per ml for downstream experiments.

The trypan blue exclusion assay was used as an indicator of plasma membrane integrity and of cell viability after pulse exposure. The cell solution was mixed with trypan blue at a 1:1

ratio and was left for 1 minute to allow enough time for dead or dying cells to absorb the dye. The cells were hand counted and the cell count ranged between 300 -500 cells for each data point.

## **X.II EXPERIMENTAL PROTOCOL**

Before experiments, a heat gun was used to raise the temperature of the chamber for approximately 30 minutes to the desired temperature (37°C, 42°C or 47°C). Once the temperature was reached, the power of the heat gun was reduced to maintain the temperature. Thirty-five  $\mu\text{L}$  of the sample was placed into the chamber for 1 minute to allow the temperature of the sample to equilibrate to the ambient temperature of the chamber. Pulses were applied at a rate of 7 - 8 pps, and 30  $\mu\text{L}$  of the sample was removed from the chamber and placed into a vial with 40  $\mu\text{L}$  of the growth media (same medium used for culturing), thus decreasing the cell concentration to  $2.57 \cdot 10^6$  cells/ml. The control sample underwent the same procedure, but without applying the pulsed electric fields (sham). The vials containing the samples were covered with mylar tape, and placed in an incubator for 4 hours at 37°C. After 4 hours, the vials were removed from the incubator, and the samples were examined by trypan blue uptake at a 1:1 ratio.

For the membrane permeability experiments, 17  $\mu\text{L}$  of trypan blue were mixed with 18  $\mu\text{L}$  of sample and placed into the exposure chamber to undergo the experimental conditions. After exposure, 30  $\mu\text{L}$  of the mixed sample was placed in 40  $\mu\text{L}$  of solution containing 20  $\mu\text{L}$  of trypan blue and 20  $\mu\text{L}$  of culture medium. Cells were examined for trypan blue uptake immediately afterwards (< 3 minutes).

## **X.III MEASUREMENT OF TEMPERATURE DEPENDENCE ON TRYPAN BLUE UPTAKE**

In order to determine the effect of temperature alone, without pulsing, experiments were performed using a waterbath which could be heated quickly, i.e., in about one minute. One



hundred fifteen microliters of Hepa 1-6 cells at a concentration of 6 million cells/ml were placed at the bottom of 1.5 ml polypropylene centrifuge tubes, which were dipped in a water bath (GCA Precision, model #Thelco 183) for 1, 2, 5, 10, 15, 30 and 105 minutes at 42°C, 47°C or 52°C. The temperature of the water bath was measured using a standard mercury thermometer. The temperature in the centrifuge tubes was monitored using an optical temperature probe. The time it took for the temperature to reach 47°C was approximately 1 minute, longer than for the heating method described above. After water bath incubation, the cell tubes were immediately transferred to a 37°C tissue culture incubator (NUAIRE, model #NU-8700) and incubated or “recovered” for 4 more hours. The cells were then assessed by the trypan blue exclusion assay as described earlier, except the cells were diluted in 0.4% trypan blue solution at a 1:8 ratio.

## CHAPTER XI

### EXPERIMENTAL RESULTS

#### XI.1 EFFECT OF TEMPERATURE WITHOUT PULSE APPLICATION

In order to determine the effect of temperature alone, i.e., without pulsing, experiments were performed using a waterbath. The cells in the waterbath were heated within times similar to those used in the heating system where a heat gun was used to increase the ambient temperature (about 1 minute for the temperature of the sample to reach 47°C)). Three independent experiments were conducted for temperatures of 42°C, 47°C and 52°C, and the results are shown in Fig. 11.1.

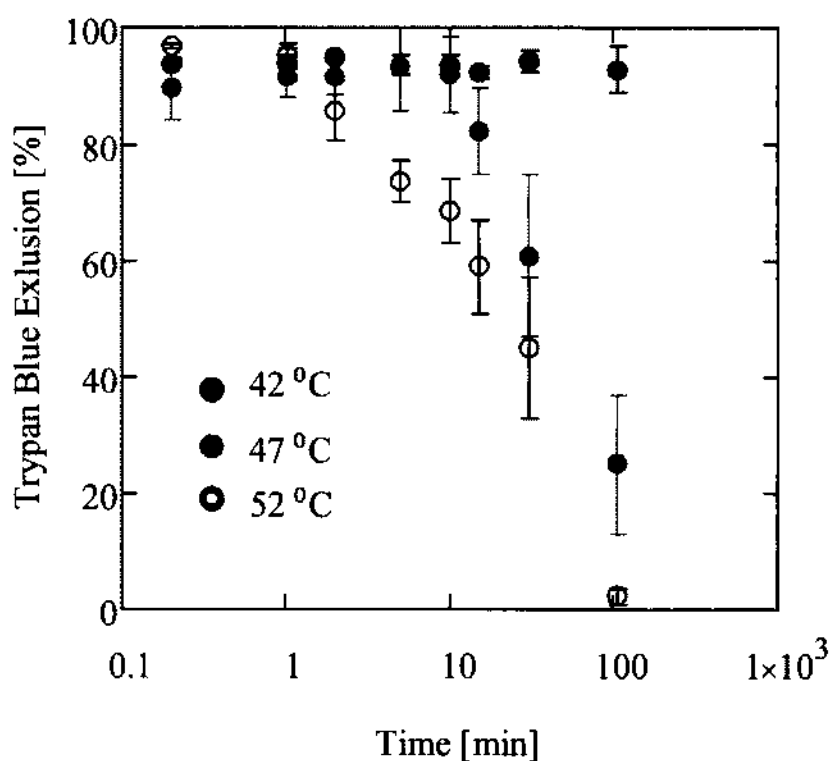


Fig. 11.1. Trypan blue exclusion versus exposure time of cells placed in a water bath of 42°C, 47°C and 52°C.

Cells exposed to temperatures of 42°C experience negligible cell death up to 105 minutes. Cells exposed to temperatures of 47°C begin to die rapidly after 15 minutes, which is almost three times as long as the time to which the cells were exposed for the pulse experiments. Cells exposed to 52°C show a 10% decrease in viability after 2 minutes. In the pulse experiments, the longest period of time that the cells encountered the highest temperature used, 47°C, was less than 10 minutes (one minute to heat the sample plus slightly more than 8 minutes to be exposed to 4,500 pulses at a repetition rate of 9 pps at 52 kV/cm). Based on the results in Fig. 11.1, the increase in temperature alone does not affect the viability of the cells for the temperatures and durations used in the pulsing experiments.

#### **XLII TRYPAN BLUE EXCLUSION FOUR HOURS AFTER EXPOSURE TO PEF**

In order to determine the effects of temperature in conjunction with pulsing, experiments were performed where 1,000 and 2,000 200-ps long pulses were applied to the sample at various temperatures. The temperatures of the sample during pulsing and without pulsing (sham) were 25°C, 37°C, 42°C and 47°C. Two types of controls were taken: an unpulsed sample at room temperature (25°C) and an unpulsed sample at each elevated temperature. Based on the results in Fig. 11.1, there should be a negligible difference in the two types of controls.

Four hours after experimental conditions were applied, the trypan blue assay was performed, the uptake of which is a marker for cell death [1]. The applied electric field was  $90 \pm 7$  kV/cm. Due to the unmatched impedance at the load, the electric field across the sample was decreased to  $84 \pm 7$  kV/cm (room temperature). Due to the changes in the electrical properties of the load with temperature, the actual electric field strength for higher temperatures was less than 84 kV/cm (Chapter VIII). For 25°C the electric field value was 84 kV/cm, 80 kV/cm for 37°C, 79 kV/cm for 42°C and 78 kV/cm for 47°C. The results are shown in Fig. 11.2.

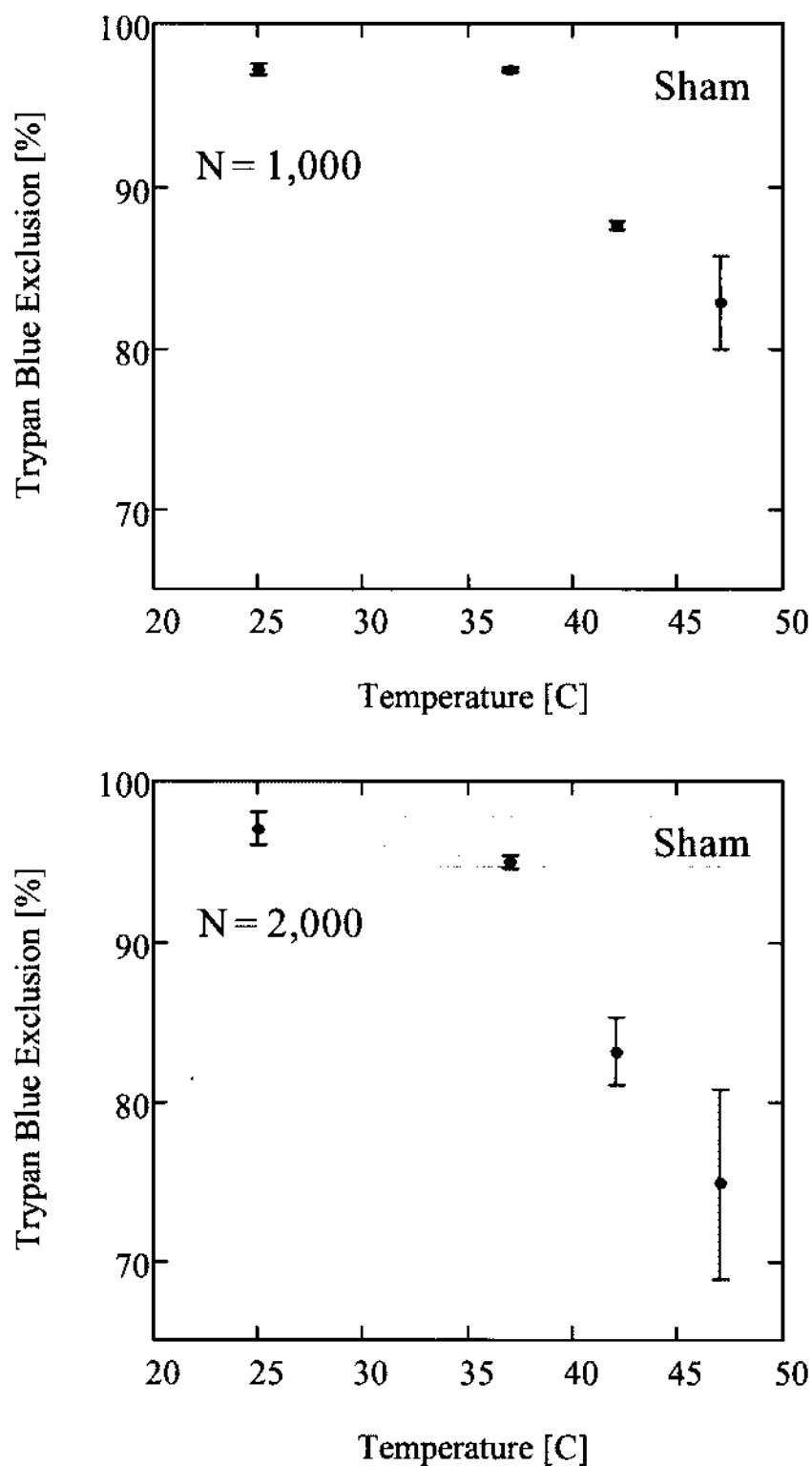


Fig. 11.2. Trypan blue exclusion 4 hours after experimental exposure to 1,000 and 2,000, 200 ps long pulses, dependent on temperature. The measured electric field at room temperature was kept constant at 84 kV/cm, but decreased to 78 kV/cm at 47°C. The data is based on 3 to 5 experiments each (n=3-5).

The sham is the combination of all the controls performed through the experiment. In each case, no distinguishable difference was evident in the exclusion of trypan blue for cells exposed to 25°C up to 47°C without applying pulsed electric fields, as expected from the studies where the temperature effect without pulsing was explored (Fig. 11.1). For both 1,000 and 2,000 pulses, there is a negligible difference in the exclusion of trypan blue from the sham and cells exposed to 25°C and 37°C during pulsing. In Fig. 13.2(a), the cell concentration which shows trypan blue exclusion decreases to 87.7% and 82.8% when the temperature of the sample is increased to 42°C and 47°C, respectively. The same trend is seen when 2,000 pulses are applied, but to a higher degree (83% for 42°C and 75% for 47°C).

### **XLIII TRYPAN BLUE EXCLUSION IN TERMS OF ENERGY DENSITY**

The shape of the voltage pulse (Chapter VIII) can be approximated by a Gaussian function, in which the standard deviation ( $\phi$ ) is approximately one half of the pulse width, and  $V_0$  is the amplitude of the pulse.

$$V(t) = V_0 e^{-(t-\mu)^2/2\phi^2} \quad 11.1$$

The electrical energy density ( $W$ ), with respect to the conductivity of the medium ( $\sigma_{med}$ ), number of pulses ( $N$ ), and the applied electric field ( $E(t)$ ) is expressed as:

$$W = N \cdot \sigma_{med} \int_0^\infty E(t)^2 \cdot dt = (E_{med})^2 \cdot N \cdot \sigma_{med} \int_0^\infty e^{-(t-\mu)^2/\phi^2} \cdot dt \quad 11.2$$

The amplitude of the applied electric field across the medium is represented by  $E_{med}$  ( $E_{med} = V_0/d$ ,  $d$  = gap distance). The trypan blue results are presented in terms of the electrical energy density (Fig. 11.3), in which both the electric field and the conductivity are dependent on the temperature. A separate experiment was added in which the pulse number was 100 for an applied electric field of 90 kV/cm at each temperature. The red lines represent same pulsing conditions (applied

electric field and pulse number). The electrical energy density for 100, 1,000 and 2,000 pulses (at room temperature) is  $1.7 \text{ J/cm}^3$ ,  $17 \text{ J/cm}^3$  and  $34 \text{ J/cm}^3$ , respectively. The electrical energy density increases with temperature as a result of a larger increase in conductivity of the medium than a decrease in the electric field strength across the sample. At  $47^\circ\text{C}$ , the energy density for a pulse number of 100, 1,000 and 2,000 pulses was  $2.2 \text{ J/cm}^3$ ,  $22 \text{ J/cm}^3$  and  $44 \text{ J/cm}^3$ , respectively.

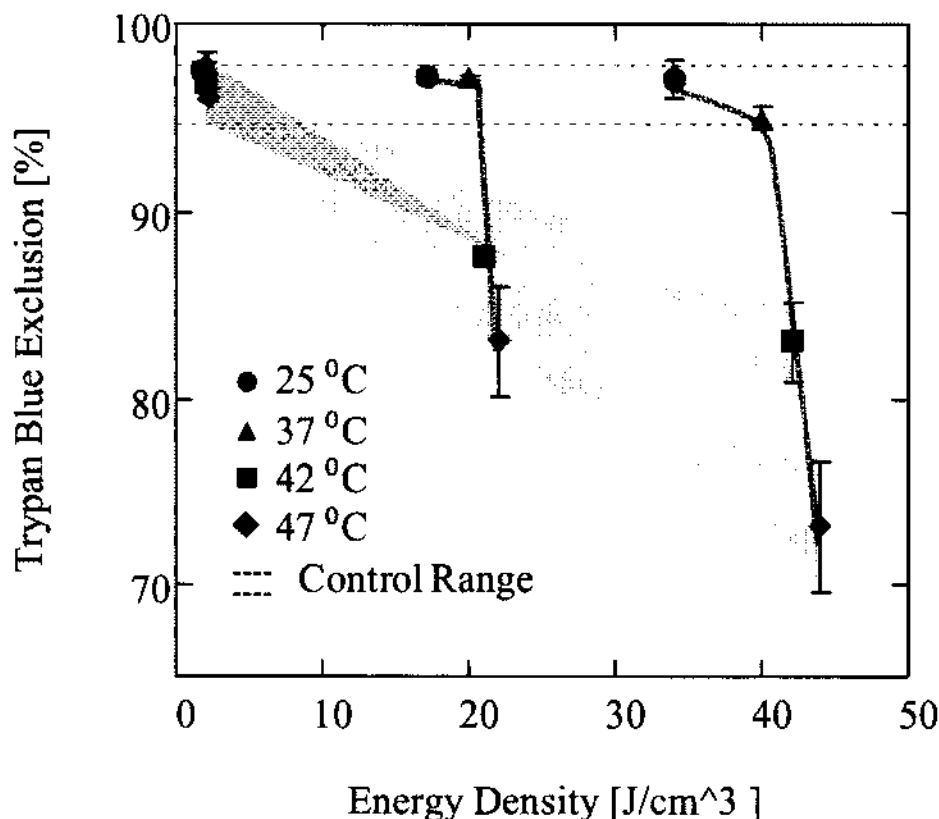


Fig. 11.3. Trypan blue exclusion results 4 hours after pulsing conditions in terms of the energy density of the medium. The red lines represent same experimental conditions (applied field and number of pulses).

For temperatures at and below  $37^\circ\text{C}$ , no distinguishable difference in the amount of trypan blue uptake is evident between the control and pulsed. Trypan blue uptake for cells exposed to  $42^\circ\text{C}$  and  $47^\circ\text{C}$  occurs at and above energy densities of  $20 \text{ J/cm}^3$ . The ratio of the energy density at  $47^\circ\text{C}$  to the energy density at  $42^\circ\text{C}$  is equal to 1.05 and is independent on the

number of pulses. At an energy density of  $22 \text{ J/cm}^3$ , the trypan blue exclusion at  $47^\circ\text{C}$  is equal to 83%, which is equal to the trypan blue exclusion at  $42^\circ\text{C}$  at an energy density of  $42 \text{ J/cm}^3$ . The ratio of the two energy densities is 1.9, which is much greater than the ratio of the energy density occurring at 1,000 pulses. As the temperature is increased above  $37^\circ\text{C}$ , the slope of the energy density also increases, resulting in a larger amount of cell death. The results indicate that the increase in cell death due to an increase in temperature is not caused by the increase in the energy density associated with a temperature increase. Such a decrease in the slope indicates the threshold for electroporation is decreased.

#### **XI.IV ELECTRIC FIELD THRESHOLD**

The dependence of trypan blue uptake (cell death) on the electric field intensity has been explored by varying the electric field strength across the sample between 52 kV/cm and 95 kV/cm, keeping the electrical energy density constant at  $44 \text{ J/cm}^3$ . The study was performed for a temperature of  $47^\circ\text{C}$ , where the strongest effect on the cells was observed. The results in terms of trypan blue exclusion, with  $n=3$ , are shown in Fig. 11.4. The results were taken 4 hours after exposure to the 200 ps pulses. At 52 kV/cm, there is no indication of trypan blue uptake, and/or cell death, beyond that observed in the sham studies. The sham control (average  $\pm$  standard deviation) is represented by the dashed gray lines. The concentration of cells which show trypan blue uptake increases strongly above 70 kV/cm but seem to level off for electric field values exceeding 80 kV/cm. Obviously a minimum electric field need to be applied to cause considerable membrane permeabilization for the given electrical energy density.

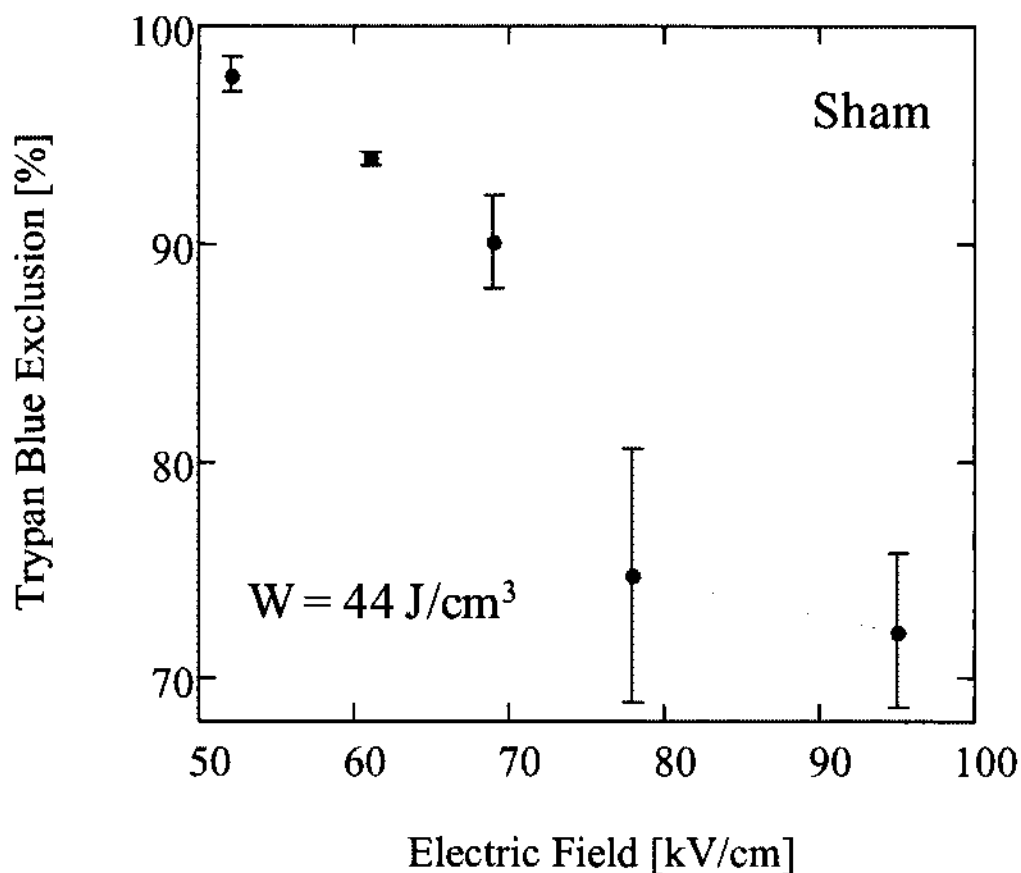


Fig. 11.4. Trypan blue exclusion 4 hours after experimental exposure at 47°C. The electrical energy density,  $W$ , was kept constant by decreasing the pulse number for an increase in electric field strength. The dashed lines show the range of the sham results.

#### **XLV CELL DEATH: IMMEDIATE MEMBRANE PERMEABILIZATION OR APOPTOSIS**

In order to determine whether or not the cells were permeabilized by the electric fields or if the cell death is a result of a delayed biological process (apoptosis), trypan blue was added to the sample prior to pulsing in a separate set of experiments. One minute after exposure, the cells were examined for membrane integrity for the following conditions:

- (a) 47°C, 78 kV/cm,  $N = 2000, 1000, 100$
- (b) 47°C, 61 kV/cm,  $N = 3306$ .
- (c) 25°C, 84 kV/cm,  $N = 2000$



Condition (b) is such that the electrical energy density ( $44 \text{ J/cm}^3$ ) is equivalent to condition (a) for an N of 2,000. The results are compared to the 4 hour results in Table 11.1.

Temperature = 47°C				
Time Point	Sham	78 kV/cm		61 kV/cm
		N = 1,000	N = 2,000	N = 3306
<b>0 hr (Avg.)</b>	<b>99.13%</b>	<b>84.4%</b>	<b>75.8%</b>	<b>97.3%</b>
0 hr (Std.)	0.65%	2.4%	4%	1.7%
<b>4 hr (Avg.)</b>	<b>96.2%</b>	<b>82.8%</b>	<b>74.8%</b>	<b>94%</b>
4 hr (Std.)	1.6%	2.9%	5.9%	0.58%

Table 11.1. Trypan blue exclusion of cells immediately after pulsing and 4 hours later (Avg.; average value, Std: standard deviation). There was no difference between the sham at 47°C and results of measurements at 25°C (not shown). The measurements at 61 kV/cm and at 84 kV/cm were conducted at the same electrical energy density.

A slight decrease in trypan blue exclusion exists in cell death for the sham, from 99% when examined immediately after pulsing to approximately 96% when measured 4 hours after pulsing. This slight decrease is a result of the cells being incubated for 4 hours in microfuge tubes. However, this decrease is negligible when compared to the cell death caused by the pulsed electric fields at 78 kV/cm. For exposure of the cells to these electric fields, it is obvious that cell death occurs immediately after the experimental procedure, likely due to membrane permeabilization. Apoptosis can be excluded as the cause for cell death under these conditions.

No statistical difference is evident in the amount of trypan blue exclusion for the sham and for the case that the electric field is reduced to 61 kV/cm (condition b), although the energy density has not been reduced. This lack of cell death indicates that the electric field needs to exceed a threshold value for the membrane permeabilization, as shown in Fig. 11.4. A negligible amount of trypan blue uptake is evident condition (c) in comparison to the control (not shown in the table).

## CHAPTER XII

### DISCUSSION OF RESULTS

The effect of cell death is clearly dependent on the temperature at which the cells are pulsed, as shown in Fig. 11.2. Cell death also depends on whether or not the electric field reaches a critical value as shown in Fig. 11.4. The critical value depends on the voltage across the membrane, in that a critical voltage is needed for the onset of electropermeabilization or electroporation. The fact that the uptake of trypan blue immediately follows pulsing indicates that membrane permeabilization is caused by the electric field acting directly on the plasma membrane, rather than on secondary effects such as those caused by apoptosis [140].

This chapter will discuss the possible reasons of why the temperature causes the cells to be more susceptible to pulsed electric fields, as well as eliminating any explanations which may seem plausible. In the first section, the induced membrane voltage and its dependence on the temperature is discussed. In the second section, the results are compared in terms of the amount of charge in the membrane during pulsing (scaling parameter) and the dose effect on the membrane opposed to the medium. The last section discusses the effects of membrane viscosity and compares molecular dynamic simulations with the experimental results.

#### XIII MEMBRANE VOLTAGE

The voltage induced across the cell membrane as a result of an external electric field,  $E_o$ , was derived in Chapter III and is given in (12.1).

$$V_m(\tau) = E_{med} \cdot \frac{d_m}{2 \cdot \epsilon_m} \cdot (\tau \cdot \sigma_{med} + 2 \cdot \epsilon_{med}) \quad 12.1$$

The temperature dependent electric field across the sample is denoted  $E_{med}$ . The relative permittivity of the membrane and medium are represented by  $\epsilon_m$  and  $\epsilon_{med}$ , respectively. The thickness of the membrane is represented by  $d_m$ , and was chosen to be 7 nm to be consistent with

the TDR analysis (Appendix B). The conductivity of the medium is represented by  $\sigma_{\text{med}}$  and the pulse width, 200 ps, is represented by  $\tau$ . The permittivity and conductivity values were taken from Table 3.1. The values of the induced membrane voltage, with an applied electric field of 90 kV/cm, for temperatures at 25°C, 37°C, 42°C, and 47°C are shown in Table 12.1.

$E_o$ [kV/cm]	$E_{\text{med}}$ [kV/cm]	Temperature [C]	$V_m$ [mV]
90	83	25	400
	80	37	343
	79	42	298
	78	47	265

Table 12.1. Relationship between the voltage across the membrane and temperature of the medium. The applied electric field is 90 kV/cm. The electric field across the sample,  $E_{\text{med}}$ , is reduced as a result of impedance of the sample, which is temperature dependent.

The voltage across the membrane decreases with an increase in temperature, which is a direct effect of the decrease in the electric field across the medium as well as a decrease in the permittivity of the medium and an increase in the membrane permittivity. The calculated membrane voltages in Table 12.1 indicate that a temperature increase causes a decrease in the threshold voltage needed to induce electroporation and/or electroporomeabilization. It is not possible for the threshold voltage to remain constant, yet have electroporomeabilization with an induced voltage of 265 mV, but not at 400 mV.

The membrane voltage in Table 12.1 does not include the resting potential, which will add to the membrane voltage on the side of the cell facing the anode and subtract from the membrane voltage on the side of the cell facing the cathode. The resting potential is approximately 70 mV to 80 mV [141, 142]. As stated in References [11-13], the resting potential increases linearly with the temperature. However, this linearity is based on the temperature in Kelvin, in which case, there would only be a 5 mV increase in the resting potential from 25°C to

47°C assuming a 70 mV resting potential at 25°C. Based on the assumption that the resting potential increases linearly with temperature, it is concluded that the increase in the resting potential superimposed with the induced membrane voltage does not make up for the decrease in the induced membrane voltage.

Table 12.2 shows the induced membrane voltages for the experiments shown in Fig. 11.4 (membrane permeabilization threshold at an energy density of 44 J/cm<sup>3</sup> at a temperature of 47°C).

$E_o$ [kV/cm]	$E_{med}$ [kV/cm]	Temperature [C]	$V_m$ [mV]
110	95	47	324
90	78	47	265
80	69	47	235
70	61	47	206
60	52	47	177

Table 12.2. Membrane voltage for threshold electric field experiments (Fig. 11.4).

The results from Fig. 11.4 indicate that at 47°C and at an energy density of 44 J/cm<sup>3</sup>, the threshold electric field, in order to achieve trypan blue uptake, is approximately 70 kV/cm, which equates to a membrane voltage of 235 mV. With the same energy density at 25°C, the membrane voltage is almost double (400 mV, Table 12.1), yet there is no distinguishable difference in the amount of trypan blue uptake from the control.

The threshold voltage for electroporation across a mammalian cell varies but is generally assumed to be 1 V [8, 9, 14]. However, measurements of the membrane voltage when 60 ns long pulses were applied to Jurkat cells showed that the position of the cell with respect to the direction of the electric field played a role in determining the threshold value for electropermeabilization or electroporation [144]. Voltages of up to 1.6 V could be reached at the anodic pole on a time scale of less than the temporal resolution of the measurements (5 ns) before

the membrane voltage leveled off. The membrane voltage at the cathodic pole increased slower, over a time of 15 ns to only 0.6 V, a value which indicates the threshold for electroporation at this pole.

The calculated membrane voltages in Table 12.1 and 12.2 are even less than the required voltage for cathodic pole. In addition, since the pulses in this study are applied for less than 200 ps, a much shorter duration than in the experiments described in reference [144], even if the membrane voltages would reach and exceed 0.6 V, it would be unlikely that pore formation can be achieved within this time frame. As reported from molecular dynamics simulations [6], it takes a few hundred picoseconds for the electric fields to re-orient the polar lipid head groups and the water to intrude into the membrane molecular structure. This re-orienting of the polar heads is an important initiating step in the formation of localized water nanowires, followed by pore development. Only the effect of multiple pulses, according to the results of the 200 ps pulses, enables the permeabilization of the plasma membrane and consequently the influx of trypan blue.

## **XII.II MEMBRANE CHARGES VERSUS MEMBRANE DOSE EFFECT**

### **XII.II.I Membrane Charges In Relation to the Temperature**

In the previous chapter, it was shown that the increase in cell death due to an increase in temperature was not a dose effect (Fig. 11.3). Rather, it was shown that the energy dose needed to induce cell death decreased with an increase in temperature. The reduction in the energy density from the 800 ps experiments in [1] to the experiments performed in this dissertation is all the more surprising since a scaling law for membrane permeabilization [4] predicts that, for shorter pulses, a higher energy density is required to obtain identical results. This scaling law, which provides a scaling or similarity parameter,  $S$ , is based on the assumption that the intensity of an observed bioelectric effect depends on the amount of electrical charges passing through the membrane when a pulse is applied [4]. The effect of pulse number,  $N$ , is determined by a statistical (thermal) motion of the cells between pulses:

$$S = S(E_{med} \cdot \tau \cdot \sqrt{N}) \quad 12.2$$

where  $E_{med}$  is the electric field intensity across the sample and  $\tau$  the pulse duration. Bursts of pulses with the product of these three quantities being the same should produce identical results.

The results of the 200 ps experiments in this dissertation, in terms of the scaling law, are shown in Fig. 12.1. The applied electric field for each data point is 90 kV/cm. The only variation in the pulsing conditions for the data in Fig. 12.1 was the number of pulses. The red lines connect the data points of the same pulse number (left: 100 pulses; middle: 1000 pulses; right: 2000 pulses). Due to the decrease in the electric field across the sample with increasing temperature, the scaling parameter also decreases (for constant pulsing conditions) with an increase in temperature; however, this decrease is negligible.

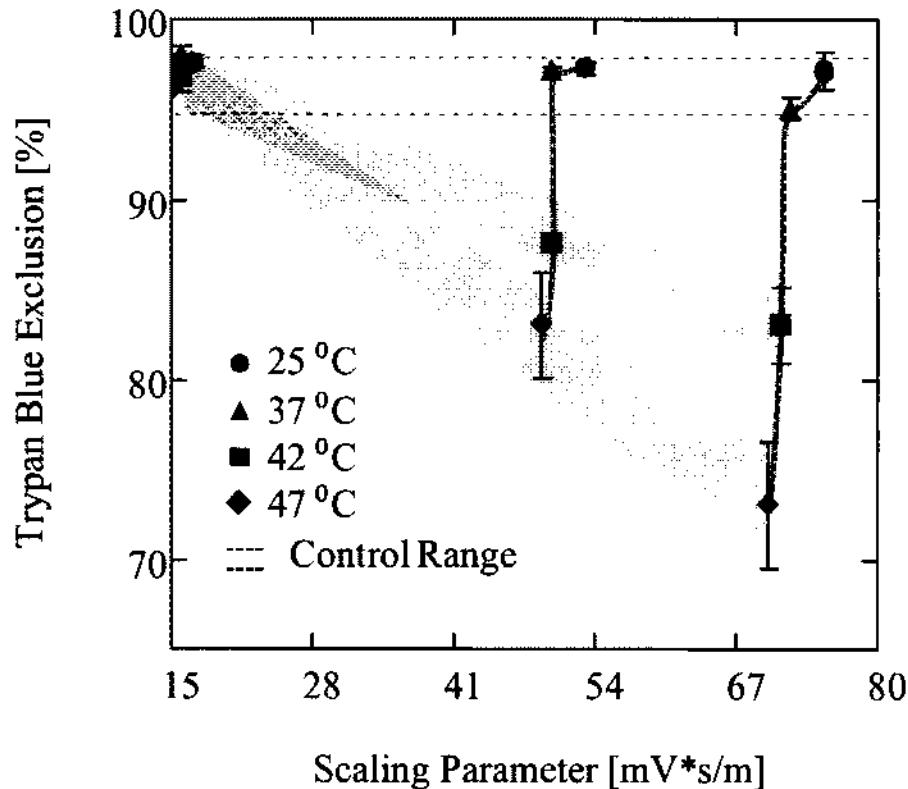


Fig. 12.1. Trypan blue exclusion 4 hours after experimental conditions ( $E_{applied} = 90$  kV/cm, 200 ps pulse width,  $N = 100, 1000, 2000$ ) in terms of the scaling parameter. The red line represents same pulsing conditions (applied electric field and number of pulses). The blue represents a different scaling parameter for 42°C and 47°C.

For temperatures at and above 42°C, the scaling parameter, needed to induce cell death, decreases with an increase in temperature. The blue highlights indicate the effect of membrane charging is different for exposure temperatures of 42°C and 47°C. The increase in cell death due to an increase in temperature for the same pulsing conditions does not scale with the amount of charge passing through the membrane. Rather, the amount of charge passing through the membrane needed to induce cell death from pulsed electric fields decreases with increasing temperature for temperatures at and above 42°C.

According to this scaling law for temperatures at and below 37°C, pulses shorter by about a factor of 4, as is the case for 800 and 200 ps pulses, would require a four times higher electric field, or a four times higher energy density (which scales with  $E^2\tau$ ). In these results, the opposite is observed: the energy density, required for a given uptake of trypan blue decreases by a factor 45 when the pulse duration is reduced from 800 ps to 200 ps. This counterintuitive effect could be due in part to the differences in cells used in the two studies, but more likely it is caused by the differences in temperature in the two experiments.

### **XII.II.II Membrane Dose Effect In Relation to the Temperature**

Up until now, the energy density measured the amount of energy delivered to the sample, which contained approximately 98% medium and 2% cells. Schoenbach et al. have shown the effects, expressed in terms of the energy density, do not scale with pulse duration [1], and it has been shown in Chapter XI that the effects in terms of the energy density does not scale with temperature. Rather than expressing the results in terms of the energy density of the sample, this section aims to express the results in terms of the energy density of the cell membrane.

The conductivity of the membrane increases by more than a factor of 4 with a temperature increase from 25°C to 47°C whereas the conductivity of the medium increased by less than 2. Since the energy density is dependent on the conductivity, the change in the energy

density of the membrane with increasing temperature will be more pronounced than the change in the energy density of the medium for the same increase in temperature.

The results of the experiments conducted at an applied electric field of 90 kV/cm (pulse numbers of 100, 1000, and 2000), expressed in terms of the membrane energy density, are shown in Fig. 12.2. The red lines connect the data points of the same pulse number. A slight decrease in the membrane energy density from 37°C to 42°C exists, followed by much stronger increase in the energy density from 42°C to 47°C. This trend was not evident for the energy density of the medium.

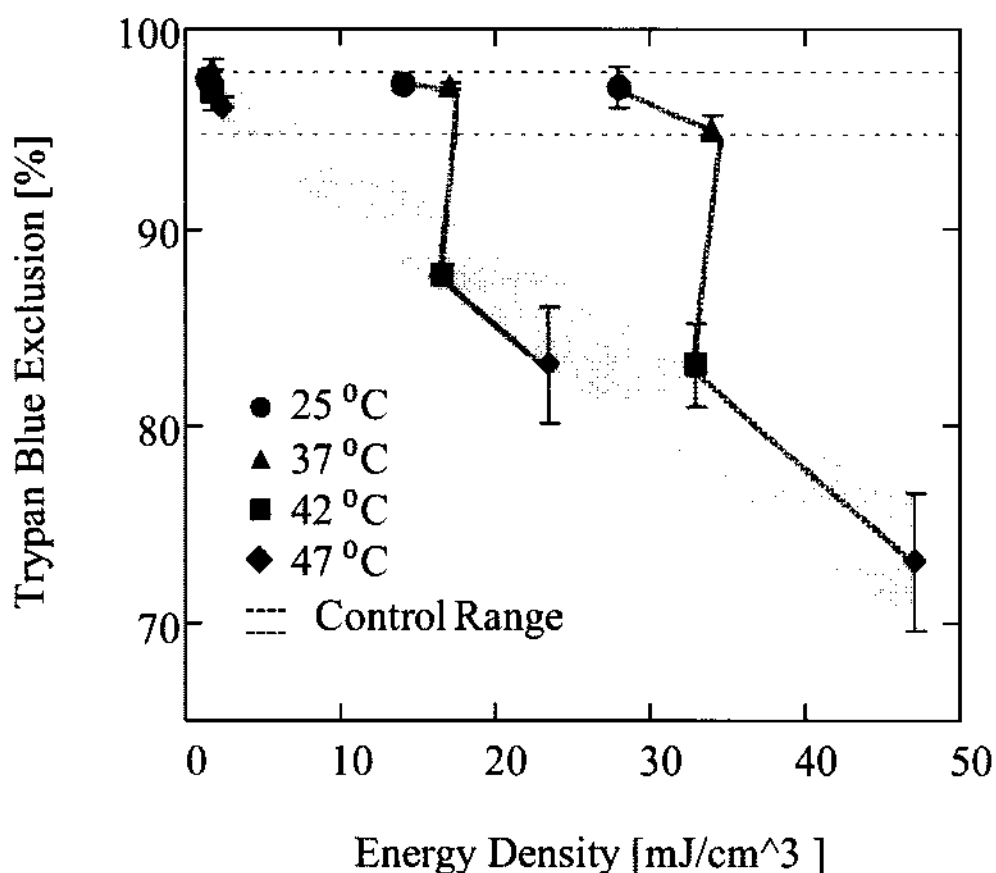


Fig. 12.2. Energy density of the membrane with respect to the temperature for cells exposed to an applied electric field of 90 kV/cm and pulse numbers of 100 (left) 1000 (middle) and 2000 (right). The red line connects the data points for cells exposed to the same pulse number. Temperatures at and below 37°C create a negligible effect on the cells. For temperatures at and above 42°C, a linear relation between the trypan blue exclusion and the energy density of the membrane exists, as shown by the blue highlight.



The energy density of the membrane ranges from  $1.4 \text{ mJ/cm}^3$  to  $47 \text{ mJ/cm}^3$ , which is approximately 3 orders of magnitude less than the energy density of the medium. For temperatures at and below  $37^\circ\text{C}$ , a negligible difference exists in the amount of trypan blue uptake between the control and pulsed cells. For temperatures at  $42^\circ\text{C}$  and above, a linear trend is evident in the amount of trypan blue uptake and the energy density of the membrane, which is defined by the range highlighted in blue. The results in Fig. 12.2 indicate that for temperatures at and above  $42^\circ\text{C}$ , the cell death can be attributed to a dose effect in terms of the energy delivered to the cell membrane, rather than the entire sample.

Although the dose effect in terms of the membrane may be able to predict the effects of pulsing for temperatures at and above  $42^\circ\text{C}$ , it still cannot account for the difference in effect for temperatures above and below  $37^\circ\text{C}$ . It is likely that an increase in temperature above the physiological temperature of the cell ( $37^\circ\text{C}$ ) decreases the threshold membrane energy density needed to induce cell death. Rather than a continuous decrease in the threshold with an increase in temperature (as observed with the scaling parameter and energy density of the medium), the increase in temperature directly increases the energy density of the membrane, which effectively increases the cell death.

Due to the short duration of the pulsed electric fields, the observed effects on the outer membrane may have also occurred on intracellular membranes as well, since the structure and composition of the outer membrane and intracellular membranes are similar. Irreversible damage to intracellular membranes is not distinguishable with trypan blue, which is strictly used to measure the permeabilization of the outer membrane. Therefore, any effects to intracellular membranes would not have been detected with trypan blue. It is possible that irreversible damage to intracellular membranes may have occurred, which would have lead to further cell death caused by apoptosis in a time frame longer than 4 hours. Such effects are most likely to occur on membranes surrounding the mitochondria opposed to the nucleus, since the nuclear membrane is already porous in nature.

### XII.III MEMBRANE VISCOSITY

Another aspect that must be taken into consideration for membrane permeabilization with ultrashort pulses is the temperature effect on the membrane viscosity or fluidity (Chapter XII) [62, 69] and pore formation enthalpy [145]. The formation of a pore in a lipid bilayer plasma membrane is depicted in Fig. 12.2. The dipole heads of the lipids are in random thermal motion when no electric field is applied. The positive charge is toward the aqueous solution, leaving the negative charge toward the interior of the membrane. With the application of an external electric field, the dipoles facing the cathode will align with the electric field, and the bonds may lengthen somewhat [6, 137]. However, the force on the lipids facing the anode will cause the polar heads to swing around as shown in Fig. 12.3 for time  $t_1$ . This motion will cause the positive side of the polar heads to repel one another leaving space for the aqueous solution to enter the membrane as depicted with the dark blue arrows.

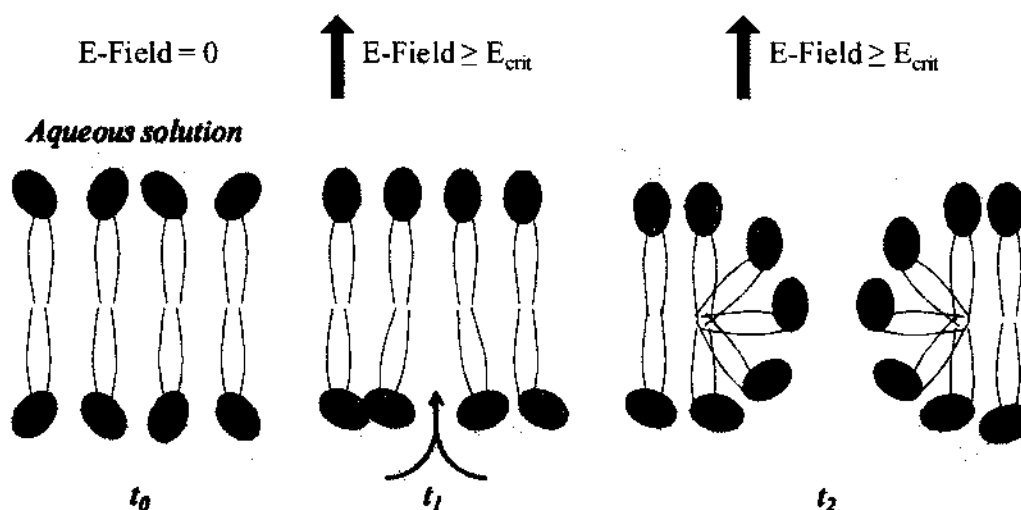


Fig. 12.3. Evolution of a pore formation due to an external electric field. At  $t_0$ , the heads of the lipids are in random motion. At  $t_1$ , an external electric field is applied and the lipid heads facing the cathode will align with the electric field. The heads of the lipids facing the anode will rotate to try and align, causing repulsion between them. This repulsion may cause an opening to allow the aqueous solution through the membrane as depicted at time  $t_2$  [48].

Thus water intrusion into the lipid structure can commence and would be the start of a poration process. Eventually, a water-wire (or bridge) through the lipid bilayer would form. The intrusion of water molecules would simultaneously push the hydrophobic leaflets causing them to rotate as depicted in Fig. 12.3 at time  $t_2$ . These water intrusions are expected to initiate at random sites based on instantaneous local potentials and zig-zag along into the lipid bilayer, much like “lightening streamers”. These streamers can lead to the formation of a pore. This process depends on the viscosity and thermal motion of the membrane, because a less viscous membrane requires less energy to create a pore.

This observation is evident in the molecular dynamic simulations of a lipid layer with constant electric field strength of 0.5 V/nm at 25°C and 47°C (Appendix C). A similar trend toward a synergism involving both thermal and electrically driven bio-phenomena has recently been reported [7]. The simulation results of Fig. 12.4 are in agreement with the experimental trends in that no pore formation occurs at 25°C. However, at 47°C, a clear indication of pore formation at 0.75 ns exists which increases at 1 ns. The results underscore the role of temperature in facilitating and accelerating the poration process. The MD results, by showing snapshots of membrane poration at two specific temperatures, point to the possibility that relatively modest variations in temperature can result in different degrees of electrically stimulated bio-effects. The effects of the decrease in viscosity with temperature which, in my opinion, is the main cause of the lowering of the threshold for electroporation or electropermeabilization, lead to a considerable reduction of electrical energy density required to achieve cell death, compared to pulsed electric field effects at (or less than) physiological temperature. This is obvious when the required energy densities for trypan blue uptake after 800 ps pulse exposure, in experiments where the temperature was kept below the physiological temperature, are compared with those used in this study.

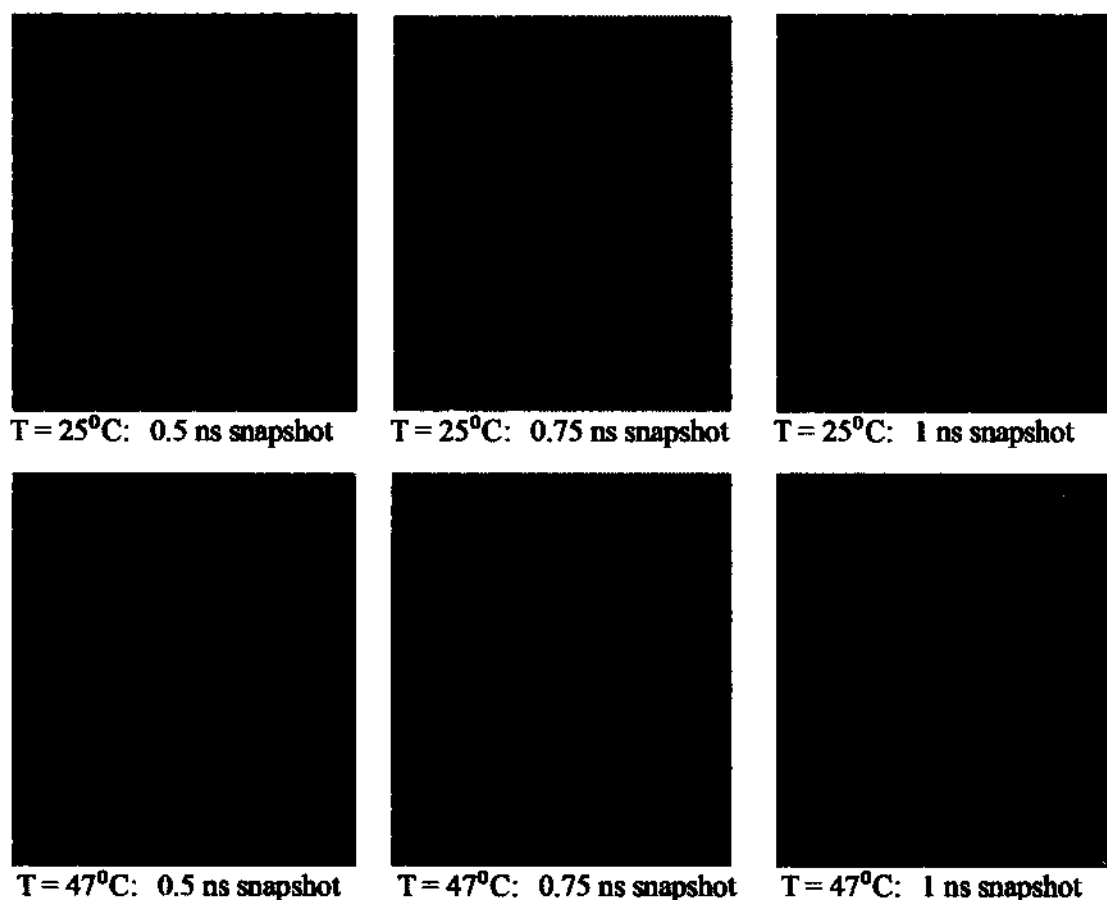


Fig. 12.4. Molecular dynamic simulations of a lipid bilayer exposed to a constant electric field strength of 0.5 V/nm for 1 ns at 25°C and 47°C [48].

Although different cell types were used - melanoma cells in the 800 ps pulse studies [1] compared to Hepa 1-6 cells in this study, the strong reduction in energy density is obvious. In the 800 ps studies at temperatures below 37°C the medium energy density required to achieve a 25% reduction in viability was 2 kJ/cm<sup>3</sup>. It was reduced to 44 J/cm<sup>3</sup> for the 200 ps pulses at elevated temperatures of 47°C, a reduction by a factor of 45. Although it is known that Hepa cells require less energy to induce cell death compared to melanoma cells, by increasing the temperature above the physiological value, the reduction in energy density, or the gain in efficiency, likely exceeds one order of magnitude.

## CHAPTER XIII

### SUMMARY

The use of subnanosecond pulsed electric fields may lead to non-invasive delivery systems for introducing an electric field within biological tissue. Two applications of such an approach is medical imaging and cancer treatment. In the case of cancer treatment, the subnanosecond pulsed electric fields would be required to induce cell death. Previous experiments suggests that energy densities on the order of  $10 \text{ kJ/cm}^3$  are needed to induce cell death, *in vitro*, for 200 ps pulses for electric fields strengths less than 100 kV/cm, which equates to a pulse number in the millions. The purpose of this dissertation was to show the energy density required for cell death can be reduced by at least 3 orders of magnitude by increasing the temperature of the sample above physiological temperature ( $37^\circ\text{C}$ ), which consequently decreases the number of pulses to the thousands.

The temperature experiments were conducted by controlling the temperature of the biological sample externally during the application of the pulsed electric fields, while minimizing temperature effects due to ohmic heating. It was shown by measuring the thermal decay constant of the chamber and calculating the leveling temperature that the temperature increase due to pulsing did not reach values above  $1^\circ\text{C}$ . It was also shown that the electric field across the sample decreased with an increase in temperature due to the temperature dependence of the permittivity and conductivity of the sample solution. An applied electric field of 90 kV/cm resulted in an electric field strength of 83 kV/cm across the sample at room temperature, and decreased to 78 kV/cm for a temperature at  $47^\circ\text{C}$ .

Trypan blue uptake by liver cancer cells, indicating cell death, was found to increase strongly with increasing temperature above the physiological temperature when pulses of 200 ps duration were applied to cells *in vitro*. With 2,000 pulses at 78 kV/cm and a temperature of the biological sample of  $47^\circ\text{C}$ , approximately 25% of the cells took up trypan blue. Experiments at

this elevated temperature without pulsing revealed that the cells can survive at these temperatures for 10 minutes before any fatalities were experienced. Since the time required for fatality is long compared to the time the cells were kept at this temperature under pulsed conditions ( $< 6$  minutes), cell death due solely to elevated temperatures can be excluded. No indication of cell death was evident when the cells were pulsed at 83 kV/cm with the same number of pulses at 25°C. The observed cell death at the elevated temperature can therefore not be attributed to temperature alone, but must be a synergistic effect of temperature and pulsed electric fields.

At an energy density of 44 J/cm<sup>3</sup>, the peak electric field intensity of the subnanosecond pulses needed to exceed 70 kV/cm to enable trypan blue uptake of the cells. Increasing the electric fields beyond this value caused a steep increase in the numbers of cells dying, but seems to level off at electric fields exceeding 80 kV/cm. The energy density in this study was kept below 60 J/cm<sup>3</sup>. This is more than an order of magnitude less than recorded for experiments on B16 cells with 800 ps pulses. The results indicated that a continuous increase in temperature above 37°C caused a continuous decrease in the threshold needed to induce cell death for both the energy density and the scaling parameter. As a result, the resulting cell death with an increase in temperature is neither a dose effect nor a membrane charging effect.

A new approach was introduced in this dissertation in which cell death was presented in terms of the energy density of the membrane, rather than the medium. The energy density of the membrane is three orders of magnitude less than the energy density of the medium, but increases by a factor of 1.3 for a temperature increase from 42°C to 47°C, whereas the increase in the energy density of the medium is only 1.05. This large increase indicates a linear trend between the cell death and the energy density of the membrane, independent on temperature for temperatures at and above 42°C. In other words, the increase in temperature caused an increase in the energy density of the membrane, which resulted in more cell death. However, this effect is only evident if the temperature is above 37°C, suggesting that the threshold energy across the

membrane needed to induce permeabilization falls below the induced membrane energy due to an applied electric field when the temperature reaches a value between 37°C and 42°C.

The cause of cell death was due to instant (relative to the time it took to measure the effect after pulsing) membrane permeabilization, rather than apoptosis, demonstrated through experiments where trypan blue was added to the suspension before pulsing. The increased sensitivity of cells to pulsed electric fields with temperature is assumed to be due to reduced viscosity of the plasma membrane at elevated temperatures. Water intrusions into the membrane are expected to be initiated at random sites based on the instantaneous local potentials, leading to pore formation. This process depends on the viscosity and thermal motion of the membrane, in that a less viscous membrane requires less energy to create a pore at higher temperatures. Molecular dynamics simulations have demonstrated the increased probability of pore formation at elevated temperatures.

The effects studied in this dissertation were strictly on the outer membrane of the cell: membrane permeabilization and cell death due to membrane permeabilization. However, due to the short duration of the pulsed electric fields, the effects on the pulses on the intracellular membranes cannot be excluded. The increase in susceptibility of the cell to pulsed electric fields due to an increase in temperature not only shows promising results for subnanosecond pulses, but may have similar effects on any pulses which affect the outer membrane of a cell. A non lethal application is using pulsed electric fields to deliver genes or drugs into the cell such that an increase in temperature may reduce the energy needed for gene/drug delivery. In the case of non-invasive cancer treatment, narrowband sources are readily available which can be used to locally heat the tissue to non-lethal temperatures using the same antenna setup in Fig. 1.2. Before the temperature of the exposed sample decays to a value below a specified temperature (above 37°C), a subnanosecond pulse generator based on semiconductor switches (Chapter V) can be used to deliver thousands of pulses to the tissue in less than a second due to the high repetition rate (10<sup>6</sup> kHz).

## REFERENCES

1. Schoenbach, K.H.; Shu Xiao; Joshi, R.P.; Camp, J.T.; Heeren, T.; Kolb, J.F.; Beebe, S.J.; "The Effect of Intense Subnanosecond Electrical Pulses on Biological Cells," *IEEE Trans. On Plasma Sci.*, vol.36, no.2, pp.414-422, April 2008.
2. Xiao, S. Guo, V. V. Nesin, R. Heller, and K. H. Schoenbach, "Subnanosecond electric pulses cause membrane permeabilization and cell death," *IEEE Trans. on Biomed. Eng.*, vol. 58, no. 5, pp. 1239-1245, 2011.
3. R. P. Joshi, and Qin Hu, "Case for Applying Subnanosecond High-Intensity, Electrical Pulses to Biological Cells," *IEEE Trans. On Bio. Engr.*, vol.58, no.10, pp.2860-2866, Oct. 2011.
4. Schoenbach, K.; Joshi, R.; Beebe, S.; Baum, C.; "A scaling law for membrane permeabilization with nanopulses," *IEEE Trans. On Dielect. And Elect. Ins.*, vol.16, no.5, pp.1224-1235, Oct. 2009.
5. R. P. Joshi, Q. Hu, R. Aly, K. H. Schoenbach, and H. P. Hjalmarson, "Self-consistent simulations of electroporation dynamics in biological cells subjected to ultrafast electrical pulses", *Phys. Rev. E.*, vol. 64, pp. 11913/01-3, 2001.
6. Q. Hu, R. P. Joshi, and K. H. Schoenbach, "Simulations of nanopore formation and phosphatidylserine externalization in lipid membranes subjected to a high-intensity, ultrashort electric pulse," *Physical Review*, vol. 72 pp. 1539-3755, 2005.
7. J. Song, R. P. Joshi, and Karl H. Schoenbach, "Synergistic effects of local temperature enhancements on cellular responses in the context of high-intensity, ultrashort electric pulses," *Med. Biol. Eng. Comp.*, vol. 49, pp. 713 – 718, 2011.
8. James C. Weaver, "Electroporation of Cells and Tissue," *IEEE Trans. Plasma Sci*, vol. 28, no. 1, 2000.
9. Tian Y. Tsong, "Electroporation of Cell Membranes: Minireview," *Biophys. J.*, vol. 60, pp. 297-306, 1991.



10. R. P. Joshi, Q. Hu, K. H. Schoenbach, and H. P. Hjalmarson, "Improved energy model for membrane electroporation in biological cells subjected to electrical pulses", *Phys. Rev. E.*, Vol. 65, pp. 041920/01-07, 2002.
11. P. Remani, Valentina V. Ostapenko, K. Akagi, V.N. Bhattathiri, M. Krishnan Nair, Y. Tanaka, "Relation of transmembrane potential to cell survival following hyperthermia in HeLa cells," *Cancer Letters*, vol. 144, pp. 117-123.
12. Reinaldo Dipolo and Ramon Latorre, "Effect of Temperature on Membrane Potential and Ionic Fluxes in Intact and Dialysed Barnacle Muscle Fibers," *J. Physiol.*, no. 225, pp. 255-273, 1972.
13. Lorenzo Marchiafava, "The Effect of Temperature Change on Membrane Potential and Conductance in Aplysia Giant Nerve Cell," *Comp. Biochem. Physiol*, vol. 34, pp. 847-852, 1969.
14. J. Gehl, "Electroporation: Theory, and methods, perspectives for drug delivery, gene therapy and research," *Acta. Physiol. Scand.*, vol. 177, pp. 437-447, 2003.
15. M. Kandušer a, M. Šentjurs b, D. Miklavčič, "The temperature effect during pulse application on cell membrane fluidity and permeabilization," *Bioelectrochemistry*, vol. 74, pp. 52-57, 2008.
16. Kang Cheng, "An improved biophysical model of electroporation of cell membrane," *Engineering in Medicine and Biology Society, 1996. Bridging Disciplines for Biomedicine. Proceedings of the 18th Annual International Conference of the IEEE* , vol.5, no., pp.1915-1916 vol.5, 31 Oct-3 Nov 1996.
17. Kang Cheng, "Development of biomechanical models of electroporation," *Biomedical Engineering Conference, 1995., Proceedings of the 1995 Fourteenth Southern* , vol., no., pp.183-184, 7-9 Apr 1995.

18. Hyun-Gyun Yuk and Douglas L. Marshall, "Heat Adaptation Alters *Escherichia coli* O157:H7 Membrane Lipid Composition and Verotoxin Production," *Applied and Environmental Microbiology*, Sept. 2003, pp. 5115-5119.
19. Michael Sinensky, "Homeoviscous Adaptation-A Homeostatic. Process that Regulates the Viscosity of Membrane Lipids in *Escherichia coli*," *Proc. Nat. Acad. Sci. USA*, Feb. 1974, pp. 522-525.
20. K. H. Schoenbach, B. Hargrave, R. P. Joshi, J. F. Kolb, C. Osgood, R. Nuccitelli, A. Pakhomov, R. J. Swanson, M. Stacey, J. A. White, S. Xiao, J. Zhang, S. J. Beebe, P. F. Blackmore, and E. S. Buescher, "Bioelectric effects of intense nanosecond pulses," *IEEE Trans. Dielectr. Electr. Insul.*, vol. 14, no. 5, pp. 1088-1119, Oct. 2007.
21. K. H. Schoenbach, R. P. Joshi, J. F. Kolb, N. Chen, M. Stacey, P. F. Blackmore, E. S. Buescher, and S. J. Beebe, "Ultrashort electrical pulses open a new gateway into biological cells," *Proc. IEEE*, vol. 92, no. 7, pp. 1122-1137, Jul. 2004.
22. K. H. Schoenbach, S. J. Beebe, and E. S. Buescher, "Intracellular effect of ultrashort electrical pulses," *Bioelectromagnetics*, vol. 22, no. 6, pp. 440-448, 2001.
23. E. S. Buescher and K. H. Schoenbach, "Effects of submicrosecond, high intensity pulsed electric fields on living cells-intracellular electromanipulation," *IEEE Trans. Dielectr. Electr. Insul.*, vol. 10, no. 5, pp. 788-794, Oct. 2003.
24. P. T. Vernier, Y. H. Sun, L. Marcu, C. M. Craft, and M. A. Gundersen, "Nanosecond pulsed electric fields perturb membrane phospholipids in T lymphoblasts," *FEBS Lett.*, vol. 572, no. 1-3, pp. 103-108, 2004.
25. J. A. White, P. F. Blackmore, K. H. Schoenbach, and S. J. Beebe, "Stimulation of capacitative calcium entry in HL-60 cells by nanosecond pulsed electric fields," *J. Biol. Chem.*, vol. 279, no. 22, pp. 22 964-22 972, May 2004.

26. E. S. Buescher, R. R. Smith, and K. H. Schoenbach, "Submicrosecond intense pulsed electric field effects on intracellular free calcium: Mechanisms and effects," *IEEE Trans. Plasma Sci.*, vol. 32, no. 4, pp. 1563–1572, Aug. 2004.
27. J. Zhang, P. F. Blackmore, B. Y. Hargrave, S. Xiao, S. J. Beebe, and K. H. Schoenbach, "Nanosecond pulse electric field (nanopulse): A novel non-ligand agonist for platelet activation," *Arch. Biochem. Biophys.*, vol. 471, no. 2, pp. 240–248, 2008. DOI:10.1016/j.abb.2007.12.009.
28. S. J. Beebe, P. M. Fox, L. J. Rec, E. L. Willis, and K. H. Schoenbach, "Nanosecond, high-intensity pulsed electric fields induce apoptosis in human cells," *FASEB J.*, vol. 17, no. 11, pp. 1493–1495, 2003.
29. S. J. Beebe, P. F. Blackmore, J. White, R. P. Joshi, and K. H. Schoenbach, "Nanosecond pulsed electric fields modulate cell function through intracellular signal transduction mechanisms," *Physiol. Meas.*, vol. 25, no. 4, pp. 1077–1093, Aug. 2004.
30. S. J. Beebe, J. White, P. F. Blackmore, Y. Deng, K. Somers, and K. H. Schoenbach, "Diverse effects of nanosecond pulsed electric fields on cells and tissues," *DNA Cell Biol.*, vol. 22, no. 12, pp. 785–796, 2003.
31. P. T. Vernier, A. Li, L. Marcu, C. M. Craft, and M. A. Gundersen, "Ultrashort pulsed electric fields induce membrane phospholipid translocation and caspase activation: Differential sensitivities of Jurkat T lymphoblasts and rat glioma C6 cells," *IEEE Trans. Dielectr. Electr. Insul.*, vol. 10, no. 5, pp. 795–809, Oct. 2003.
32. R. Nuccitelli, U. Pliquett, X. Chen, W. Ford, J. Swanson, S. J. Beebe, J. F. Kolb, and K. H. Schoenbach, "Nanosecond pulsed electric fields cause melanomas to self-destruct," *Biochem. Biophys. Res. Commun.*, vol. 343, no. 2, pp. 351–360, May 2006.
33. Nuccitelli, R., Chen, X., Pakhomov, A. G., Baldwin, W. H., Sheikh, S., Pomietter, J. L., Ren, W., Osgood, C., Swanson, R. J., Kolb, J. F., Beebe, S. J. and Schoenbach, K. H., "A new

- pulsed electric field therapy for melanoma disrupts the tumor's blood supply and causes complete remission without recurrence," *Inter. J. of Cancer*, no. 125 pp. 438–445, 2009.
34. Vrba, Jan "Microwave Applicators for Medical Applications: Imaging and Thermo-therapy Treatment." *Microwave Review*, June 2005.
  35. Baum, C. E., "Focal waveform of a prolate-spheroidal impulse-radiating antenna," *Radio Sci.*, vol. 42, 2007.
  36. Carl Baum, University of New Mexico, private communication, 2009.
  37. Magic user's manual, Mission Research Corporation, October 2003.
  38. Shu Xiao, Karl H. Schoenbach, and Carl E. Baum, "Time-Domain Focusing Radar for Medical Imaging," *Proc. URSI, XXIX Gen. Assembly of URSI, Chicago, IL*, 2008.
  39. Fear, E.; Low, A.; Sill, J.; Stuchly, M.A.; , "Microwave system for breast tumor detection: experimental concept evaluation," *Antennas and Propagation Society International Symposium, 2002. IEEE* , vol.1, no., pp. 819- 822 vol.1, 2002.
  40. Tammo Heeren, J. Thomas Camp, Juergen F. Kolb, Karl H. Schoenbach, Sunao Katsuki, and Hidenori Akiyama, "250 kV Subnanosecond Pulse Generator with Adjustable Pulsewidth," *IEEE Trans. Dielect. Electr. Insul.* 14, pp. 884-888 (2007).
  41. Qin Hu, and R. P. Joshi, "Analysis of Intense, Subnanosecond Electrical Pulse-Induced Transmembrane Voltage in Spheroidal Cells With Arbitrary Orientation," *Biomedical Engineering, IEEE Transactions on*, vol.56, no.6, pp.1617-1626, June 2009.
  42. S. Jayaram, G. S. P. Castle, and A. Margaritis, "Effects of High Electric Field Pulses on *Lactobacillus Brevis* at Elevated Temperatures," *Industry Applications Society Annual Meeting, 1991., Conference Record of the 1991 IEEE* , vol., no., pp.674-681 vol.1, 28 Sep-4 Oct 1991.
  43. Takayuki Ohshima, Kanako Okuyama, Masayuki Sato, "Effect of culture temperature on high voltage pulse sterilization of *Escherichia coli*," *Journal of Electrostatics*, vol. 55, pp. 227-235, 2002.

44. R. Waugh and E. A. Evans, "Thermoelasticity of red blood cell membrane," *Biophys. J.*, pp. 115-132, 1979.
45. Y. Sun, S. Xiao, J. A. White, J. F. Kolb, M. Stacey, and K. H. Schoenbach, "Compact, nanosecond, high repetition-rate, pulse generator for bioelectric studies," *IEEE Trans. Dielectr. Electr. Insul.*, vol. 14, no. 4, pp. 863-870, Aug. 2007.
46. E. L. Carstensen and R. E. Marquis, "Conductivity of Isolated Bacterial Cell Walls," *Biophys. J.*, vol. 8, pp. 536 - 548, 1968.
47. Schoenbach, K.H.; Katsuki, S.; Akiyama, H.; Heeren, T.; Kolb, J.F.; Xiao, S.; Camp, T.; Joshi, R.P.; Osgood, C.; Nuccitelli, R.; Beebe, S.J.; , "Biological Effects of Intense Subnanosecond Electrical Pulses," *Power Modulator Symposium, 2006. Conference Record of the 2006 Twenty-Seventh International*, pp.573-576, 14-18 May 2006.
48. J. Thomas Camp, Yu Jing, Jie Zhuang, Juergen Kolb, Stephen J. Beebe, Jiahui Song, Ravindra P. Joshi, Shu Xiao, Karl H. Schoenbach, "Cell Death Induced by Subnanosecond Pulsed Electric Fields at Elevated Temperatures," Submitted to *Transactions on Plasma Science*, Dec. 2011.
49. Irina Ermolina, Yulia Poleyeva, Yuri Feldman, Ben Ginzburg and Michael Schlesinger, "Study of Normal and Malignant White Blood Cells by Time Domain Dielectric Spectroscopy," *IEEE Trans. Dielect. And Elec. Ins.*, vol. 8, no. 2, April 2001.
50. Jutiporn Sudsiri, Derk Wachner, Jan Gimsa, "On the temperature dependence of the dielectric membrane properties of human red blood cells," *Bioelectrochemistry*, vol. 70, iss. 1, 2005.
51. Jie Zhuang; Baldwin, W.H.; Schoenbach, K.H.; Kolb, J.F.; , "Pulsed electric field induced changes in dielectric properties of biological cells," *Power Modulator and High Voltage Conference (IPMHVC), 2010 IEEE International*, pp.200-203, 23-27 May 2010
52. G. Qiao, W. Duan, C. Chatwin, A. Sinclair, and W. Wang, "Electrical Properties of Breast Cancer Cells From Impedance Measurement of Cell Suspensions," *J. Phys. Conf. Ser.* 224, 2010.

53. Garner, A.L.; Nianyong Chen; Jing Yang; Kolb, J.; Swanson, R.J.; Loftin, K.C.; Beebe, S.J.; Joshi, R.P.; Schoenbach, K.H.; , "Time domain dielectric spectroscopy measurements of HL-60 cell suspensions after microsecond and nanosecond electrical pulses," *Plasma Science, IEEE Transactions on* , vol.32, no.5, pp. 2073- 2084, Oct. 2004.
54. Wolf, M & Gulich, R & Lunkenheimer, P & Loidl, A., "Broadband dielectric spectroscopy on human blood," *Biochimica et biophysica acta*. 2011.
55. Gurtovenko, A. A.; Vattulainen, "Ion Leakage through Transient Water Pores in Protein-Free Lipid Membranes Driven by Transmembrane Ionic Charge Imbalance" *Biophys. J.*, vol. 92, pp. 1878 – 1890, 2007.
56. Lars Onsager, "Electric Moments of Molecules in Liquids," *Am. Chem. Soc.*, 58 (8), pp 1486–1493, 1936.
57. MathCad 14.0 Copyright © 2007 Parametric Technology Corporation. All Rights Reserved.
58. Blaz Valic, Mojca Pavlin, Damijan Miklavcic, "The effect of resting transmembrane voltage on cell electroporabilization: A numerical analysis," *J. Biochem.* vol. 63, pp. 311-315, 2004.
59. S. J. Singer and Garth L. Nicolson, "The Fluid Mosaic Model of the Structure of Cell Membranes," *Science*, New Series, vol. 175, no. 4023, pp. 720-731, Feb. 1972.
60. Jeffrey R. Hazel, "Thermal Adaptation in Biological Membranes: Is Homeoviscous Adaptation the Explanation?" *Annu. Rev. Physiol*, pp. 19-42, 1995.
61. Ernst J.M. Helmreich, "Environmental influences on signal transduction through membranes: a retrospective mini-review," *Biochemical Chemistry*, pp. 519-534, 2003.
62. Alexandre Martinie`re, Maria Shvedunova, Adrian J.W. Thomson, Nicola H. Evans, Steven Penfield, John Runions and Harriet G. McWatters, "Homeostasis of plasma membrane viscosity in fluctuating temperatures," *New Phytologists*, 2011.

63. R.N. McElhaney, K.A. Souza, "The relationship between environmental temperature, cell growth and the fluidity and physical state of the membrane lipids in bacillus stearothermophilus," *Biochim. Biophys. Acta* 443 pp. 348–359, 1976.
64. M. Sinensky, "Homeoviscous adaptation-a homeostatic process that regulates the viscosity of membrane lipids in Escherichia coli," *Proc. Nat. Acad. Sci. USA*, vol. 71, pp. 522–525, 1974.
65. Yehudith Ghetler, Saar Yavin, Ruth Shalgi and Amir Arav, "The Effect of Chilling on Membrane Lipid Phase Transition in Human Oocytes and Zygotes," *Human Reproduction*, vol. 20, no. 12, pp. 3385-3389, 2005.
66. Guillaume T. Charras, Margaret Coughlin, Timothy J. Mitchison, and L. Mahadevan, "Life and Times of Cellular Blebb" *Biophys. J.* vol. 94, pp. 1836-1853, 2008.
67. J. C. Bischof, J. Padanilam, W. H. Holmes, R. M. Ezzell, R. C. Lee, R. G. Tompkins, M. L. Yarmush, and M. Toner, "Dynamics of Cell Membrane Permeability Changes at Supraphysiological Temperatures," *Biophys. J.* vol. 68, pp. 2608-2614, 1995.
68. Allen G. Marr, and John L. Ingraham, "Effect of Temperature on the Composition of Fatty Acids in Escherichia Coli," *J. Bacteriol.*, vol. 84, no. 6, pp. 1260 - 1267, 1962.
69. Diana A. Bates, Christian Le Grimellec, and Jason H. T. Bates, "Effects of Thermal Adaptation at 40°C on Membrane Viscosity and the Sodium-Potassium Pump in Chinese Hamster Ovary Cells," *Cancer Research*, 1985, pp. 4895-4899.
70. Sophie Raffy and Justin Teissie, "Control of Lipid Membrane Stability by Cholesterol Content," *Biophysical Journal*, pp. 2072-2078, April, 1999.
71. Alister G. MacDonald, "Application of the theory of homeoviscous adaptation to excitable membranes: pre-synaptic processes," *Biochem. J.*, pp. 313-327, 1988.
72. Masa Kanduser, Marjeta Sentjunc and Damijan Miklavc ic, "Cell membrane fluidity related to electroporation and resealing," *Eur. Biophys. J.*, pp. 196-204, 2006.
73. Kouichi Nakagawa, "EPR Investigations of Spin-Probe Dynamics in Aqueous Dispersions of Nonionic Amphiphilic Compound," *J. Am. Oil Che. Soc.*, vol. 86, pp. 1-17, 2009.

74. P. G. Saffman, and M. Delbruck, "Brownian motion in biological membranes," *Proc. Nat. Acad. Sci.* vol. 72, no. 8, pp. 3111-3113, 1975.
75. David Brown and Don Martin, "Subnanosecond High-Voltage Pulse Generator," *rev. sci. instrum.*, vol. 58, no. 8, pp. 1523-1529, 1987.
76. D. McDonald, and C. Benning, "Subnanosecond Risetime Multikilovolt Pulse Generator," *rev. sci. instrum.*, vol. 36, no. 4, pp. 504-506, 1965.
77. M. R. Ul'maskulov, S. A. Shunailov, K. A. Sharypov, V. G. Shpak, and M. I. Yalandin, "A Compact Subnanosecond High\_Voltage Bipolar Pulse Generator with Spark Gaps," *Instr. And Exp. Techn.*, vol. 53, no. 6, pp. 825-829, 2010.
78. Pavitra Krishnaswamy, Andras Kuthi, P. Thomas Vernier, and Martin A. Gundersen, "Compact Subnanosecond Pulse Generator Using Avalanche Transistors for Cell Electroperturbation Studies," *IEEE Trans. on Dielect. and Electr. Insul.*, vol. 14, no. 4, pp. 871-877, 2007.
79. T. Heeren, T. Ueno, H. Akiyama, "Miniature, Solid State, Kilivolt, Nanosecond Pulse Generator with Variable Pulse Width, Pulse Polarity, and Pulse Frequency," *Pulsed Power Conference, 2005 IEEE* , vol., no., pp.1360-1363, 13-17 June, 2005.
80. Lyubutin, S.K.; Mesyats, G.A.; Rukin, S.N.; Slovikovskii, B.G.; , "Subnanosecond high-density current interruption in SOS diodes," *Pulsed Power Conference, 1997. Digest of Technical Papers. 1997 11th IEEE International* , vol.1, no., pp.663-666 vol.1, 29 Jun-2 Jul 1997.
81. Rukin, S.N.; Alichkin, E.A.; Lyubutin, S.K.; Mesyats, G.A.; Ponomarev, A.V.; Slovikovsky, B.G.; Timoshenkov, S.P.; , "SOS/DBD-based solid state switching for ultra-high-power short pulse generation," *Power Modulator Symposium, 2002 and 2002 High-Voltage Workshop. Conference Record of the Twenty-Fifth International* , vol., no., pp. 178- 182, 30 June-3 July 2002.



82. Yalandin, M.I.; Lyubutin, S.K.; Rukin, S.N.; Shpak, V.G.; Shunailov, S.A.; Slovikovsky, B.G.; , "Subnanosecond hybrid modulator for UWB and HPM applications," *Power Modulator Symposium, 2002 and 2002 High-Voltage Workshop. Conference Record of the Twenty-Fifth International* , vol., no., pp. 248- 251, 30 June-3 July 2002.
83. Pocha, M.D.; Druce, R.L.; , "35-kV GaAs subnanosecond photoconductive switches," *Electron Devices, IEEE Transactions on* , vol.37, no.12, pp.2486-2492, Dec 1990.
84. Yu. A. Kotov, G. A. Mesyats, S. N. Rukin et al., "A Novel Nanosecond Semiconductor Opening Switch for Megavolt Repetitive Pulsed Power Technology: Experiments and Applications," *Proc. 9<sup>th</sup> IEEE Pulsed Power Conf., Albuquerque, NM*, p. 134, 1993.
85. Engelko, A.; Bluhm, H.; , "Simulation of semiconductor opening switch physics," *Pulsed Power Plasma Science, 2001. IEEE Conference Record - Abstracts* , vol., no., pp.358, 2001.
86. Sanders, J.M.; Kuthi, A.; Yu-Hsuan Wu; Vernier, P.T.; Gundersen, M.A.; , "A linear, single-stage, nanosecond pulse generator for delivering intense electric fields to biological loads," *Dielectrics and Electrical Insulation, IEEE Transactions on*, vol.16, no.4, pp.1048-1054, August 2009.
87. Andras Kuthi, and Martin A. Gundersen, "High Voltage Nanosecond Pulse Generator Using Fast Recovery Diodes for Cell Electro-Manipulation," United States Patent, no. US 7,901,930 B2, March 8<sup>th</sup>, 2011.
88. Teramoto, Y.; Urakami, H.; Katsuki, S.; Namihira, T.; Akiyama, H.; , "Semiconductor opening switch based repetitive pulsed power generator," *Power Modulator Symposium, 2002 and 2002 High-Voltage Workshop. Conference Record of the Twenty-Fifth International* , vol., no., pp. 210- 213, 30 June-3 July 2002.
89. Gaudet, J.A.; Prather, W.D.; Burger, J.; Skipper, M.C.; Abdalla, M.D.; Mar, A.; O'Malley, M.W.; Zutavern, F.J.; Loubriel, G.M.; , "Progress in gallium arsenide photoconductive switch research for high power applications," *Power Modulator Symposium, 2002 and 2002 High-*

- Voltage Workshop. Conference Record of the Twenty-Fifth International* , vol., no., pp. 699-702, 30 June-3 July 2002.
90. Zutavern, F.J.; Loubriel, G.M.; Buttram, M.T.; O'Malley, M.W.; Helgeson, W.D.; McLaughlin, D.L.; , "High power light activated semiconductor switches with sub-nanosecond rise times," *Microwave Symposium Digest, 1991., IEEE MTT-S International* , vol., no., pp.377-380 vol.1, 10-14 Jul 1991.
  91. H. Bluhm, Pulsed Power Systems: Principles and Applications. Springer, 2006.
  92. Druce, R.L.; Pocha, M.D.; Griffin, K.L.; Hofer, W.W.; , "Subnanosecond linear GaAs photoconductive switching," *Pulsed Power Conference, 1989*, pp.882-886, 1989.
  93. Schoenbach, K.H.; Kenney, J.S.; Koenig, A.; Ocampo, B.J.; , "Electric Field Measurements In Photoconductive GaAs Switches," *Pulsed Power Conference, 1991. Digest of Technical Papers. Eighth IEEE International*, pp.105-108, 16-19 Jun 1991.
  94. Howson, P.A.; Miller, R.; Ryder, D.M.; , "Photoconductive switch design and applications," *Electrical Insulation, 1990., Conference Record of the 1990 IEEE International Symposium on*, pp.461-464, 3-6 Jun 1990.
  95. Buttram, M., "Some future directions for repetitive pulsed power," *Plasma Science, IEEE Transactions on* , vol.30, no.1, pp.262-266, Feb 2002.
  96. S. T. Pai and Qi Zhang, Introduction to High Power Pulse Technology. Series B: Physics, Vol. 89a. pp 12-22, 1995.
  97. G. Beziuk, "Subnanosecond Pulse Generator Operating with Arbitrary Load," *rev. sci. instrum.*, vol. 82, 2011.
  98. Frederick W. Grover, Inductance Calculations: Working Formulas and Tables, Dover Publications, Inc., New York, 1946.
  99. Levent Sevgi, "Transmission Line Fault Analysis Using a Matlab-Based Virtual Time Domain Reflectrometer Tool," IEEE, 2006.

100. Rene Seeberger, "Capacitance and Dissipation Factor Measurements," *IEEE Elec. Ins. Mag.*, vol. 2, pp. 27-36, January 1986.
101. Juergen F. Kolb, Susumu Kono, and Karl H. Schoenbach, "Nanosecond pulsed electric field generators for the study of subcellular effects," *Bioelectromagnetics*, vol. 27, 2006.
102. Hildebrandt, B, Wust, P., Ahlers, O., Dieing, A., Sreenivasa, G., Kerner, T., Felix, R., and Riess, H., "The Cellular and Molecular Basis of Hyperthermia," *Critical Reviews in Oncology Hematology*, vol. 43, pp.33-56, 2002.
103. T. C. Cetas, and R. B. Roemer, "Status and future developments in the physical aspects of hyperthermia," *Cancer Research*, vol. 44, pp.4894-4901, 1984.
104. I. Szabo, S. I. Alekseev, G. Acs, A. A. Radzievsky, M. K. Logani, V. R. Makar, O. R. Gordiienko, and M. C. Ziskin, "Destruction of cutaneous melanoma with millimeter wave hyperthermia in mice," *IEEE Trans. Plasma Science*, vol. 32, pp.1653-1660, 2004.
105. J. A. Dickson and S. K. Calderwood, "Temperature range and selective sensitivity of tumors to hyperthermia: A critical review," *Annals New York Academy of Sciences*, vol. 335, pp. 180-205, 1980.
106. P. Wust, B. Hildebrandt, G. Sreenivasa, B. Rau, J. Gellermann, H. Riess, R. Felix, and P. M. Schlag, "Hyperthermia in combined treatment of cancer," *The Lancet Oncology*, vol. 3, pp. 487-497, 2002.
107. Craig F. Bohren, "Comment on "Newton's Law of Cooling – A critical Assessment," [*Am. J. Phys.* Vol. 58, pp. 956-960, 1990]," *Am. J. Phys.*, vol. 59, no. 11, 1991.
108. E. E. Kunhardt and W. W. Byszewski, "Development of Overvoltage Breakdown at High Pressure." *Physical Review A*, Vol 21, No. 6, 1980.
109. W. W. Byszewski and G. Reinhold, "X-Ray Diagnostics of Runaway Electrons in Fast Gas Discharges." *Physical Review A*, vol 26, no. 5, 1982.
110. E. E. Kunhardt and Y. Tzeng, "Development of Electron Avalanche and its Transition Into Streamers." *Physical Review A*, vol 38, no. 3, 1988.

111. S. N. Ivanov, E. A. Litvinov and V. G. Shpak, "Initial Stages of Subnanosecond Electric Pulse Breakdown in High Pressure Gas Discharge Gaps." *Technical Physics Letters*, vol. 32, no. 9, pp. 745-749, 2006.
112. Frost, C.A.; Martin, T.H.; Patterson, P.E.; Rinehart, L.F.; Rohwein, G.J.; Roose, L.D.; Aurand, J.F.; , "ULTRAFast GAS SWITCHING EXPERIMENTS," *Pulsed Power Conference, 1993. Digest of Technical Papers. Ninth IEEE International* , vol.1, no., pp.491, 21-23 Jun 1993.
113. T.H. Martin, J.F. Seamen, and D.O. Jobe "Energy Losses in Switches." *Pulsed Power Conference, 1993. Digest of Technical Papers. Ninth IEEE International* , vol.1, no., pp.463, 21-23 Jun 1993.
114. S. N. Ivanov, V. V. Lisenkov and V. G. Shpak, "Electron Optical Study of the Initial Phase of Subnanosecond Pulsed Electric Breakdown of Gas Filled Gaps." *Technical Physics Letters*, Vol. 53, No 9, pp. 1162-1168, 2008.
115. Hasibur Rahaman, Byung-Joon Lee, Jürgen Urban, Robert Stark, Klaus Frank, S.H. Nam, "A spark gap switch with very high repetition rate." 28th ICPIG 2007.
116. A A Kulikovsky, "Positive Streamer Between Parallel Plate Electrodes in Atmospheric Pressure Air." *J. Phys. D: Appl. Phys.* 30 (1997), pp 441–450.
117. Moran, Stuart L.; Rinehart, Larry F.; , "Voltage Recovery Time of Small Spark Gaps," *Plasma Science, IEEE Transactions on* , vol.10, no.4, pp.277-280, Dec. 1982.
118. Liu, J.L.; Yin, Y.; Zhan, T.W.; Feng, J.H.; Zhong, H.H.; , "Application of a self-breakdown hydrogen spark gap switch on high power pulse modulator," *Pulsed Power Conference, 2007 16th IEEE International* , vol.1, no., pp.455-458, 17-22 June 2007.
119. Worts, E.J.; Kovaleski, S.D.; , "Particle-in-Cell Model of a Laser-Triggered Spark Gap," *Plasma Science, IEEE Transactions on* , vol.34, no.5, pp.1640-1645, Oct. 2006.
120. M. R. Barrault, and M. M. Kekez, "A simple subnanosecond spark gap." *J. Sci. Instrum.*, 1967, vol. 44.

121. Erich E. Kunhardt and Lawrence H. Luessen, Electrical Breakdown and Discharges in Gases. *Series B: Physics*, vol. 89a. pp 252-257, 1983.
122. Jean-Francois, "Longitudinal Profile and Effective Length of a Conventional Dipole Magnet." Particle Accelerator Conference Proceedings, (1993), vol.4, pp. 2901-2903.
123. J. D. Cobine, *Gaseous Conductors: Theory and Engineering Applications*. Dover, 1958.
124. Donaldson, A.L.; Kristiansen, M.; , "Electrode erosion as a function of electrode materials in high current, high energy transient arcs," *Pulsed Power Conference, 1989. 7th*, vol., no., pp.83-86, 1989
125. J. M. Koutsoubis and S. J. MacGregor, "Electrode Erosion and Lifetime Performance of a High Repetition Rate, Triggered, Corona-stabilized Switch in Air," *J. Phys. D: Appl. Phys.* **33** 1093, 2000.
126. A R Dick, S J MacGregor and R C Pate, "Transmission Line Switch Design for the Investigation for Subnanosecond Electrical Breakdown." *Meas. Sci. Technol.*, vol. 13, pp. 539-546, 2002.
127. Khan, S.H.; "The laser triggered spark gap," *Radio and Electronic Engineer*, vol.41, no.10, pp.475-480, October 1971.
128. Hutsel, B.T.; Benwell, A.; Kovalesski, S.D.; Kemp, M.A.; Sullivan, D.L.; Gahl, J.M.; , "Runtime and Jitter on a Laser-Triggered Spark-Gap Switch," *Plasma Science, IEEE Transactions on*, vol.36, no.5, pp.2541-2545, Oct. 2008.
129. Harjes, H. C.; Schonbach, K. H.; Kristiansen, M.; Guenther, A. H.; Hatfield, L. L.; , "Laser Triggering through Fiber Optics of a Low Jitter Spark Gap," *Plasma Science, IEEE Transactions on*, vol.8, no.3, pp.170-176, Sept. 1980.
130. Guo, R.; He, J.; Zhao, C.; Wu, C.; Pan, Y.; , "Study of a High-Power Rotary Arc Gap Switch," *Plasma Science, IEEE Transactions on* , vol.39, no.1, pp.279-284, Jan. 2011.

131. Geun-Hie Rim; Chu-Hyun Cho; Pavlov, E.P.; , "Design and testing of a rotary arc gap switch for pulsed power," *Pulsed Power Conference, 1999. Digest of Technical Papers. 12th IEEE International* , vol.1, no., pp.219-223 vol.1, 1999.
132. Kil-Soo Seo; Tae-Ho Lee; Lee-Ho Hwang; Hee-Jin Kim; Hong-Sik Lee; Geun-Hie Rim; , "A high power vacuum rotary arc gap closing switch for pulsed power applications," *Power Modulator Symposium, 2002 and 2002 High-Voltage Workshop. Conference Record of the Twenty-Fifth International*, pp. 366- 369, 30 June-3 July 2002.
133. Moran, S.L.; Hardesty, L.W.; , "High-repetition-rate hydrogen spark gap," *Power Modulator Symposium, 1990., IEEE Conference Record of the 1990 Nineteenth*, pp.227-231, 26-28 Jun 1990.
134. Yin, Y.; Liu, J.L.; Zhong, H.H.; Feng, J.H.; , "Experimental study of the voltage recovery characteristics of spark gap switch with different gases," *Pulsed Power Conference, 2007 16th IEEE International* , vol.1, pp.459-463, 17-22 June 2007.
135. A. Garner, G. Chen, N. Chen, V. Sridhara, J. Kolb, R. Swanson, S.Beebe, R. Joshi, and K. Schoenbach, "Ultrashort electric pulse induced changes in cellular dielectric properties", *Biochemical and Biophysical Research Communications*, vol. 362, pp. 139-144, 2007.
136. N. Hager III, "Broadband time domain reflectometry dielectric spectroscopy using variable time scale sampling," *Review of Scientific Instruments*, vol. 65, p. 887, 1994.
137. Qin Hu, Viswanadham Sridhara, Ravindra P. Joshi, Juergen F. Kolb, and Karl H. Schoenbach, "Molecular Dynamics Analysis of High Electric Pulse Effects on Bilayer Membranes Containing DPPC and DPPS," *IEEE Trans. on Plasma Sci.*, vol. 34, no. 4, pp. 1405-1411, 2006.
138. Berendsen HJC, van der Spoel D, van Drunen R (1995) Gromacs: a message-passing parallel molecular dynamics implementation. *Comput. Phys. Commun.* 91:43–56.
139. Lindahl E, Hess B, van der Spoel D (2001) A package for molecular simulation and trajectory analysis. *J. Mol. Model.* 7:306–317.

140. Kroemer G, Galluzzi L, Vandenabeele P, Abrams J, Alnemri ES, Baehrecke EH, Blagosklonny MV, El-Deiry WS, Golstein P, Green DR, Hengartner M, Knight RA, Kumar S, Lipton SA, Malorni W, Nunez G, Peter ME, Tschopp J, Yuan J, Piacentini M, Zhivotovsky B, Melino G; Nomenclature Committee on Cell Death 2009. Classification of cell death: recommendations of the Nomenclature Committee on Cell Death 2009. *Cell Death Differ.* 2009 Jan;16 (1):3-11. Epub 2008 Oct 10.
141. Sun-Joo Lee, Yuhua Song, Nathan A. Baker, "Molecular Dynamics Simulations of Asymmetric NaCl and KCl Solutions Separated by Phosphatidylcholine Bilayers: Potential Drops and Structural Changes Induced by Strong Na<sup>+</sup>-Lipid Interactions and Finite Size Effects," *Biophys. J.*, vol. 94, pp. 3565 – 3576, 2008.
142. Andrey A. Gurtovenko, "Asymmetry of Lipid Bilayers Induced by Monovalent Salt: Atomistic Molecular-Dynamics Study," *J. Chem. Phys.*, vol. 122, pp. 244902, 2005.
143. Andrey A. Gurtovenko, and Ilpo Vattulainen, "Lipid Transmembrane Asymmetry and Intrinsic Membrane Potential: Two Sides of the Same Coin" *J. Am. Chem. Soc.*, vol. 129, pp. 5358-5359, 2007.
144. W. Frey, J.A. White, R.O. Price, P.F. Blackmore, R.P. Joshi, R. Nuccitelli, S.J. Beebe, K.H. Schoenbach, and J.F. Kolb, "Plasma Membrane Voltage Changes During Nanosecond Pulsed Electric Field Exposure," *Biophys. J.* vol. 90, pp. 3608-3615, 2006.
145. A. Blicher, K. Wodzinska, M. Fidorra, M. Winterhalter, and T. Heimburg, The temperature dependence of lipid membrane permeability, its quantized nature, and the influence of anesthetics, *Biophysical Journal*, v 96, pp. 4581-4591, June 2009.

## APPENDIX A

### NANO AND SUBNANOSECOND SPARK GAP SWITCHES

The switch is of critical importance in any pulsed power device, in that energy needs to be transferred from the pulse forming network to the load with high efficiency and reproducibility. The spark gap switch possesses many characteristics that are well suited for high pulsed power applications. These characteristics include a wide voltage range and large current handling capabilities (into the MV and MA range), wide range of energy transferring capabilities (mJ – MJ), simple design/construction, closing times reaching into the picosecond range, and ease of adjustment of the parameters of the switch (gas pressure, gap spacing, trigger timing, etc.). The disadvantages are the limited number of pulses ( $10^4$  -  $10^6$ ) due to erosion of the electrodes, low repetition rate due to the slow recovery of the ionized gas, and high jitter (100's ns) associated with spontaneous breakdowns. Jitter is defined in the variation of time (runtime) between the triggering of the switch and the breakdown of the switch. This appendix is an overview of the criteria needed to design spark gap switches capable of creating breakdowns in the subnanosecond regime.

#### A.1 INITIATION OF SUBNANOSECOND BREAKDOWN

The initiation of breakdown (gas transformation from insulating to conducting stage) for a spark gap begins with an applied voltage across the gap so that the electric field across the gap reaches a threshold needed to induce ionization of the gas within the gap. The ionization causes an electron avalanche to begin at the cathode, which is followed by the formation of a streamer towards the anode which eventually leads to breakdown. From Paschen's Law, the DC breakdown voltage in air can be approximated by

$$V_{bd} = B \cdot [P \cdot d / \ln(A \cdot P \cdot d)] \quad \text{A.1}$$



in which  $A$  is equal to  $15.2 \text{ (cm·torr)}^{-1}$  and  $B$  is equal to  $370 \text{ V·(cm·torr)}^{-1}$  [96]. The condition of the gap prior to breakdown can be characterized by the ratio of the electric field across the gap to the density of the gas within the gap,  $E/n$ . The  $E/n$  ratio is known as the Townsend coefficient, and is given in units of Td where  $1 \text{ Td} = 10^{-17} \text{ Vcm}^2$ . For air, the DC breakdown voltage is approximately 31 kV/cm, which equates to a Townsend coefficient of 13 Td.

The time lag, which is the time it takes for a gap to break down once it reaches the DC breakdown voltage, is inversely proportional to the risetime of the pulse. A faster risetime across the gap will allow for a higher voltage across the gap before breakdown is initiated. This overvoltage allows the electric field between the electrodes of the switch to reach to a high enough  $E/n$  value to create the conditions for runaway electrons, which are necessary for subnanosecond breakdown times. Runaway electrons are a small percentage of electrons which acquire enough energy ( $> 3 \times$  Ionization energy) to surpass the ionization energy of its respective gas to move past the head of the avalanche, which eventually lead to the creation of new electron avalanches [108, 109].

Streamers are mainly created by photoionization in DC breakdown conditions, but can additionally be created by runaway electrons at breakdown strengths above DC conditions. Through numerical simulations based on electron kinetics, Kunhardt et al. determined the minimum voltage needed to create conditions for runaway electrons is at least 20% of the DC breakdown voltage [108, 110], which would equate to a Townsend coefficient of 15 Td for air. To create such conditions, the voltage across the switch must increase at a high enough rate so that the delay time between the time the voltage reaches the DC breakdown voltage and the time the switch breaks down is long enough to allow the voltage at which the switch breaks down to reach values at least 20% higher than the DC breakdown voltage [108]. Electrons existing in the injection region (Fig. A.1) acquire the energy needed to surpass the maximum cross section value for ionization. The injection region is the region with the avalanche in which the electric field,

due to space charges, is increasing. This energy is greater than  $3 \epsilon_i$  to  $5 \epsilon_i$  where  $\epsilon_i$  is the ionization energy [108, 109].

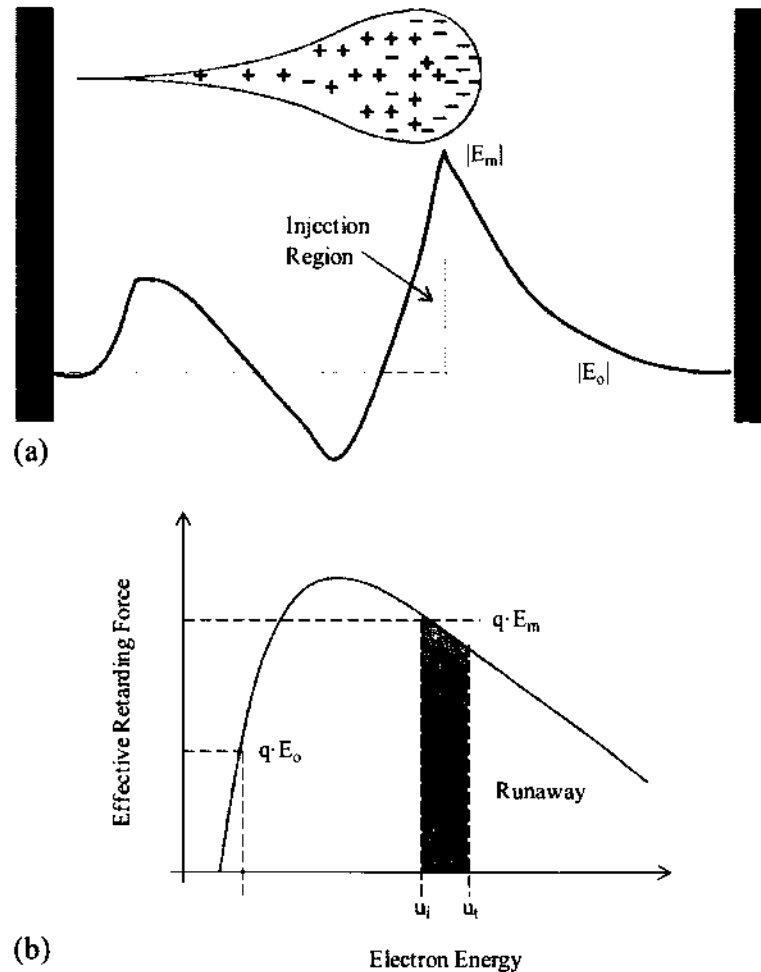


Fig. A.1. (a) Electric field distribution in an electron avalanche. The external electric field across the gap is represented by the dashed line,  $E_0$ . The space charge between the positive ions in the avalanche and the electrons at the head of the avalanche create a high electric field within the head of the avalanche, which decreases exponentially at the head. The injection region is the space in which the electric field increases up to  $E_m$ . Electrons in this region acquire enough energy to surpass the ionization energy such that the electron passes ahead of the avalanche in which the electric field decreases.

These electrons will move ahead of the head of the avalanche, in which, depending on their energy, they may get trapped [108]. The trapped region exists where the electric field begins to decrease from the maximum value achieved with the local space charge [108]. Trapping occurs when the energy gained by the electrons is less than the energy lost due to collisions with other

particles (retarding forces). The retarding force increases with increasing gap pressure. Therefore, the electric field must also increase to allow the electrons to gain sufficient energy to overcome the retarding force. Trapped electrons begin a new avalanche in front of the existing avalanche. The field in the center of the head is the strongest, which suggests most of the runaway electrons will be centered in the avalanche causing newer avalanches to be created in the center [108, 110]. In effect, this centering narrows the head of the avalanche and enhances the field even more which creates more runaway electrons. The process then repeats itself and is much faster than a normal avalanche formation.

A breakdown voltage of 20% greater than DC breakdown is still not sufficient for subnanosecond breakdown conditions [108, 111]. Subnanosecond breakdown requires a percentage of electrons to avoid becoming trapped for reasons which will be discussed shortly. Kunhardt et al. determined that in order for a percentage of the runaway electrons to acquire enough energy to avoid becoming trapped, the breakdown voltage needs to be greater than three times the DC breakdown voltage [108]. A 300% increase in the DC breakdown voltage would put the Townsend coefficient, for air, at 38 Td at a pressure of 1 atm. Un-trapped Electrons are able to move even farther away from the main avalanche chain, until they lose enough energy to start their own avalanches away from the main column, resulting in a multichannel and/or diffused discharge [108, 112, 113].

An avalanche chain is known as a streamer. Photoionization is also taking place and avalanches can form outside the center of the primary avalanche cone. In high enough electric fields, photoionization of atoms can lead to new avalanches outside the primary streamer, and these avalanches also undergo the runaway electron process, which also contributes to the diffused discharge [108]. A diffused and/or multichannel discharge has a faster decrease in resistance of the channel than a single filamentary discharge. This acts as a channel with a radius that grows larger at a faster rate than a normal streamer breakdown. As a result, the rise time in the current is decreased, leading to a faster switch.

In order to create runaway electrons, the ratio must be on the order of 40 Td or greater in gases including air, nitrogen, helium, hydrogen and SF<sub>6</sub> [108-111, 114]. The ratio is proportional to the risetime in that a higher ratio leads to a faster rise time (or breakdown time). A smaller gap distance gives larger values of E/n which results in shorter risetime with an increase in amplitude. As the gap distance of the electrode decreases further (< 0.5 mm), the time lag decreases, which decreases the breakdown voltage across the gap, thus decreasing E/n. Therefore, there is an optimum gap distance of a spark gap switch depending on the voltage across the switch.

## A.2 BREAKDOWN

The formation of the streamer is not the breakdown of a spark gap switch. Whether the streamer is formed from photoionization or runaway electrons, the breakdown mechanism is the same in each case. The streamer is made of free electrons and ions, in which the electrons move towards the head of the avalanche while the positive ions remain behind due to their low mobilities. When the head of the streamer reaches the anode, it creates a conductive channel having the same potential as the anode [115]. This creates a high electric field strength between the tail of the streamer and the cathode. As the streamer grows toward the cathode, the electric field between the tip of the streamer and the cathode increases. Eventually, the electric field is strong enough to pull electrons off the cathode, at which point, the streamer makes contact with the cathode, and the potential of the gap drops at a speed related to the change of the inductance and resistance of the plasma channel [116].

Once the streamer is connected to both electrodes, a highly resistive conduction channel, also known as a filament, (k $\Omega$  range) with radius on the order of 10<sup>-2</sup> mm exists between the cathode and anode. The increase of electrons from the cathode cause the channel to heat up, which in turn expands the channel, decreasing the resistance. This change in resistance is the defined breakdown of the switch in which the current rises, and the voltage across the switch

drops. The change in the radius of the plasma causes a pressure gradient within the gas, which leads to a popping noise associated with all electrical breakdowns [113]. The change in the radius was experimentally determined by Martin et al., for five different gases: Hydrogen, Helium, Air, Nitrogen, and SF<sub>6</sub> [113].

$$r(t)^2 = \left( \frac{4}{\pi^2 \cdot \rho \cdot \xi \cdot \sigma} \right)^{\frac{1}{3}} \cdot \int_0^t \frac{2}{I^3} dt + r(0)^2 \quad A.2$$

$I$  is the current,  $\rho$  is the density of gas, and Zeta is a given constant (4.5 for hydrogen), and  $r(0)$  is the radius of the channel before expansion [113]. At time 0, the radius of the channel can be approximated by the avalanche head size as given in (A.3) [117].

$$r_a = \left( \frac{3 \cdot q}{4 \cdot \pi \cdot \varepsilon \cdot E_o} \right)^{\frac{1}{3}} \cdot e^{\frac{\alpha \cdot d}{3}} \quad A.3$$

The number of ions per cm created by electrons is denoted  $\alpha$ . By increasing the pressure (effectively increasing  $n$ ), breakdown channels will have smaller radii, resulting in a more filamentary type of discharge. However, if the switch is overvoltaged, the electric field,  $E$ , will also increase, resulting in a constant or increased  $E/n$  value. Such an increase may lead to multichannel discharges, or diffused discharges. For a multichannel discharge, the radius is estimated by (A.2) multiplied by the number of channels [112, 113]. The number of channels,  $N$ , can be approximated by determining the resistance of a single channel and decreasing the resistance by  $N$  until the resistance is less than 1  $\Omega$ .

Assuming that the breakdown occurs in a single filament, the temporal development of the resistance and inductance can be obtained using the Braginskii model of the spark channel. In this model, the conductivity of the plasma is assumed to remain constant while joule heating causes pressure, which increases the radius of the gap. As the radius increases, the resistance of the channel decreases. The current during the rise of the pulse can be expressed as:

$$I(t) = K \cdot t \quad \text{A.4}$$

where K is equal to the slope of the current rise, A/s. The conductivity can be calculated with:

$$\sigma = \rho \cdot q \cdot \mu \quad \text{A.5}$$

in which q is the charge of an electron and  $\mu$  is the mobility of the electron in the plasma. The conductivity of air is  $200 \text{ mho} \cdot \text{cm}^{-1}$  [113]. The resistance of this single channel can be calculated by:

$$R(t) = d / \pi \cdot \sigma \cdot r(t)^2 \quad \text{A.6}$$

where d is the gap distance of the switch, and the time dependent radius of the gap can be expressed with (A.2). In order to meet the criteria for breakdown, the resistance of the gap should be much lower than the load resistance (typically  $50 \Omega$ ). A good approximation to determine the radius of the channel is to assume  $R(t) < 1 \Omega$  and solve for  $r(t)$ . The number of channels can then be approximated by  $R(t = 0)/1 \Omega$ .

A faster decrease in the resistance of the plasma channel accounts for a fast risetime of the switch. Martin et al. compared the energy delivered to the switch to the time it takes the switch to go from an infinite load to zero [113]:

$$E = \frac{1}{4} \cdot V_{peak} \cdot I_{peak} \cdot t_r \quad \text{A.7}$$

For air,  $\text{H}_2$ ,  $\text{SF}_6$ , and He, Martin et al. experimentally determined the risetime of the switch to be equal to:

$$t_r = 88 \cdot \sqrt{\rho} / (Z \cdot E^4)^{1/3} \quad \text{A.8}$$

where  $\rho$  is the ratio of the density of the gas and the density of the gas under normal conditions (1 atm, 300 K), Z is the matched impedance of the load, and E is the electric field between the switch before breakdown [113, 118]. According to (A.5), a decrease in the gas density will result

in a faster risetime. This was confirmed by Liu et al., by comparing the risetime of a spark gap with  $H_2$ ,  $N_2$ , and  $SF_6$  [118]. The electrode gap spacing was 27.4 mm, and the breakdown voltage was equal to 400 kV. The pressures of the gases were adjusted to match the same breakdown voltage. The risetime of  $H_2$ ,  $N_2$ , and  $SF_6$  were 8, 11.2, and 12.8 ns respectively. After pressurization, the density of the corresponding gases were in increasing order [118]. The decrease in risetime is most likely due to an increase in the radius of the channel as expected in (A.2), in which the radius is proportional to  $(1/\sigma)^{1/6}$ .

### A.6 CIRCUIT PARAMETERS

The ideal switch has a voltage fall time of zero, with zero resistance, inductance, and capacitance. The capacitance of the non-ideal switch can be calculated by the geometry of the switch (gap distance, electrode surface area, electrode shape). The inductance is proportional to the length of the spark (distance between electrodes,  $d$ ) multiplied by the log of the ratio of the length and radius of the spark [119].

$$L = \frac{\mu \cdot d}{2 \cdot \pi} \cdot \ln\left(\frac{d}{r(t)}\right) \quad A.9$$

The resistance of the channel is proportional to the length of the spark ( $d$ ) and the reciprocal of the square of the radius of the channel, and is described by (A.6). The conductivity ( $\sigma$ ) is assumed to be constant, and for air, helium and nitrogen at 1 atm has values of 200, 140, and 300 mho-cm respectively [113]. The circuit components make up a series RLC circuit as shown in Fig. A.2 [112, 120].

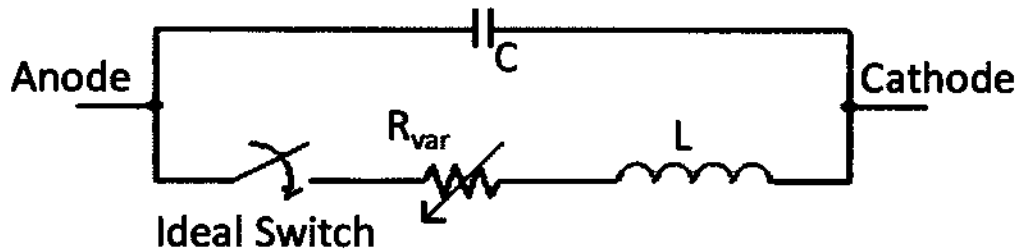


Fig. A.2. Circuit model of a spark gap

The change in resistance depends on the speed at which the plasma channel increases during the breakdown process. Figure A.3 shows the voltage across a load connected to a DC voltage source with an ideal and non-ideal switch. The light gray trace represents an ideal switch, and the overdamped and underdamped switch are in black and dark gray, respectively. Overdamped or underdamped switches occur when the resistance of the channel is larger than or smaller than  $2\sqrt{L/C}$ , respectively. A critically damped switch will provide the fastest risetime without oscillation. For a critically damped switch, the resistance equals  $2\sqrt{L/C}$ , and the risetime can be approximated by  $\sqrt{LC}/2$ .

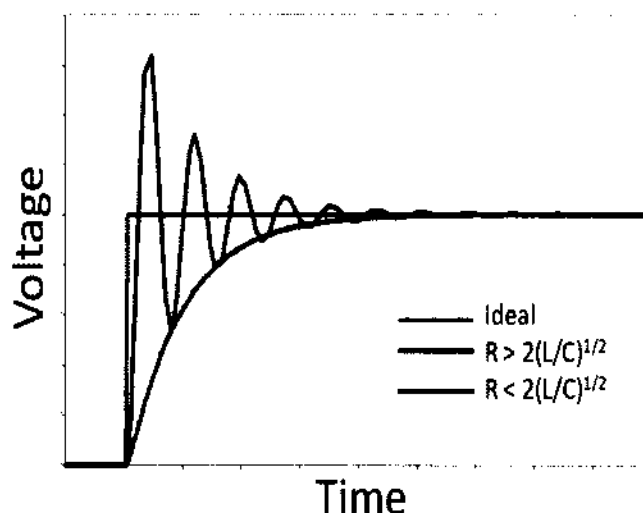


Fig. A.3. Electrical characteristic of a spark gap. The gray trace represents an ideal switch, while the dark gray represents an inductive switch, and the black trace a capacitive switch.

As shown with the circuit analysis, a spark gap switch with a long gap would create an oscillation due to the large inductance and small capacitance. A switch with a large electrode surface area and a small gap would create a damping effect due to a small inductance and large capacitance. To create a fast switch, a small gap distance as well as electrodes with a small surface area are needed to minimize both the capacitance and inductance. The inductance is also reduced as a



result of a multiple channel discharge, which occurs for high electric fields and is also a direct result of a small gap distance at high voltages.

Oscillations can also be dampened for a given switch by decreasing the pressure [120].

The conductivity of an ideal plasma is given by [119]:

$$\sigma = \frac{n \cdot q^2}{m \cdot \nu} \quad \text{A.10}$$

In (A.10)  $q$  is the electron charge,  $m$  is the electron mass,  $\nu$  is the collision frequency, and  $n$  is the gas density, which is decreased by decreasing the pressure. A decrease in the gas density causes an increase in the resistance of the plasma, (5.5), which effectively dampens the oscillations. This dampening in the oscillations by decreasing the pressure of the gas was experimentally shown for nitrogen at pressures of 5, 3, and 1 atm [120]. The voltage was adjusted to allow for the same amplitude (2 kV, 20 ns FWHM, < 5 ns rise time).

## A.5 ELECTRODE SHAPE AND MATERIAL

Flat electrodes create higher electric fields at the edges, while pin electrodes create high electric fields at the tips. Such field enhancing geometries may cause a high enough electric field to decrease the time lag, causing the voltage of the gap to break down at or before the DC breakdown voltage [121]. The ideal electrode shape is designed to create a uniform electric field within the gap while minimizing edge effects which can lead breakdown below the desired level by corona discharges. Two common electrode shapes which are derived from the equipotential lines from two finite parallel planes are the Rogowski and Borda profile [122, 123]. Rogowski performed the experiments for such a profile and found that setting  $\nu = \pi/2$  (equipotential line) resulted in the maximum field being homogenous in the center and decreasing monotonically within the curvature of the potential line. This allows for repetitive breakdown with minimal erosion and no unwanted breakdown around the edges. This geometry also has the most compact

shape [122, 123]. The Borda profile has less of a flat surface and more of a curvature on the corners. This reduces the side electric field compared to Rogowski profile [122].

The durability of the switch is mainly governed by the electrode material. Electrodes with higher thermal and electrical conductivities, higher melting temperatures (or temperatures in which there is a significant reduction in thermal strength), and higher densities will be more durable to erosion caused by local heating at the electrode due to the plasma channel [124]. Koutsoubis and MacGregor performed several durability tests on brass, stainless steel, aluminum and elkonite by comparing the lifetime of the switch at two repetition rates of the pulses (10 Hz vs. 1 kHz) [125]. At 10 Hz, the amount of erosion, in increasing order, was elkonite, brass, ss, and Al. The lifetime of the switch with different material at 10 Hz in decreasing order was elkonite (0.7 million), followed by brass (0.5 million), stainless steel (0.3 million), and aluminum (0.2 million). At 1 kHz, the amount of erosion in increasing order was brass, Al, ss, and elkonite. In fact, the erosion at a higher frequency decreased for the brass and aluminum. The decreased erosion was due to the formation of a thin layer of oxides on the surface of the electrodes ( $\text{Al}_2\text{O}_3$  on the aluminum and  $\text{ZnO}$  on the brass), which have much higher melting temperatures than brass and aluminum. The lifetime of each material increased: brass (2.1 million), aluminum (1.8 million), stainless steel (1.6 million) and elkonite (1.3 million). The formation of the oxides is temperature dependent in that a higher temperature on the surface of the electrode will result in more of a build up of the oxide layer. At low repetition rates, the amount of erosion and/or lifetime of the switch was determined by the electrical and thermal properties of the metal; whereas the lifetime is determined by the thermal properties of the metallic oxides formed on the electrodes [125]. A higher temperature is associated with a higher repetition rate. Stainless steel performed poorly at a higher repetition rate mainly due to the lower electrical and thermal conductivities than the other metals. Brass exhibited a better overall performance while stainless steel exhibited the poorest performance.

## A.7 OPTIMIZATION OF SPARK GAP FOR SUB-NS BREAKDOWN

In order for a spark gap switch to achieve a breakdown time in the subnanosecond regime, the resistance and inductance of the plasma channel during the breakdown process need to decrease at a rate which leads to a subnanosecond current risetime across the switch. Subnanosecond breakdown is accomplished by creating conditions which allow for a diffused or multichannel discharge, which is characteristic for multiple avalanches created by runaway electrons as well as photoionization. To create such conditions, high  $E/n$  ratios, on the order of 40 Td, are required.

In order to avoid heavy damping, or oscillations, the geometry of the spark gap must be designed to reduce both the capacitance of the gap and the inductance of the channel. The reduction of the capacitance and inductance is accomplished by using a small gap distance (decreases inductance) and reducing the electrode surface area (reduces capacitance).

Decreasing the gap distance will decrease the breakdown voltage which leads to a decrease in  $E/n$ . Three techniques are used together to increase the breakdown voltage, which increases  $E/n$ . The first technique is to pressurize the spark gap which will increase the DC breakdown voltage. The second technique is to use a charging circuit (Marx Bank, square wave pulse generator, etc.) in order to increase the voltage rate across the switch which allows the breakdown voltage to reach values above the DC breakdown voltage. A third approach to increase  $E/n$  is to pressurize the spark gap with a gas of lower density than air, such as hydrogen. This approach will also decrease the resistance of the single filaments by increasing the radius according to (A.2). The electrodes need a Rogowski type profile to prevent premature breakdown which is characteristic of sharp electrodes.

The following design criteria were used by Frost et al., and were able to create a spark gap switch capable of switching a 120 kV pulse in which the risetime of the current through the switch was less than 100 ps [112]. The gap distance was 0.7 mm, and the switch was pressurized at 120 psi with Hydrogen. The charging circuit supplied a pulse with a risetime of 2 ns. The

resulting  $E/n$  ratio before breakdown was 86 Td. With an  $E/n$  ratio between 30 Td and 60 Td, other groups were able to achieve risetimes between 900 ps and 400 ps [108-111, 114, 126].

## **A.5 COMPARISON TO OTHER SUBNANOSECOND SWITCHES**

Pulsed power applications have increasing demands for switches with low jitter ( $< \text{ns}$ ), fast repetition rate (kHz – MHz) and long life times ( $> 10^9$  pulses). Due to the disadvantages of the spark gap listed in the introduction to this appendix, spark gaps are unable to compete with semiconductor high power switches such as the SOS switch, photoconductive switches and avalanche transistors for pulsed power applications requiring such conditions [75, 81, 92].

Avalanche transistors are capable of switching in the 100 ps regime and can hold off voltages in the 10's of kV. Voltages in the 100's of kV can be achieved if the transistors are placed in series [75, 78]. The repetition rate of a pulse generator using avalanche transistors has reached up to 200 kHz [78].

Pulse generators incorporating SOS switches have been developed capable of delivering pulses with amplitudes in the 100's of kV range with sub 200 ps rise times, and repetition rates in the 10's of kHz [75, 81, 82]. The life time of SOS switches has been reported to be in the  $10^{11}$  range [85].

Photoconductive switches are capable of delivering 10's of kV with sub 200 ps rise times at a frequency rate in the 10's of kHz [83, 92]. The jitter of the photoconductive switch is less than 10 ps, which is the distinct advantage over the other semiconductor switches in which the jitter is in the 10's to 100's of ps. However, the repetition rate may be limited by the repetition rate of the laser trigger which can be in the 10's of Hz [92]. The life time of photoconductive switches can reach up to  $10^{11}$  pulses [83]. Photoconductive switches have one advantage over the other semiconductor switches: the use of optical triggering rather than electrical triggering. The optical isolation of the trigger source does not require protective circuitry.

The distinct advantage of spark gaps over semiconductor switches is the ability of the spark gap to deliver repetitive pulses with energies ranging from the  $\mu\text{J}$  to the MJ. The basic design of the spark gap is very simple and can be manipulated in a number of different ways to operate for a specific application (size, gas type and pressure, gap distance, electrode shape and material, etc.). Such adjustments for semiconductor switches (SOS and avalanche transistors) would require a change in the circuitry.

Several mechanisms have also been incorporated with spark gaps in order to reduce the runtime and jitter of the switch, the repetition rate, and the lifetime. Both the jitter and runtime of the switch can be decreased by triggering the spark gap, electrically and/or optically, at or below the DC breakdown voltage. Laser triggering has been used to decrease the runtime and jitter of the spark gap to values on the order of 10 ns and 1 ns, respectively [127, 128]. By triggering a spark gap at voltages of 80% of the DC breakdown voltage, jitter under 1 ns has been achieved [128, 129]. The energy required from the laser to breakdown the spark gap (mJ) is on the same order needed to induce breakdown of the photoconductive switch in linear mode. However, much higher voltages with the spark gap can be achieved (100's kV) opposed to the photoconductive switch (10's kV). Rotary arc switches are used to increase the lifetime of the switch, as well as to deliver energies up to 500 kJ [130-132]. The repetition rate of the spark gap can be increased by pressurizing the gas, and using a gas with a high thermal diffusivity, such as hydrogen [117, 133, 134]. Repetition rates in the 100's kHz range have been achieved by pressuring the switch with 1,000 psi of Hydrogen [133, 134].

## APPENDIX B

### MEASUREMENTS OF THE ELECTRICAL PROPERTIES OF CELLS BY MEANS OF DIELECTRIC SPECTROSCOPY

In order to measure the conductivity and permittivity of the Hepa 1-6 cell and the growth medium, and their dependence on temperature, Time Domain Reflectometry (TDR) Dielectric Spectroscopy analysis was used [49, 51, 135, 136]. TDR gives the dispersion relation for both the conductivity and permittivity of a sample from the reflected signal of a known transmitted signal. The diagram of TDR is shown in Fig. B.1.

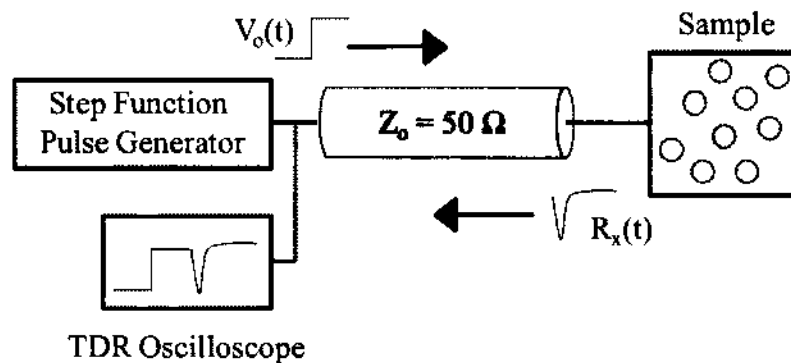


Fig. B.1. Diagram of the TDR dielectric spectroscopy system. A step function,  $V_o(t)$ , is fed into the transmission line, which is terminated with a sensor containing the sample. The reflected signal,  $R_x(t)$ , is used to determine the complex permittivity of the sample. Not shown in the figure is a sampling head before the oscilloscope which digitizes the reflected signal before storing into the oscilloscope [51].

A pulse generator sends a voltage pulse, of known risetime and amplitude, into a transmission line of impedance  $Z_o$  ( $50 \Omega$ ) in which the end of the line is terminated with a coaxial sensor containing the sample. The dimensions of the sample can be obtained from [51]. The reflection coefficient,  $\rho$ , is based upon the reflected signal of an open sensor and is used to determine the complex permittivity of the sample [51],

$$\epsilon^* = [1 + \rho / (s \cdot Z_o \cdot C_o)] / [1 + \rho \cdot s \cdot Z_o \cdot C_o] \quad \text{B.1}$$

The capacitance,  $C_0$ , is the capacitance of the empty chamber, and  $s = j\omega$ . The reflection coefficient is defined as [51]:

$$\rho = (v_r - v_x)/(v_r + v_x) \quad \text{B.2}$$

in which  $v_r$  and  $v_x$  are the Fourier transform of the empty sensor reflection and load sensor reflection, respectively. This technique is used since it is easier to distinguish, in time, the reflected signal from the sample to the reflected signal of an empty sensor [18]. The relative permittivity ( $\epsilon_r$ ) and conductivity ( $\sigma$ ) of the sample can then be determined from the complex permittivity [49]:

$$\epsilon^* = \epsilon_r - j \cdot \sigma / (\epsilon_0 \cdot \omega) \quad \text{B.3}$$

The complex permittivity of the suspension ( $\epsilon^*_{sup}$ ) and of the cells ( $\epsilon^*_{cell}$ ) is determined by using the Maxwell-Wagner model [49]:

$$\epsilon^* = \epsilon^*_{sup} \cdot \frac{2 \cdot (1-p) \cdot \epsilon^*_{sup} + (1+2 \cdot p) \cdot \epsilon^*_{cell}}{(2+p) \cdot \epsilon^*_{sup} + (1-p) \cdot \epsilon^*_{cell}} \quad \text{B.4}$$

in which  $p$  is the volume fraction of cells in the suspension. Once the complex permittivity of the cell is determined, the cell can be broken down further in order to determine the complex permittivities of the cell cytoplasm ( $\epsilon^*_{cp}$ ) and membrane ( $\epsilon^*_m$ ) [49].

$$\epsilon^*_{cell} = \epsilon^*_m \cdot \frac{2 \cdot (1-v) \cdot \epsilon^*_m + (1+2 \cdot v) \cdot \epsilon^*_{cp}}{(2+v) \cdot \epsilon^*_m + (1-v) \cdot \epsilon^*_{cp}} \quad \text{B.5}$$

The thickness of the membrane ( $d$ ) and radius of the cell ( $R$ ) is accounted for in  $v$ , in which  $v = (1-d/R)^3$ . Similarly, in order to find the relative permittivity and conductivity of the different parts of the cell, (B.3) is used.

An Agilent 86100C TDR oscilloscope together with a 54754A differential plug-in was used. A cutoff type termination-sensor with gold-plated stainless steel electrodes was used to hold

cell suspensions with a 10% volume fraction. In order to minimize the effect of electrode polarization, the cells were suspended in a low conductivity buffer as suggested by previous studies [135]. The incident voltage pulse is generated by the differential plug-in with 35-ps rise time and 200-mV amplitude. The same module also receives the reflected signal with an 18-GHz detection bandwidth. The temperature was controlled by immersing the sensor in a water bath with a thermostat (Julabo, San Diego, CA). The complex permittivity of the sample was calculated by running a Laplace transform of the incident and reflected signals as suggested by Hager [136]. The relative permittivity and conductivity of the sample was further determined from the complex permittivity. After correction for electrode polarization [51], the permittivity and conductivity spectra of the cell suspension were fitted in a combination of the Maxwell-Wagner mixture model and a single-shell cell dielectric model with the knowledge of the cell. The dielectric properties of each cellular structure can be derived as fitting parameters when the cell geometry values are known (cell radius and membrane thickness).

The measured conductivity and permittivity of the cytoplasm and plasma membrane derived by TDR analysis with respect to temperature are shown in Table B.1. It is worth noting that the buffer (medium) used in dielectric spectroscopy to determine the electrical properties of the cell has a much lower conductivity than the cell culture medium.



Relative Permittivity				
Temperature	Membrane		Cytoplasm	
	Avg.	Std.	Avg.	Std.
25°C	13.9	0.19	76.3	2.6
37°C	15.1	0.31	100	1.5
42°C	16.5	0.64	115	4.9
47°C	18	0.17	146	4.8

Conductivity				
Temperature	Membrane [10 <sup>-5</sup> S/m]		Cytoplasm [10 <sup>-1</sup> S/m]	
	Avg.	Std.	Avg.	Std.
25°C	2.44	0.28	3.79	0.08
37°C	4.05	0.13	4.53	0.07
42°C	5.13	0.24	4.73	0.27
47°C	9.21	0.21	5.1	0.23

Table B.1. Permittivity (a) and conductivity (b) of cytoplasm and plasma membranes of Hepa 1-6 cells at 25°C, 37°C, 42°C and 47°C [48].

The change in conductivity of the cytoplasm for the same temperature rise is 34%. However, the temperature effect on the plasma membrane conductivity is much more pronounced: it increases by 270% when the temperature is increased from 25°C to 47°C. The permittivity of the cytoplasm and plasma membrane of Hepa 1-6 cells increases by approximately 90%, and 30%, when the temperature is raised from 25°C to 47°C, respectively.

## APPENDIX C

### MOLECULAR DYNAMICS SIMULATION APPROACH

Simulation studies of membrane electroporation under a constant applied voltage were carried out as an example of a bio-process affected by both the electric field and temperature [48]. The poration process was modeled through atomistic Molecular Dynamic (MD) simulations. The MD technique allows for the inclusion and collection of particles and their respected potentials at the nanoscale level, allowing for natural fluctuations, self consistent calculations without fitting parameters, and ease of allowing complex geometries [137]. With MD simulations, the use of mean-field approximation is not required. The MD simulations use classical Newtonian mechanics to simulate the dynamical movement of neutral atoms and ions taking account for the many body interactions between them [137]. The realistic molecular representation of the molecules is also constructed into the simulation. A more detailed discussion on MD simulations can be found in [6, 137].

This MD technique allows for the simulation of a membrane patch from which one can ascertain whether pore formation can occur within a certain time at a chosen value of external field and fixed temperature. The GROMACS package [138, 139] was used for the MD simulations of membrane effects at different temperatures. The GROMACS tool provides the force fields for the lipid membrane, which was assumed to comprise dipalmitoyl-phosphatidylcholine (DPPC) molecules. The Simple Point Charge (SPC) water model mimicked the aqueous environment surrounding the membrane. Velocities of water and membrane molecules were generated randomly at each simulation run according to a Maxwellian distribution. For statistical significance, a total of eight MD simulations were carried out with different starting molecular velocities for each case. A 4 fs time step was used.

**VITA****James Thomas Camp****Education:**

**Doctor of Philosophy** (Electrical Engineering), Old Dominion University, Norfolk, Virginia: May 2012.

**Bachelor of Science** (Applied Physics), Christopher Newport University, Newport News, Virginia: December 2005.